

2009

Preparation and characterization of novel nanometer-scale platinum electrodes

Leanne Petry
University of Dayton

Follow this and additional works at: https://ecommons.udayton.edu/graduate_theses

Recommended Citation

Petry, Leanne, "Preparation and characterization of novel nanometer-scale platinum electrodes" (2009). *Graduate Theses and Dissertations*. 4926.
https://ecommons.udayton.edu/graduate_theses/4926

This Dissertation is brought to you for free and open access by the Theses and Dissertations at eCommons. It has been accepted for inclusion in Graduate Theses and Dissertations by an authorized administrator of eCommons. For more information, please contact mschlange1@udayton.edu, ecommons@udayton.edu.

PREPARATION AND CHARACTERIZATION
OF NOVEL NANOMETER-SCALE
PLATINUM ELECTRODES

Dissertation

Submitted to

The School of Engineering of the
UNIVERSITY OF DAYTON

in Partial Fulfillment of the Requirements for

The Degree

Doctor of Philosophy in Materials Engineering

By

Leanne Petry

UNIVERSITY OF DAYTON

Dayton, Ohio

December 2009

PREPARATION AND CHARACTERIZATION OF NOVEL NANOMETER-SCALE
PLATINUM ELECTRODES

APPROVED BY:



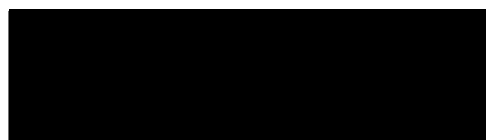
Paul T. Murray, Ph.D.
Committee Chairman
Technical Advisor
Professor
Materials Engineering



Robert G. Keil, Ph.D.
Committee Member
Co-Advisor
Professor
Chemistry



James A. Snide, Ph.D.
Committee Member
Professor Emeritus
Materials Engineering



Gerald J. Shaughnessy, M.S.
Committee Member
Associate Professor
Mathematics



Douglas C. Hansen, Ph.D.
Committee Member
Associate Professor
Materials Engineering



Malcolm W. Daniels, Ph.D.
Associate Dean
School of Engineering



Tony E. Saliba, Ph.D.
Dean
School of Engineering

ABSTRACT

PREPARATION AND CHARACTERIZATION OF NOVEL NANOMETER-SCALE PLATINUM ELECTRODES

Name: Petry, Leanne
University of Dayton

Co-Advisors: Dr. P. T. Murray and Dr. R. G. Keil

Observation of the oxidation-reduction processes occurring at the nanoelectrode-solution interface demonstrates how electrochemical behavior depends upon nanoelectrode size. The use of a modified form of pulsed laser ablation as an improved method to synthesize nanometer-scaled electrode materials easily and consistently is reported. This method of fabrication enables platinum metal nanoparticles averaging 3 nm in diameter and approximately 5.0×10^{11} particles/cm² to be deposited onto silicon substrates using optimum ablation parameters. A platinum silicide phase exists at the interface of the platinum and silicon as a result of the ablation process. Impedance and cyclic voltammetric results demonstrate single electron transfer and the absence of diffusion control, with 1.1×10^7 particles/cm² separated by an average distance of 14 nm between electrochemically active nanoelectrodes.

Dedicated to
my beloved family:
Paul and Alex
for reminding me there is more to life;
to my Dad in the hope that he has found peace in everlasting life;
to Saint Mary and all the blessings of motherhood;
and finally to the Holy Trinity:
the Father, Son and Holy Spirit,
for directing me to do God's will.

ACKNOWLEDGEMENTS

This research was supported by the United States Army Research Office (Dr. W. Lampert) under Grant Number W911NF-07-1-0518 as well as the Ohio Board of Regents Innovation Incentive Graduate Assistantship and the Dayton Area Graduate Studies Institute Graduate Assistantship.

To the memory of Dr. N. J. Farrier for the early motivation to one day pursue this advanced degree. To co-advisors Drs. P. T. Murray and R. G. Keil for the unique interdisciplinary opportunity to combine materials with electrochemical research. For 20 years their commitment to research and dedication to teaching enabled the realization of Farrier's vision, only at ultraviolet wavelengths.

To the support of advisory committee members G. Shaughnessy and Dr. D. C. Hansen for their excellent guidance and behind the scenes lifesaving techniques, specifically for comments and suggestions pertaining to my experimental design and setup, not to mention database recovery.

To all the faculty and staff of the Chemical and Materials Engineering Program as well as the Chemistry Department, particularly the efforts of Drs. D. Eylon, J. A. Snide, P. Sjoblom, and H. Knachel for their encouraging and nurturing spirit. I am especially thankful for the administrative assistance and friendship of Ms. C. Seitz.

The technical advice and expertise of T. Back, L. Grazulis, L. Kasten, V. Nalladega, N. Pierce, and S. Streiker as well as Drs. E. Shin and Y. Yoon was greatly appreciated. Additionally, gratitude is extended to Drs. J. Johnson (XPS) and D. Tomich (XRD) of the Air Force Research Laboratory for granting access and usage privileges for the X-ray analysis equipment used in this work.

Family and friends: To my loving and devoted husband, Paul Andrew Petry; beloved son, Alexander Noel Petry; parents, James Robert Hansell and Connie Lee McIntyre-Hansell; God Almighty and Mary, Mother of us all; for it is in your presence that I find solace. To all others who deserve to be mentioned but are not named here, I am indebted to you.

TABLE OF CONTENTS

	<u>Page</u>
ABSTRACT	iii
ACKNOWLEDGEMENTS	v
LIST OF FIGURES	x
LIST OF TABLES	xvi
LIST OF SYMBOLS, ABBREVIATIONS, AND NOMENCLATURE	xvii
CHAPTERS	
I. INTRODUCTION	1
II. LITERATURE REVIEW	6
2.1. Nanofabrication	6
2.2. Conventional Pulsed Laser Ablation (PLA)	8
2.3. Electrode Behavior	10
2.4. References	14
III. PLATINUM ABLATION AND PLUME CHARACTERIZATION	23
3.1. Introduction	23
3.2. Experimental	24
3.3. Results and Discussion	26
3.4. Summary	29

	<u>Page</u>
3.5. References	31
3.6. Figures	33
IV. MORPHOLOGY OF NANOELECTRODES	42
4.1. Introduction	42
4.2. Experimental	42
4.3. Results and Discussion	44
4.4. Summary	47
4.5. References	49
4.6. Table	50
4.7. Figures	51
V. COMPOSITION OF NANOELECTRODES	58
5.1. Introduction	58
5.2. Experimental	61
5.3. Results and Discussion	61
5.4. Summary	64
5.5. References	65
5.6. Figures	66
VI. NANOELECTRODE ELECTROCHEMISTRY	75
6.1. Introduction	75
6.2. Experimental	76
6.3. Results and Discussion	78

	<u>Page</u>
6.4. Summary	84
6.5. References	86
6.6. Tables	88
6.7. Figures	90
VII. CONCLUSIONS AND RECOMMENDATIONS	97
7.1. References	102
7.2. Figures	103
APPENDICES	
A. CALCULATION OF IONIZED PLATINUM PER ABLATED PLATINUM ATOM	109
B. ESTIMATED ENERGY OF PLATINUM DURING MELT TRANSITION	110
C. TABULAR AND GRAPHICAL REPRESENTATION OF TTFA EFFICIENCY AND PERCENT SUBSTRATE COVERAGE	111

LIST OF FIGURES

<u>Figure</u>	<u>Page</u>
3.1. Optical photograph of fused silica target after Pt TTFA. Laser footprint is 2.0 cm by 1.2 cm, denoted a and b respectively, having an area of 2.4 cm ² .	33
3.2. Ablation setup for TTFA synthesis.	33
3.3. Instrumentation setup for ion current, emission spectroscopy, and time of flight measurements.	34
3.4. Photograph of Pt plume in vacuum.	34
3.5. Time of flight spectrum of ion currents measured from Pt TTFA plume in vacuum.	35
3.6. Temperature of Pt plume produced via TTFA in (a) vacuum, T=2940K and (b) 5 Torr argon, T=2938K. The blue curve is a fit of the emission spectra (red and purple curves) using the blackbody formula.	36
3.7. Emission spectra from Pt TTFA plume in vacuum at (a) 6 μ s delay, (b) 8 μ s delay, (c) 10 μ s delay, (d) 20 μ s delay, (e) 200 μ s delay, and (f) 400 μ s delay.	37
3.8. Emission spectra from Pt TTFA plume in vacuum at (a) 800 μ s delay and (b) 1000 μ s delay.	38
3.9. Time of flight spectrum of Pt during TTFA in (a) vacuum and (b) 5 Torr argon.	39
3.10. Propagation of TTFA plume in vacuum as a function of time over a distance of 25 mm.	40
3.11. Propagation of TTFA plume in 5 Torr argon as a function of time over a distance of 25 mm.	41

	<u>Page</u>
4.1. Micrograph images (magn. 150k, $0.1\ \mu\text{m}^2$) of Pt nanoparticles from TTFA in (a) vacuum and (b) 5 Torr argon.	51
4.2. Size distribution of Pt nanoparticles from TTFA in (a) vacuum and (b) 5 Torr argon.	52
4.3. (a) Micrograph images (magn. 150k, $0.1\ \mu\text{m}^2$) from matrix of samples using a 20 nm Pt TF TTFA target. The legend to identify the ablation parameters used is (1) 600 mJ/cm ² -5 Torr Ar-4S-50 mm, (2) 500 mJ/cm ² -5 Torr Ar-4S-75 mm, (3) 600 mJ/cm ² -10 Torr Ar-1S-50 mm, and (4) 500 mJ/cm ² -10 Torr Ar-1S-75 mm. (b) Size distribution of condition (1) "optimum ablation parameters".	53
4.4. (a) Micrograph images (magn. 150k, $0.1\ \mu\text{m}^2$) from matrix of samples using a 10 nm Pt TF TTFA target. The legend to identify the ablation parameters used is (1) 600 mJ/cm ² -5 Torr Ar-4S-50 mm, (2) 500 mJ/cm ² -5 Torr Ar-4S-75 mm, (3) 600 mJ/cm ² -10 Torr Ar-1S-50 mm, and (4) 500 mJ/cm ² -10 Torr Ar-1S-75 mm. (b) Size distribution of condition (1) "optimum ablation parameters".	54
4.5. Micrograph images (magn. 30k, $3.0\ \mu\text{m}^2$) from matrix of samples using a 5 nm Pt TF TTFA target. The legend to identify the ablation parameters used is (1) 600 mJ/cm ² -5 Torr Ar-4S-50 mm, (2) 500 mJ/cm ² -5 Torr Ar-4S-75 mm, (3) 600 mJ/cm ² -10 Torr Ar-1S-50 mm, and (4) 500 mJ/cm ² -10 Torr Ar-1S-75 mm.	55
4.6. Scanning electron micrographs (SEM) of Pt nanoparticles deposited by TTFA on Si substrates. (a) Examination of particles orientated perpendicular to the electron beam suggests they are round. (b) Examination of particles when tilted suggests they are round but flat (pancake-like).	56
4.7. Platinum nanoparticle height determination. (a) Atomic force micrograph taken in non-contact mode shows numerous nanoparticles (bright contrast) that are approximately 0.6 nm tall. Particle heights are shown in the table and range 0.5 - 0.7 nm. (b) Line profiles across these particles suggest the nanoparticles are wider than they are tall (i.e. flat).	57

5.1. X-ray diffraction spectra of a collection of Pt nanoparticles deposited on Si by TTFA using the "optimum ablation parameters" compared with a RF magnetron sputtered 10 nm Pt TF. Diffraction of X-rays was observed in all cases at angles of 2θ indicative of Pt. For the TTFA samples, compositional differences were noted by the presence of peaks at additional diffraction angles. These additional peaks were consistent with various silicide phases.

66

5.2. X-ray photoelectron spectroscopy of the Pt 4f peak at the surface of the test matrix of samples. The collection of spectra are from as-deposited (unannealed) samples. Curves 1-11 are for test matrix samples as follows: (1) Pt foil-unannealed, (2) 20 nm-600 mJ/cm²-vacuum-1S-50 mm, (3) 20 nm-600 mJ/cm²-5 Torr Ar-4S-50 mm, (4) 20 nm-600 mJ/cm²-10 Torr Ar-4S-75 mm, (5) 20 nm-500 mJ/cm²-5 Torr Ar-1S-50 mm, (6) 20 nm-500 mJ/cm²-10 Torr Ar-1S-75 mm, (7) 10 nm-600 mJ/cm²-vacuum-1S-50 mm, (8) 10 nm-600 mJ/cm²-5 Torr Ar-1S-75 mm, (9) 10 nm-600 mJ/cm²-10 Torr Ar-1S-50 mm, (10) 10 nm-500 mJ/cm²-5 Torr Ar-4S-75 mm, and (11) 10 nm-500 mJ/cm²-10 Torr Ar-4S-50 mm.

67

5.3. X-ray photoelectron spectroscopy of the Pt 4f peak at the surface of the test matrix of samples. The collection of spectra are from samples annealed at 410°C. Curves 1-11 are for test matrix samples as follows: (1) Pt foil-annealed, (2) 20 nm-600 mJ/cm²-vacuum-1S-50 mm, (3) 20 nm-600 mJ/cm²-5 Torr Ar-1S-75 mm, (4) 20 nm-600 mJ/cm²-10 Torr Ar-1S-50 mm, (5) 20 nm-500 mJ/cm²-5 Torr Ar-4S-75 mm, (6) 20 nm-500 mJ/cm²-10 Torr Ar-4S-50 mm, (7) 10 nm-600 mJ/cm²-vacuum-1S-50 mm, (8) 10 nm-600 mJ/cm²-5 Torr Ar-4S-50 mm, (9) 10 nm-600 mJ/cm²-10 Torr Ar-4S-75 mm, (10) 10 nm-500 mJ/cm²-5 Torr Ar-1S-50 mm, and (11) 10 nm-500 mJ/cm²-10 Torr Ar-1S-75 mm.

68

5.4. X-ray photoelectron spectroscopy of the Pt 4f peak at the interface of the test matrix of samples. The collection of spectra are from as-deposited (unannealed) samples. Curves 1-11 are for test matrix samples as follows: (1) Pt foil-unannealed, (2) 20 nm-600 mJ/cm²-vacuum-1S-50 mm, (3) 20 nm-600 mJ/cm²-5 Torr Ar-4S-50 mm, (4) 20 nm-600 mJ/cm²-10 Torr Ar-4S-75 mm, (5) 20 nm-500 mJ/cm²-5 Torr Ar-1S-50 mm, (6) 20 nm-500 mJ/cm²-10 Torr Ar-1S-75 mm, (7) 10 nm-600 mJ/cm²-vacuum-1S-50 mm, (8) 10 nm-600 mJ/cm²-5 Torr Ar-1S-75 mm, (9) 10 nm-600 mJ/cm²-10 Torr Ar-1S-50 mm, (10) 10 nm-500 mJ/cm²-5 Torr Ar-4S-75 mm, and (11) 10 nm-500 mJ/cm²-10 Torr Ar-4S-50 mm.

69

5.5. X-ray photoelectron spectroscopy of the Pt 4f peak at the interface of the test matrix of samples. The collection of spectra are from samples annealed at 410°C. Curves 1-11 are for test matrix samples as follows: (1) Pt foil-annealed, (2) 20 nm-600 mJ/cm²-vacuum-1S-50 mm, (3) 20 nm-600 mJ/cm²-5 Torr Ar-1S-75 mm, (4) 20 nm-600 mJ/cm²-10 Torr Ar-1S-50 mm, (5) 20 nm-500 mJ/cm²-5 Torr Ar-4S-75 mm, (6) 20 nm-500 mJ/cm²-10 Torr Ar-4S-50 mm, (7) 10 nm-600 mJ/cm²-vacuum-1S-50 mm, (8) 10 nm-600 mJ/cm²-5 Torr Ar-4S-50 mm, (9) 10 nm-600 mJ/cm²-10 Torr Ar-4S-75 mm, (10) 10 nm-500 mJ/cm²-5 Torr Ar-1S-50 mm, and (11) 10 nm-500 mJ/cm²-10 Torr Ar-1S-75 mm.

70

5.6. X-ray photoelectron spectroscopy of the Si 2p peak at the surface of the test matrix of samples. The collection of spectra are from as-deposited (unannealed) samples. Curves 1-11 are for test matrix samples as follows: (1) Si substrate-unannealed, (2) 20 nm-600 mJ/cm²-vacuum-1S-50 mm, (3) 20 nm-600 mJ/cm²-5 Torr Ar-4S-50 mm, (4) 20 nm-600 mJ/cm²-10 Torr Ar-4S-75 mm, (5) 20 nm-500 mJ/cm²-5 Torr Ar-1S-50 mm, (6) 20 nm-500 mJ/cm²-10 Torr Ar-1S-75 mm, (7) 10 nm-600 mJ/cm²-vacuum-1S-50 mm, (8) 10 nm-600 mJ/cm²-5 Torr Ar-1S-75 mm, (9) 10 nm-600 mJ/cm²-10 Torr Ar-1S-50 mm, (10) 10 nm-500 mJ/cm²-5 Torr Ar-4S-75 mm, and (11) 10 nm-500 mJ/cm²-10 Torr Ar-4S-50 mm.

71

5.7. X-ray photoelectron spectroscopy of the Si 2p peak at the surface of the test matrix of samples. The collection of spectra are from samples annealed at 410°C. Curves 1-11 are for test matrix samples as follows: (1) Si substrate-annealed, (2) 20 nm-600 mJ/cm²-vacuum-1S-50 mm, (3) 20 nm-600 mJ/cm²-5 Torr Ar-1S-75 mm, (4) 20 nm-600 mJ/cm²-10 Torr Ar-1S-50 mm, (5) 20 nm-500 mJ/cm²-5 Torr Ar-4S-75 mm, (6) 20 nm-500 mJ/cm²-10 Torr Ar-4S-50 mm, (7) 10 nm-600 mJ/cm²-vacuum-1S-50 mm, (8) 10 nm-600 mJ/cm²-5 Torr Ar-4S-50 mm, (9) 10 nm-600 mJ/cm²-10 Torr Ar-4S-75 mm, (10) 10 nm-500 mJ/cm²-5 Torr Ar-1S-50 mm, and (11) 10 nm-500 mJ/cm²-10 Torr Ar-1S-75 mm.

72

5.8. X-ray photoelectron spectroscopy of the Si 2p peak at the interface of the test matrix of samples. The collection of spectra are from as-deposited (unannealed) samples. Curves 1-11 are for test matrix samples as follows: (1) Si substrate-unannealed, (2) 20 nm-600 mJ/cm²-vacuum-1S-50 mm, (3) 20 nm-600 mJ/cm²-5 Torr Ar-4S-50 mm, (4) 20 nm-600 mJ/cm²-10 Torr Ar-4S-75 mm, (5) 20 nm-500 mJ/cm²-5 Torr Ar-1S-50 mm, (6) 20 nm-500 mJ/cm²-10 Torr Ar-1S-75 mm, (7) 10 nm-600 mJ/cm²-vacuum-1S-50 mm, (8) 10 nm-600 mJ/cm²-5 Torr Ar-1S-75 mm, (9) 10 nm-600 mJ/cm²-10 Torr Ar-1S-50 mm, (10) 10 nm-500 mJ/cm²-5 Torr Ar-4S-75 mm, and (11) 10 nm-500 mJ/cm²-10 Torr Ar-4S-50 mm.

73

	<u>Page</u>
5.9. X-ray photoelectron spectroscopy of the Si 2p peak at the interface of the test matrix of samples. The collection of spectra are from samples annealed at 410°C. Curves 1-11 are for test matrix samples as follows: (1) Si substrate-annealed, (2) 20 nm-600 mJ/cm ² -vacuum-1S-50 mm, (3) 20 nm-600 mJ/cm ² -5 Torr Ar-1S-75 mm, (4) 20 nm-600 mJ/cm ² -10 Torr Ar-1S-50 mm, (5) 20 nm-500 mJ/cm ² -5 Torr Ar-4S-75 mm, (6) 20 nm-500 mJ/cm ² -10 Torr Ar-4S-50 mm, (7) 10 nm-600 mJ/cm ² -vacuum-1S-50 mm, (8) 10 nm-600 mJ/cm ² -5 Torr Ar-4S-50 mm, (9) 10 nm-600 mJ/cm ² -10 Torr Ar-4S-75 mm, (10) 10 nm-500 mJ/cm ² -5 Torr Ar-1S-50 mm, and (11) 10 nm-500 mJ/cm ² -10 Torr Ar-1S-75 mm.	74
6.1. (a) Cyclic voltammogram from an array of Pt nanoelectrodes as-deposited in vacuum by TTFA. (b) Cyclic voltammogram exhibited by the conventional Pt electrode.	90
6.2. Comparison of cyclic voltammograms from an as-deposited vs. annealed array of Pt nanoelectrodes.	91
6.3. Comparison of cyclic voltammograms from an array of Pt nanoelectrodes synthesized via different ablation parameters and annealed.	92
6.4. Chronoamperometric data for Pt nanoarrays grown in argon at the optimum ablation parameters using targets of different thicknesses.	93
6.5. Nyquist plots for Pt nanoarrays grown in argon at the optimum ablation parameters using targets of different thicknesses. The absence of Warburg impedance indicates the transport effects due to diffusion are small.	94
6.6. Nyquists plots of impedance measurements for TTFA Pt nanoarrays in the presence of propylene carbonate (chemical warfare simulant) or 5.0 % sodium chloride (highly conductive and corrosive electrolyte).	95
6.7. Possible equivalent circuit models. (a) Conventional Randles Circuit where the impedance is best described by the double-layer capacitance in parallel with the charge transfer resistance, both of which are in series with the electrolyte resistance. (b and c) Models in varying configurations distinguishing two time constants (two RC circuits) in series with the electrolyte resistance. In both cases, the capacitor can be replaced by a constant phase element.	96

	<u>Page</u>
Figure 7.1. (a) The blue curve demonstrates the reduction of cadmium for a conventional Pt electrode. (b) Investigation into feasibility of Pt nanoelectrode array to reduce metals (10ppm cadmium, maroon curve and 20 ppm cadmium, black curve) in a solution of ferricyanide. The green curve is for the reduction of ferricyanide solution, only, at the surface of a conventional electrode. (c) Chronoamperometric data showing increasing current with increasing concentration of cadmium being reduced.	103
Figure 7.2. Impedance spectra from Pt nanoelectrode array in propylene carbonate (PC). The aqua (CE near) and purple (CE far) curves were acquired with the CE in different positions relative to WE (Pt array).	104
Figure 7.3. Impedance spectrum from Pt TF on Si in a different cell geometry using a smaller electrolyte volume.	104
Figure 7.4. (a) Micrograph image of carbon nanotube (CNT) growth at 900°C on TTFA deposited Pt nanoparticles on Si substrates. High resolution XPS analyses of this sample indicate the presence of (b) Pt catalysts and formation of oxide on Si as shown in the (c) Si 2p and (d) Si 2s signals.	105
Figure 7.5. Micrograph images of FePt nanoparticles ablated via TTFA at (a) 5 Torr Ar and (b) 10 Torr Ar using (c) a dual layer target consisting of a 10 nm Fe TF layer sandwiched between the transparent support and a 10nm Pt TF layer.	106
Figure 7.6. Chemical composition information for TTFA FePt nanoparticles determined using backscattered electrons (BSE) at (a) 10000x and (b) 20000x.	107
Figure 7.7. Chemical composition of FePt nanoparticles deposited via TTFA on Si substrates surveyed using (a) XRD and (b) XPS.	107
Figure 7.8. (a) Fe 2p, (b) O 1s, (c) Pt 4f, (d) C 1s, (e) Si 2p, and (f) Si 2s high resolution XPS analyses of FePt nanoparticles.	108
C.1. The TTFA method is an efficient means to generate small platinum nanoparticles.	115
C.2. An increase in the nanoelectrode radius indicates a greater percentage of substrate is covered with platinum.	116

LIST OF TABLES

<u>Table</u>	<u>Page</u>
4.1. Platinum Through Thin Film Ablation Test Matrix	50
6.1. Measured limiting current and calculated A_A values for the nanoarrays	88
6.2. Resistive components of electrochemical impedance data for TTFA nanoelectrodes in solutions of ferricyanide, sodium chloride, or propylene carbonate	89
6.3. Capacitive components of electrochemical impedance data for TTFA nanoelectrodes in solutions of ferricyanide, sodium chloride, or propylene carbonate	89
C.1. TTFA efficiency based on nanoparticle diameter size	113
C.2. Substrate coverage as a function of nanoelectrode radius size	114

LIST OF SYMBOLS, ABBREVIATIONS, AND NOMENCLATURE

A_A	active area of nanoelectrode array (cm^2)
CNT	carbon nanotube
C	concentration (M)
cm	centimeter
I	current (A)
D	diffusion coefficient of the reagents in the liquid electrolyte ($\text{cm}^2 \text{s}^{-1}$)
E	electrode potential (V vs Ag/AgCl)
F	Faraday constant
FCC	face centered cubic
fs	femtosecond
A	geometric area of the electrode (cm^2)
Hz	hertz
$ Z $	impedance
J	joule
kJ	kilojoule
MAPLE	matrix assisted pulsed laser evaporation
mm	millimeter
μm	micrometer
R	molar gas constant
nm	nanometer
ns	nanosecond
n	number of electrons involved in the reaction
ps	picosecond
ν	scan rate (V s^{-1})
T	temperature
t	time (s)
TOF	time of flight
UV	ultraviolet
W	watt

CHAPTER I

INTRODUCTION

*We must remember that intelligence is not enough. Intelligence plus character—
that is the goal of true education.*

*—Martin Luther King Jr.,
Speech at Morehouse College
1948*

Nanoelectrodes possess dimensions in the nanometer (nm) range and have specific characteristics that are a direct result of their small size. These small electrodes offer significant advantages over their microscopic and macroscopic counterparts that reach beyond restrictions of space. High current densities can be measured with nanoelectrodes leading to good signal resolution and low detection limits [1, 2]. Additionally, low total current means they can be used in more resistive media or in the absence of conductive electrolytes, thereby expanding the range of detection to numerous chemical and biological analytes for the purpose of environmental and health monitoring or other small organic molecules such as formic acid and methanol for potential use as fuels.

Previous studies by other researchers have been directed at modeling, developing, and characterizing electrodes based on the effect of electrode size and shape in relation to electrochemical events, including diffusion [3-9]. It is known that the voltammetric response at a microelectrode results in a steady-

state current-voltage response that is more readily analyzed than that obtained from a conventional size electrode [10]. This advantage results from the size of the electrode diameter, d , being smaller than the distance that species diffuse (δ) in order to reach the electrode surface ($d < \delta$). Thus, surface diameter is critical to the performance of the electrode.

Microelectrodes can be used in solutions that do not contain a supporting electrolyte and to study very fast electron-transfer kinetics for electrochemical reactions involving redox couples. The potassium ferrocyanide redox couple $\text{Fe(CN)}_6^{4-}/\text{Fe(CN)}_6^{3-}$ has served as the benchmark for studying electrochemical reactions at the surface of platinum electrodes. Recently, there has been interest in the electrochemical behavior of nanometer-scaled electrodes [1, 11-13]. Interest in nanoelectrodes is driven by a desire to combine independent nanoelectrode behavior with high population density so as to maximize the electrochemical response to $\text{Fe(CN)}_6^{3-/4-}$, while at the same time minimizing the power and size requirements.

The work in this dissertation is based on the use of a modified laser ablation process denoted as Through Thin Film Ablation (TTFA) to synthesize platinum nanoparticles to be used as nanoelectrodes. Specifically, the objective of this study was to investigate the influence of laser ablation parameters on the size distribution, number density, composition, and electrochemistry of the nanoelectrodes. However, the effect of a collection of nanoelectrodes has not been investigated rigorously in previous work. This study, therefore, was designed to acquire a basic understanding of electron transfer at the surface of a

distribution of well separated nanoelectrodes. It was hypothesized that nanoelectrode size, density, and composition would influence the electrochemical performance.

This dissertation consists of seven chapters. Chapter 1 is the current chapter giving a brief description of background and objective of this study. Chapter 2 reviews current literature on the subject of nanoparticle synthesis methods. The chapter also examines the various aspects of mass transfer at the surface of an electrode as a function of particle size.

Chapter 3 describes in detail the nanoelectrode synthesis process, and the findings present a basis for the formation of the nanoparticles which are used to fabricate a collection of nanoelectrodes. The nanoelectrode morphology is examined in Chapter 4. The annealing effect on the composition of the nanoelectrodes is shown in Chapter 5. Chapter 6 discusses single electron transfer and the absence of diffusion at the surface of the nanoelectrodes. Each of these chapters contains an introduction, experimental, results, discussion, and summary section and is related to the other as appropriate. The final chapter, Chapter 7, summarizes the overall findings of this work and makes conclusions on the formation and characterization of the nanoelectrodes. The final chapter also presents several ideas that are appropriate for future work.

References

- [1] S. Oh, J. S. Lee, K. H. Jeong, L. P. Lee, "Minimization of Electrode Polarization Effect by Nanogap Electrodes for Biosensor Applications, in Micro Electro Mechanical Systems," The Sixteenth Annual International Conference, IEEE, MEMS-03 Kyoto, 52, Jan 19-23, 2003, IEEE, (2003).
- [2] N. Punbusayakul, S. Talapatra, L. Ci, W. Surareungchai, P. M. Ajayan, "Double-Walled Carbon Nanotube Electrodes for Electrochemical Sensing," *Electrochem. Solid State Lett.*, 10 (2007) F13.
- [3] J. E. B. Randles, "A Cathode Ray Polarograph. Part II.-The Current-Voltage Curves," *Trans. Faraday Soc.*, 44 (1948) 327.
- [4] A. Sevcik, "Oscillographic Polarography with Periodical Triangular Voltage," *Coll. Czech. Chem. Commun.*, 13 (1948) 349.
- [5] R. S. Nicholson, I. Shain, "Theory of Stationary Electrode Polarography: Single Scan and Cyclic Methods Applied to Reversible, Irreversible, and Kinetic Systems," *Anal. Chem.*, 36 (1964) 706.
- [6] A. G. Ewing, M. A. Dayton, R. M. Wightman, "Pulse Voltammetry with Microvoltammetric Electrodes," *Anal. Chem.*, 53 (1981) 1842.
- [7] M. Fleischmann, S., Pons, D., Rolison, P. Schmidt, "Ultramicroelectrodes," Datatech Systems, Inc., Science Publishers, 1987.
- [8] R. M. Wightman, "Voltammetry with Microscopic Electrodes in New Domains," *Science*, 240 (1988) 415.
- [9] V. Komanicky, W. R. Fawcett, "Fabrication of Gold and Platinum Single Crystal Ultramicroelectrodes," *Electrochim. Acta*, 49 (2004) 1185.

- [10] J. J. Watkins, J. Chen, H. S. White, H. D. Abruna, E. Maisonhaute, C. Amatore, "Zeptomole Voltammetric Detection and Electron-Transfer Rate Measurements Using Platinum Electrodes of Nanometer Dimensions," *Anal. Chem.*, 75 (2003) 3962.
- [11] J. L. Conyers, Jr., H. S. White, "Electrochemical Characterization of Electrodes with Submicrometer Dimensions," *Anal. Chem.*, 72 (2000) 4441.
- [12] R. J. White, H. S. White, "Electrochemistry in Nanometer-Wide Electrochemical Cells," *Langmuir*, 24 (2008) 2850.
- [13] Y. Zhang, J. Zhou, L. Lin, Z. Lin, "Determination of Electrochemical Electron-Transfer Reaction Standard Rate Constants at Nanoelectrodes: Standard Rate Constants for Ferrocenylmethyltrimethylammonium (III)/(II) and Hexacyanoferrate (III)/(II)," *Electroanalysis*, 20 (2008) 1490.

CHAPTER II

LITERATURE REVIEW

*Search me, O God, and know my heart; test me and know my anxious thoughts.
See if there is any offensive way in me, and lead me in the way everlasting.
-Psalm 139:23-24*

The purpose of this literature review is to provide an overview of nanoparticle synthesis methods and to discuss electrode reactions. A large amount of research has been devoted to fabricating nanoparticles and understanding electrode behavior. Nonetheless, a large amount of work remains to be done in the novel arena of nanoelectrode preparation and characterization.

Nanofabrication

Nanotechnology is defined as “the design, fabrication and use of nanostructured systems, and the growing, shaping or assembling of such systems either mechanically, chemically or biologically to form nanoscale architectures, systems and devices” [1]. The materials used in nanotechnology and the study of their behavior when the dimensions are reduced to the nanoscale (i.e. at least one

dimension that is in the 1 to 100 nanometer (nm) range) are known as nanomaterials [2]. The development of processes and sensors on the nanoscale promise to provide exciting new opportunities as the physical world at the atomic, i.e., nanometer, level is markedly different from that observed in the bulk.

Nanoparticle species with diameters less than 100 nm have been prepared by numerous gas and solution phase techniques. Physical [3] and chemical [4] deposition methods, including aerosol formation, [5-9] are among the most common gas phase processing approaches and may make use of ion beams [10-12] and sputtering [13], electron beams [14] and plasmas [15], as well as laser beams [16-19] in a vacuum environment. However, achieving the desired morphology, density, or composition can be a problem with these growth processes. Since scalability is also an issue with gas techniques, many researchers have turned to various solution methods to manipulate metals in a liquid environment. The precious metals silver (Ag) [20], gold (Au) [21], palladium (Pd) [22], platinum (Pt) [23,24], rhodium (Rh) [28], other transition metals such as iron (Fe) [29] and copper (Cu) [30-33] in addition to mercury (Hg) [34] in the form of salts have been electrochemically reduced and the resultant nanoparticles' nanometer sized dimensions intensely studied. Unfortunately, an agglomerated or clustered distribution of nanoparticles is a recurring problem with liquid techniques. Thus, the production of nanosized metal particles by the chemical reduction of metal ions in solution using reducing agents [35-37], is

performed in the presence of protective stabilizers to minimize the effect of particle agglomeration [38,39]. Although the syntheses themselves can be somewhat lengthy, as well as messy processes, solution chemistry methods continue to be used due to their versatility in the stabilization and functionalization of a variety of nanoparticles.

Conventional Pulsed Laser Ablation (PLA)

An ideal technique for the fabrication of nanoparticles would be one such that monodisperse particle distributions are produced easily and reproducibly with contamination-free tailorability of size and shape, with an ability to functionalize particle chemistry by the addition of ligands, or with the potential to alloy the particle with another metal to produce a nanocomposite structure. As compared to less “clean” electrochemical reduction methods, plasma processing is an environmentally friendly manufacturing technology that produces low levels of industrial waste. One way to produce a plasma is to use a laser. More recently reported has been the pulsed laser ablation (PLA) synthesis of nanoparticle materials [16-19].

Conventional PLA synthesis methods direct a tightly focused high power laser beam at a solid target which is a few millimeters (mm) thick. The solid is quickly heated, ionized, and ablated to form a divergent plasma which expands freely and cools adiabatically into the surrounding vacuum or background gas.

By carefully selecting the ablation parameters, the ablation process can be manipulated in such a way as to nucleate, grow, and accelerate the ablated species by the transfer of energy and momentum in the plasma toward a substrate. High power (i.e. 10^9 W) at ultraviolet (UV) wavelengths (i.e. 248 nm for a krypton fluoride, KrF, gas mixture) is typically generated for excimer lasers. When operated at a repetition rate of a few hertz (Hz), laser energies in the tens of millijoules (mJ) per pulse can be emitted. Thus, control of the laser power output (watts (W)) is one way to control the transfer of energy and the ablation conditions necessary to synthesize nanoparticles, specifically the Pt nanoparticles proposed in this study.

Commercially available excimer lasers, with output wavelengths in the nm range, produce nanosecond (ns) pulses, energies up to joules (J), and utilize molecules, such as the KrF mentioned previously, as active lasing media. The duration of the laser pulse is another parameter capable of being modified during experimentation. Supplying the energy in short bursts (i.e. duration on the order of ns, picosecond (ps), or femtosecond (fs)) can reduce localized heating of the target.

One alternative to conventional PLA is matrix assisted pulsed laser evaporation or MAPLE. It was originally developed for molecule-by-molecule deposition of organic material such as polymers [40], carbon nanotubes (CNTs) [41], and nanopearls [42]. A. T. Sellinger et al. explained the premise behind the

matrix assisted process was to minimize interactions between the laser and polymer molecules, promoting growth at reduced energies as compared to conventional PLA [43]. In another article co-authored by Sellinger, another goal of the process was to minimize chemical modification of the target material [44]. In MAPLE, the target was fabricated by dissolving the material to be deposited into a volatile solvent such as toluene and flash freezing the solution in liquid nitrogen before placing the solid target into the vacuum chamber for deposition. Ablation with an excimer laser ($\lambda = 248$ nm) was performed onto substrates similar to conventional PLA. This method of ablation was not conducive to producing material of nanoparticle size as can be achieved via conventional PLA [16-19]; however, it may be ideally suited to stabilizing metal nanoparticles with organic ligands or polymers [45].

Electrode Behavior

Electrochemical reactions occur at the electrode/solution interface, creating a diffusion boundary layer at the electrode surface. Work by Randles [46] and Sivicik [47] and the later numerical work of Nicholson and Shain [48] showed the fundamental relationship between current, concentration, diffusion coefficient and sweep rate. Generally these experiments were conducted on large working electrodes, and the cyclic voltammetry experiment required diffusion transport of the redox couple to the electrode due to the formation of the

diffusion boundary layer, resulting in depletion of the electroactive species within the diffusion boundary layer and consequent loss of resolution for activities occurring at the electrode interface.

Pioneering research by Fleischmann [49] and Wightman [50,51] provide the basis for the development of microelectrode sensors. The benefits of these types of sensors are attributed to the small dimensions of the microelectrode, leading to spherical diffusion and rapid steady state operation. The time dependent current at an infinite planar electrode is given by the Cottrell equation:

$$i(t) = nFAD^{1/2}C/(\pi t)^{1/2} \quad (2.1)$$

where n is the number of electrons in the reaction, F is the Faraday constant, A is electrode surface area, D is the diffusion coefficient, C is the reactant concentration, and t is the time. The time dependent current at a sphere is given by:

$$i(t) = nFADC[(\pi Dt)^{-1/2} + r^{-1}] \quad (2.2)$$

where r is the radius of the sphere. Note that the case of spherical diffusion contains a time-dependent "Cottrellian" term and a time-independent term. At small r values, the time-independent term dominates. For example, for $r = 5$ micrometers (μm) and $D = 10^{-5} \text{ cm}^2/\text{sec}$, the time-independent current is ten times the time-dependent "Cottrellian" current after only 0.8 sec. Consequently, steady state current is attained in real time, allowing for fast measurements and also enhancing the mass transfer to the electrode surface that results in an

increase in sensitivity. In summary, several characteristics of microelectrodes are relevant to the development of nanoelectrodes:

- Improved efficiency and sensitivity resulting from enhanced signal to noise
- Rapid real-time response rates due to steady-state operation
- Low current and voltage requirements
- Decreased electrolyte resistance effects, eliminating the need for addition of conductive solvents for electrochemical analysis.

In recent years, there has been growing interest in the electrochemical behavior of an electrode when its size is further reduced from the micrometer to the nanometer scale. Interest in these ultra-small electrodes is driven by a curiosity in understanding how electrochemical behavior depends on electrode size and by achievement of increased sensitivity that cannot be achieved with conventional electrodes of large dimensions. In this dissertation, nanoparticle electrodes are configured in a fashion to enhance sensitivity to an oxidation-reduction couple while providing a decreased electrode response time and an increase in the signal to noise ratio of the electrochemical signal. Observation of electrochemistry at nano-scale electrodes includes single electron or staircase events [52]. Extending the capability of a sensing electrode to single electron events within a single molecule may usher in a new age of analytical capability. In the future, there exists the intriguing possibility of detecting events that result in the transfer of less than a single electron; an example of such an event

includes detecting dipole/polarization differences within a molecule. Achieving the desired sensitivity will require the ability to replicate large numbers of these nano-scale electrodes configured within a high population density. The sensor capability of each should be independent. In this work, nano-scale sensor electrodes are prepared using TTFA, which is explained in the next Chapter.

While the use of precious metals is diverse, their availability and cost typically restrict the range of applications to circumstances where limited amounts of material are used or there is no viable alternative. Currently, noble metals are used for corrosion protection [53,54] as well as high temperature [53,55] and fuel cell [56] applications. In addition to currency and jewelry, a more archaic use of precious metals is found in the photographic and printing industries [21,57,58]. Of the eight precious metals, Platinum (Pt) is the material of choice for electrode studies because it is catalytic and inert. Similar to the catalytic surface used in fuel cells, platinum-based catalysts are ideal liners for catalytic converters in car exhausts lines [59] and chemical reactors [53]. Qualities of biocompatibility [60] and radio-opacity [61,62] increase the use of this precious metal in medical devices and related tools. Lastly, pharmaceutical applications are playing a key role in drug delivery for cancer treatment [63]. It is in these areas where precious nano-metal fabrication and nanoelectrode use would be ideal.

References

- [1] R. M. Brydson, C. Hammond, Generic Methodologies for Nanotechnology - Classification and Fabrication, in: R. W. Kelsall, I. W. Hamley, M. Geoghegan (Eds.), Nanoscale Science and Technology, John Wiley & Sons, West Sussex, England, 2005, pp. 4, 20, 28.
- [2] M. Wilson, K. Kannangara, G. Smith, M. Simmons, B. Raguse, Nanotechnology - Basic Science and Emerging Technologies, Chapman & Hall, New York, 2002, p. 56.
- [3] E. Aschauer, R. Fasching, G. Urban, G. Nicolussi, W. Husinsky, "Surface Characterization of Thin-Film Platinum Electrodes for Biosensors by Means of Cyclic Voltammetry and Laser SNMS," J. Electroanal. Chem., 381 (1995) 143.
- [4] D. S. Y. Hsu, L. M. Troilo, N. H. Turner, K. W. Pierson, "Selective Area Platinum Silicide Film Deposition Using a Molecular Precursor Chemical Beam Source," Thin Solid Films, 269 (1995) 21.
- [5] A. P. Weber, M. Seipenbusch, G. Kasper, "Application of Aerosol Techniques to Study the Catalytic Formation of Methane on Gasborne Nickel Nanoparticles," J. Phys. Chem. A, 105 (2001) 8958.
- [6] Y. Singh, J. R. N. Javier, S. H. Ehrman, M. H. Magnusson, K. Deppert, "Approaches to Increasing Yield in Evaporation/Condensation Nanoparticle Generation," Aerosol Sci., 33 (2002) 1309.

- [7] S. S. Talukdar, M. T. Swihart, "Aerosol Dynamics Modeling of Silicon Nanoparticle Formation during Silane Pyrolysis: A Comparison of Three Solution Methods," *Aerosol Sci.*, 35 (2004) 889.
- [8] A. P. Weber, M. Seipenbusch, C. Thanner, G. Kasper, "Aerosol Catalysis on Nickel Nanoparticles," *J. Nanopart. Res.*, 1 (1999) 253.
- [9] A. P. Weber, M. Seipenbusch, J. Binnig, G. Kasper, "Influence of the Particle Morphology on the Activity of Nanometer Platinum Aerosol Catalysts," *Part. Part. Syst. Charact.*, 19 (2002) 300.
- [10] B. Xu, S. I. Tanaka, "Formation and Bonding of Platinum Nanoparticles Controlled by High Energy Beam Irradiation," *Scripta Mater.*, 44 (2001) 2051.
- [11] L. D'Urso, V. Nicolosi, G. Compagnini, O. Puglisi, "Size Distribution of Silver Nanoclusters Induced by Ion, Electron, Laser Beams and Thermal Treatments of an Organometallic Precursor," *Appl. Surf. Sci.*, 226 (2004) 131.
- [12] C. Maurizio, "Multielemental Nanoclusters Formed by Ion Implantation in Dielectrics," *Nucl. Instrum. Methods Phys. Res., Sect. B*, 218 (2004) 396.
- [13] J. J. Blackstock, Z. Li, M. R. Freeman, D. R. Stewart, "Ultra-Flat Platinum Surfaces from Template-Stripping of Sputter Deposited Films," *Surf. Sci.*, 546 (2003) 87.
- [14] S. Johansson, K. Wong, V. P. Shdanov, B. Kasemo, "Nanofabrication of Model Catalysts and Simulations of Their Reaction Kinetics," *J. Vac. Sci. Technol., A*, 17 (1999) 297.

- [15] J. S. Becker, C. Pickhardt, W. Pompe, "Determination of Ag, Ti, and Pb in a Few Milligrams of Platinum Nanoclusters by On-Line Isotope Dilution in Laser Ablation Inductively Coupled Plasma Mass Spectroscopy," *Int. J. Mass Spec.*, 237 (2004) 13.
- [16] K. S. Seol, R. P. Camata, K. Takeuchi, "Study on the Formation of Silicon Nanoparticles during Laser Ablation Using a Low Pressure Differential Mobility Analyzer," *J. Aerosol Sci.*, 30 (1999) S467.
- [17] F. Mafune, J. Kohno, Y. Takeda, T. Kondow, "Formation of Stable Platinum Nanoparticles by Laser Ablation in Water," *J. Phys. Chem. B*, 107 (2003) 4218.
- [18] F. Mafune, J. Kohno, Y. Takeda, T. Kondow, "Nanoscale Soldering of Metal Nanoparticles for Construction of Higher-Order Structures," *J. Am. Chem. Soc.*, 125 (2003) 1686.
- [19] M. R. Davidson, Y. Fan, G. J. Berry, J. A. Cairns, A. G. Fitzgerald, "Analysis of Laser Irradiated Organo-Platinum Films," *Mikrochim. Acta*, 139 (2002) 43.
- [20] J. L. Elechiguerra, L. Larios-Lopez, C. Liu, D. Garcia-Gutierrez, A. Camacho-Bragado, M. J. Yacaman, "Corrosion at the Nanoscale: The Case of Silver Nanowires and Nanoparticles," *Chem. Mater.*, 17 (2005) 6042.
- [21] D. W. Chang, L. Dai, "Photo-Induced Formation and Self-Assembling of Gold Nanoparticles in Aqueous Solution of Amphiphilic Dendrimers with Oligo(p-phenylene vinylene) Core Branches and Oligo(ethylene oxide) Terminal Chains," *Nanotechnology*, 18 (2007) 1.

- [22] N. Toshima, Y. Shiraishi, T. Teranishi, "Effect of Additional Metal Ions on Catalyses of Polymer-Stabilized Metal Nanoclusters," *J. Mol. Catal. A: Chem.*, 177 (2001) 139.
- [23] S. E. Eklund, D. E. Cliffler, "Synthesis and Catalytic Properties of Soluble Platinum Nanoparticles Protected by a Thiol Monolayer," *Langmuir*, 20 (2004) 6012.
- [24] M. Zhou, S. Chen, H. Ren, L. Wu, S. Zhao, "Electrochemical Formation of Platinum Nanoparticles by a Novel Rotating Cathode Method," *Physica E*, 27 (2005) 341.
- [25] J. Orozco, G. Suarez, C. Fernandez-Sanchez, C. McNeil, C. Jimenez-Jorquera, "Characterization of Ultramicroelectrode Arrays Combining Electrochemical Techniques and Optical Microscopy Imaging," *Electrochim. Acta*, 53 (2007) 729.
- [26] W. Plieth, H. Dietz, A. Anders, G. Sandmann, A. Meixner, M. Weber, H. Kneppel, "Electrochemical Preparation of Silver and gold Nanoparticles: Characterization by Confocal and Surface Enhanced Raman Microscopy," *Surf. Sci.*, 597 (2005) 119.
- [27] Y. Sun, H. H. Wang, "Electrodeposition of Pd Nanoparticles on Single-Walled Carbon Nanotubes for Flexible Hydrogen Sensors," *Appl. Phys. Lett.*, 90 (2007) 213107.
- [28] N. Toshima, Y. Shiraishi, T. Teranishi, M. Miyake, T. Tominaga, H. Watanabe, W. Brijoux, H. Bonnemann, G. Schmid, "Various Ligand-Stabilized

Metal Nanoclusters as Homogeneous and Heterogeneous Catalysts in the Liquid Phase," *Appl. Organometal. Chem.*, 15 (2001) 178.

- [29] F. Dumestre, B. Chaudret, C. Amiens, P. Renaud, P. Fejes, "Supperlattices of Iron Nanocubes Synthesized from $\text{Fe}[\text{N}(\text{SiMe}_3)_2]_2$," *Science*, 303 (2004) 821.
- [30] X. Ren, D. Chen, F. Tang, "Shape-Controlled Synthesis of Copper Colloids with a Simple Chemical Route," *J. Phys. Chem. B*, 109 (2005) 15803.
- [31] L. Y. Zhao, K. R. Eldridge, K. Sukhija, H. Jalili, N. F. Heinig, K. T. Leung, "Electrodeposition of Iron Core-Shell Nanoparticles on a H-Terminated Si (100) Surface," *Appl. Phys. Lett.*, 88 (2006) 033111.
- [32] L. Huang, E. S. Lee, K. B. Kim, "Electrodeposition of Monodisperse Copper Nanoparticles on Highly Oriented Pyrolytic Graphite Electrode with Modulation Potential Method," *Colloids Surf., A: Physicochem. Eng. Aspects*, 262 (2005) 125.
- [33] G. P. Jin, Y. F. Ding, P. P. Zheng, "Electrodeposition of Nickel Nanoparticles on Functional MWCNT Surfaces for Ethanol Oxidation," *J. Power Sources*, 166 (2007) 80.
- [34] U. Hasse, K. Wagner, F. Scholz, "Nucleation at Three-Phase Junction Lines: In Situ Atomic Force Microscopy of the Electrochemical Reduction of Sub-Micrometer Size Silver and Mercury (I) Halide Crystals Immobilized on Solid Electrodes," *J. Solid State Electrochem.*, 8 (2004) 842.

- [35] C. W. Chen, T. Takezako, K. Yamamoto, T. Serizawa, M. Akashi, "Poly(N-vinylisobutyramide)-Stabilized Platinum Nanoparticles: Synthesis and Temperature-Response Behavior in Aqueous Solution," *Colloids Surf., A: Physicochem. Eng. Aspects*, 169 (2000) 107.
- [36] H. H. Ingelsten, R. Bagwe, A. Palmqvist, M. Skoglundh, C. Svanberg, K. Holmberg, D. O. Shah, "Kinetics of Formation of Nano-Sized Platinum Particles in Water-in-Oil Microemulsions," *J. Colloid Interface Sci.*, 241 (2001) 104.
- [37] H. H. Ingelsten, J. C. Beziat, K. Bergkvist, A. Palmqvist, M. Skoglundh, H. Quihong, L. K. L. Falk, K. Holmberg, "Deposition of Platinum Nanoparticles, Synthesized in Water-in-Oil Microemulsions, on Alumina Supports," *Langmuir*, 18 (2002) 1811.
- [38] T. Teranishi, R. Kurita, M. Miyake, "Shape Control of Pt Nanoparticles," *J. Inorg. Organomet. Polym.*, 10 (2000) 145.
- [39] J. P. Carpenter, C. M. Lukehart, S. B. Milne, D. O. Henderson, R. Mu, S. R. Stock, "Formation of Crystalline Nanoclusters of Ag, Cu, Os, Pd, Pt, Re, or Ru in a Silica Xerogel Matrix from Single-Source Molecular Precursors," *Chem. Mater.*, 9 (1997) 3164.
- [40] A. T. Sellinger, E. M. Leveugle, K. Gogick, L. V. Zhigilei, J. M. Fitz-Gerald, "Laser Processing of Polymer Nanocomposite Thin Films," *J. Vac. Sci. Technol. A*, 24 (2006) 1618.

- [41] A. T. Sellinger, E. Leveugle, K. Gogick, G. Peman, L. V. Zhigilei, J. M. Fitz-Gerald, "Ejection of Matrix-Polymer Clusters in Matrix-Assisted Laser Evaporation: Experimental Observations," J. Phys. Conference Series, 59 (2007) 314.
- [42] C. N. Hunter, M. H. Check, J. E. Bultman, A. A. Voevodin, "Development of Matrix-Assisted Pulsed Laser Evaporation (MAPLE) for Deposition of Disperse Films of Carbon Nanoparticles and Gold Nanoparticle Composite Films," Surf. Coat. Technol., 203 (2008) 300.
- [43] A. T. Sellinger, A. H. Martin, J. M. Fitz-Gerald, "Effect of Substrate Temperature on Poly(methyl methacrylate) Nanocomposite Thin Films Deposited by Matrix Assisted Pulsed Laser Evaporation," Thin Solid Films, 516 (2008) 6033.
- [44] E. Leveugle, L. V. Zhigilei, A. Sellinger, J. M. Fitz-Gerald, "Ejection of Matrix-Polymer Clusters in Matrix-Assisted Laser Evaporation: Course-Grained Molecular Dynamics Simulations," J. Phys. Conference Series 59, (2007) 126.
- [45] C. N. Hunter, M. H. Check, C. H. Hager, A. A. Voevodin, "Tribological Properties of Carbon Nanopearls Synthesized by Nickel-Catalyzed Chemical Vapor Deposition," Tribol. Lett., 30 (2008) 169.
- [46] J. E. B. Randles, "A Cathode Ray Polarograph. Part II.-The Current-Voltage Curves," Trans. Faraday. Soc. 44 (1948) 327.

- [47] A. Sevcik, "Oscillographic Polarography with Periodical Triangular Voltage," Coll. Czech. Chem. Commun. 13 (1948) 349.
- [48] R. S. Nicholson, I. Shain, "Theory of Stationary Electrode Polarography: Single Scan and Cyclic Methods Applied to Reversible, Irreversible, and Kinetic Systems," Anal. Chem. 36 (1964) 706.
- [49] M. Fleischmann, S. Pons, D. Rolison, P. Schmidt, "Ultramicroelectrodes," Datatech Systems, Inc., Science Publishers, 1987.
- [50] A. G. Ewing, M. A. Dayton, R. M. Wightman, "Pulse Voltammetry with Microvoltammetric Electrodes," Anal. Chem., 53 (1981) 1842.
- [51] R. M. Wightman, "Voltammetry with Microscopic Electrodes in New Dimensions," Science 240 (1988) 415.
- [52] G. Akchurin, B. Khlebtsov, G. Akchurin, V. Tuchin, V. Zharov, N. Khlebtsov, "Gold Nanoshell Photomodification under a Single Nanosecond Laser Pulse Accompanied by Color-Shifting and Bubble Formation Phenomena," Nanotechnology, 19 (2008) 1.
- [53] D. A. Jones, Principles and Prevention of Corrosion, 2nd ed., Printice-Hall, New Jersey, 1996, pp. 12, 50, 66, 79, 402, 532.
- [54] J. Ghilane, O. Fontaine, P. Martin, J. C. Lacroix, H. Randriamahazaka, "Formation of Negative Oxidation States of Platinum and Gold in Redox Ionic Liquid: Electrochemical Evidence," Electrochem. Comm., 10 (2008) 1205.
- [55] K. Tammeveski, T. Tenno, J. Niinisto, T. Leitner, G. Friedbacher, L. Niinisto, "Thermal Preparation of Thin Platinum Coatings and Their Electrochemical

- and Atomic Force Microscopic Characterization," *Appl. Surf. Sci.*, 156 (2000) 135.
- [56] K. Z. Yao, K. Karan, K. B. McAuley, P. Oosthuizen, B. Peppley, T. Xie, "A Review of Mathematical Models for Hydrogen and Direct Methanol Polymer Electrolyte Membrane Fuel Cells," *Fuel Cells*, 4 (2004) 3.
- [57] L. Qu, L. Dai, "Novel Silver Nanostructures from Silver Mirror reaction on Reactive Substrates," *J. Phys. Chem. B*, 109 (2005) 13985.
- [58] D. M. K. Lam, B. W. Rossiter, "Chromsokedasic Painting," *Sci. Am.*, 265 (1991) 80.
- [59] S. Artelt, H. Kock, D. Nachtigall, U. Heinrich, "Bioavailability of Platinum Emitted from Automobile Exhaust," *Toxicology Letters*, 96-97 (1998) 163.
- [60] J. Black, *Biological Performance of Materials - Fundamentals of Biocompatibility*, 2nd ed., Marcel Dekker, New York, 1992, p. 4.
- [61] H. P. Stallmann, C. Faber, H. M. Plokker, P. I. J. M. Wuisman, "Biodegradable X-Ray Markers of Controlled Radio-Opacity: Temporary Position Measurements in Bone," *Acta Orthopaedica*, 76 (2005) 122.
- [62] D. W. Trost, H. L. Zhang, M. R. Prince, P. A. Winchester, Y. Wang, R. Watts, T. A. Sos, "Three-Dimensional MR Angiography in Imaging Platinum Alloy Stents," *J. Magn. Reson. Imaging*, 20 (2004) 975.
- [63] D. Wang, S. J. Lippard, "Cellular Processing of Platinum Anticancer Drugs," *Nat. Rev. Drug Dis.*, 4 (2005) 307.

CHAPTER III

PLATINUM ABLATION AND PLUME CHARACTERIZATION

And I said to the man who stood at the gate of the year, "Give me a light that I may tread safely into the unknown." And he replied, "Go out into the darkness and put your hand into the hand of God. That shall be better to you than light and safer than a known way."

-Louise Haskins

Introduction

In 2001, Suzdalev and Suzdalev published an extensive review article on the methods used to prepare nanostructures [1]. They classified the synthesis methods into six groups with gas-phase nanoparticles formed by laser vaporization being one of them. Having cited 274 references, it was their conclusion that "[t]he ways of assembly of nanoclusters into nanostructures depend[ed] not only on the properties of separate nanoclusters and intercluster interactions but also on the methods used to prepare nanoclusters." [1]. They also speculated on the development of nanostructures for the fabrication of single electron devices. The ability to fabricate such a device would require the ability to minimize particle agglomeration, reduce overall particle size (< 100 nm), and control the resultant particle shape. Pulsed laser ablation synthesis of nanoparticle materials was reported in the literature review found in Chapter 2 [2-

6]. However, achieving the desired particle separation and morphology was a problem with these conventional ablation processes and mitigated the use of the resultant structure for single electron processes. The work described in this dissertation is the first to report the ability to fabricate nano-sized particles via the modified form of PLA denoted Through Thin Film Ablation (TTFA) with the purpose of creating a collection of well dispersed nanoelectrodes that can act as a probe to detect the ferricyanide electroactive species. The focus of this chapter is on the ablation process and the techniques used to indirectly monitor the formation of Pt species in the plume [7].

Experimental

An A300 magnetron sputtering system manufactured by AJA International was used to sputter a thin film (TF) of Pt from a Pt foil (Ladd Research; Williston, VT) onto a 50 mm diameter by 4 mm thick UV transparent fused silica support to be used as a UV transparent TTFA target (Figure 3.1). Ablation was conducted with TF thicknesses of 5, 10, and 20 nm. Irradiation was performed through the back side of the target with a krypton fluoride (KrF) excimer laser (LPX200i, Lambda Physik, $\lambda=248$ nm) oriented at 45° to the target. Platinum species were released from the front side of the TF by means of adiabatic expansion and deposited downstream onto a silicon (Si) substrate surface (Figure 3.2).

Following TTFA, Pt TF remnants remaining on the silica support were removed by cleaning in aqua regia, a 1:3 ratio mixture of concentrated nitric acid

(HNO₃) to concentrated hydrochloric acid (HCl). Etching the target with dilute hydrofluoric acid (HF) removed any damage to the target resulting from high laser energy densities ($> 0.6 \text{ J/cm}^2$). Cleanability and reusability of the target, especially at laser energy densities equal to or less than 0.6 J/cm^2 contributed to the overall robustness of the method.

A schematic of the instrumentation setup used for ion current, emission spectroscopy, and time of flight (TOF) measurements is shown in Figure 3.3. A 250 mm focusing lens was placed 172 mm before the target as a way to adjust the laser energy density on the surface of the target. The ions sampled from the Pt plume were collected during the TTFA process by a Faraday cup placed 16 cm from the target and detected using a 50 ohm (Ω) input resistance, the voltage across which was measured and recorded as a function of time using a digital oscilloscope [7]. A SpectraPro 150 Acton Research monochromator and an HR2000 Ocean Optics optical emission spectrometer calibrated against a LS-1-CAL tungsten halogen light source, a blackbody lamp of known color temperature (3100 K), were used to disperse the Pt emitted radiation and to acquire absolute irradiance spectra. The optical emission spectrometer was connected to an optical fiber that was placed behind another lens and light collection system 7mm from the target. A gated ICCD camera capable of rapidly collecting plume images was used to record the time evolution of the Pt TTFA synthesis process. A R7400U-04 Hamamatsu photomultiplier tube (PMT) was

positioned 25 mm downstream from the target to allow the ablated species time of flight distribution to be collected, from which the speed was calculated.

Results and Discussion

The Pt TTFA plume was evaluated for divergence, directionality, and temperature and for radiation emitted from the excited Pt species in various growth environments. The TTFA plume shown in Figure 3.4 was less divergent and more directional than plumes typically observed for conventional PLA processes [7]. A TOF distribution of ion current is presented in Figure 3.5. This data, which was collected with the Faraday cup, was obtained from Pt TTFA plume in vacuum using a single laser pulse. The TTFA target used for this measurement contained a 20 nm Pt TF. As the fast photoelectrons (ns) had a much higher speed than that of the ions, and thus were not seen in this data, the negative amplitude of the ion current observed at approximately 54 μ s indicated the ions detected by the Faraday cup were negatively charged.

One possible explanation for the observation of negative ions is that at the point of ablation, space charge forces build up and a localized layer of positive charge is formed at the front surface of the target. Yushkov et al. in their 2000 article on ion velocities [8] described that, if this is the case, then for the same element different ion-charge states would result in slightly different velocities because the same pressure gradient is experienced by all ions. This interpretation indicated that positive ions would also be observed. Their data

implied a correlation existed between the elemental ion velocity and charge state suggesting ion acceleration was based on pressure gradients coupled with electron-ion friction.

A speed for the detected negative ions was calculated by dividing the flight time for the observed peak into the distance traveled (16 cm). The corresponding speed was 3.0 km/s. From this information, the ratio of ionized Pt per ablated Pt atom was calculated, as shown in Appendix A, to be 2.0×10^{-7} ions/atom. This small number implies TTFA is a gentle method of ablation.

Shown in Figures 3.6a and 3.6b are the optical emission results. The red and purple curves are the emission data for the vacuum and 5 Torr argon ablations, respectively. The blue curves represent a fit of the emission spectra using the blackbody formula, derived from Planck's Law

$$I(\lambda, T) = (2hc^2/\lambda^5)(1/e^{(hc/\lambda kT)} - 1) \quad (3.1)$$

to estimate the temperature of the emitting species in vacuum and 5 Torr argon. The results indicated that the temperature of the emitted species was 2940 K in vacuum and 2938 K in 5 Torr argon. The melting and boiling point of platinum are 2042 K (T_m) and 4443 K (T_b), respectively. Thus, emission spectroscopy of ablated species in either environment suggested TTFA produced "liquefied" platinum with an average temperature of approximately 2939 K.

The corresponding emission spectra from the Pt TTFA plume in vacuum are shown in Figure 3.7 for (a) 6 μ s, (b) 8 μ s, (c) 10 μ s, (d) 20 μ s, (e) 200 μ s, and (f) 400 μ s delay after the laser pulse. Positive peaks at different relative

intensities were noted at various wavelengths, such as approximately 300 nm, 303 nm, 306 nm and 310 nm in Figure 3.7a, 390 nm in Figure 3.7b, 387 nm, 404 nm, and 412 nm in Figure 3.7c, 311 nm in Figure 3.7d, 578 nm, 584 nm, and 587 nm in Figure 3.7e, and 533 nm, 540 nm, and 547 nm in Figure 3.7f. The sharp peaks at 300 nm and 390 nm were indicative of atomic platinum being released during ablation in vacuum [9]. The remaining broad peaks were molecular Pt. It is important to note the absence of Pt species in Figure 3.8. At 800 μ s to 1000 μ s delays, only blackbody radiation was observed.

Presented in Figures 3.9a and 3.9b are the Pt TOF data measured by the PMT for ablation carried out in vacuum and in 5 Torr argon, respectively. Ablation performed in vacuum (Figure 3.9a) produced a sharp peak at a flight time of 8 μ s in addition to a broad peak at the longer flight times. Ablation in low pressures of argon (i.e. 500 mTorr and 1 Torr) gave PMT TOF results similar to vacuum ablation (results not shown). At a pressure of 5 Torr argon, no sharp peaks and only broad peaks at longer flight times (a broad peak between 75-225 μ s and another between 450-600 μ s), were observed (Figure 3.9b). At higher argon pressure (10 Torr), only a broad peak centered at 200 μ s was observed (data not presented). Since the PMT was located 25 mm from the target, a speed of 3.18 km/s was calculated for the sharp peak observed at 8 μ s in Figure 3.9a. This speed corresponded to that which was calculated based on ionic currents (3.00 km/s, Figure 3.5). The PMT TOF observations in addition to the

ion current TOF and emission results suggested, indirectly, that the sharp peaks at early flight times were due to atomic Pt.

Shown in Figures 3.10 and 3.11 are the time delayed series of plume images of the Pt TTFA process recorded with a high speed camera after the ablation laser pulse in vacuum and 5 Torr argon, respectively. In both cases, the release of fast moving ablated material from the front side of the target was observed in the propagation of the TTFA plume with time. In Figure 3.11, the addition of a slower moving species was observed after 100 μs delay in 5 Torr argon. The addition of argon to the TTFA process enabled the ablated Pt atoms observed in vacuum ablation (Figure 3.9a) to collide with background gas and recombine to maximize formation of nanoparticles in the gas phase as evidenced by the two peaks in Figure 3.9b at approximately 150 μs and 500 μs . Together these results corroborate the PMT data discussed previously and also suggest TTFA performed in the presence of argon produced two populations of nanoparticles. Not only is the radiation emitted from the ablated Pt species in vacuum (Figure 3.9a) different from that in argon (Figure 3.9b), but collision with the background gas produced nanoparticles with differing speeds.

Summary

Plume characterization data provided indirect evidence that the highly directional plume produced by the TTFA synthesis process produced an abundance of "liquefied" nanoparticles with different speeds when conducted in

the presence of argon. This result was the more favorable compared to vacuum ablation in terms of maximizing particle density for the production of Pt nanoelectrodes.

References

- [1] I. P. Suzdalev, P. I. Suzdalev, "Nanoclusters and Nanocluster Systems. Assembling, Interactions, and Properties," *Russian Chem. Rev.*, 70 (2001) 177.
- [2] K. S. Seol, R. P. Camata, K. Takeuchi, "Study on the Formation of Silicon Nanoparticles during Laser Ablation Using a Low Pressure Differential Mobility Analyzer," *J. Aerosol Sci.*, 30 (1999) S467.
- [3] F. Mafune, J. Kohno, Y. Takeda, T. Kondow, "Formation of Stable Platinum Nanoparticles by Laser Ablation in Water," *J. Phys. Chem. B*, 107 (2003) 4218.
- [4] F. Mafune, J. Kohno, Y. Takeda, T. Kondow, "Nanoscale Soldering of Metal Nanoparticles for Construction of Higher-Order Structures," *J. Am. Chem. Soc.*, 125 (2003) 1686.
- [5] M. R. Davidson, Y. Fan, G. J. Berry, J. A. Cairns, A. G. Fitzgerald, "Analysis of Laser Irradiated Organo-Platinum Films," *Mikrochim. Acta*, 139 (2002) 43.
- [6] G. Akchurin, B. Khlebtsov, G. Akchurin, V. Tuchin, V. Zharov, N. Khlebtsov, "Gold Nanoshell Photomodification under a Single-Nanosecond Laser Pulse Accompanied by Color-Shifting and Bubble Formation Phenomena," *Nanotechnology*, 19 (2008) 1.
- [7] P. T. Murray and E. Shin, "Formation of Silver Nanoparticles by Through Thin Film Ablation," *Mater. Lett.*, 62 (2008) 4336.

- [8] G. Y. Yushkov, A. Anders, E. M. Oks, I. G. Brown, "Ion Velocities in Vacuum Arc Plasmas," J. Appl. Phys. 88 (2000) 5618.
- [9] Ralchenko, Yu., Kramida, A.E., Reader, J., and NIST ASD Team (2008). NIST Atomic Spectra Database (version 3.1.5), [Online]. Available: <http://physics.nist.gov/asd3> [2009, May 20]. National Institute of Standards and Technology, Gaithersburg, MD.

Figures

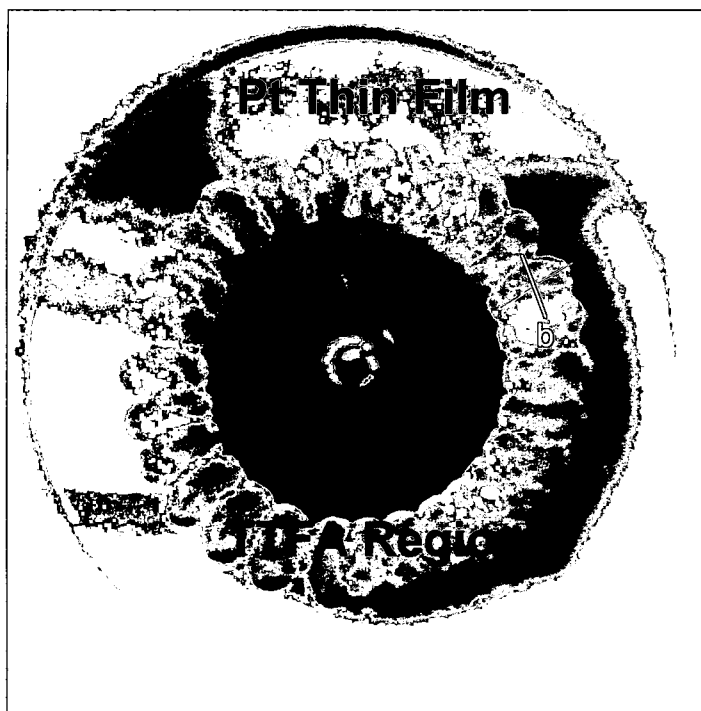


Figure 3.1. Optical photograph of fused silica target after Pt TTFA. Laser footprint is 2.0 cm by 1.2 cm, denoted a and b respectively, having an area of 2.4 cm².

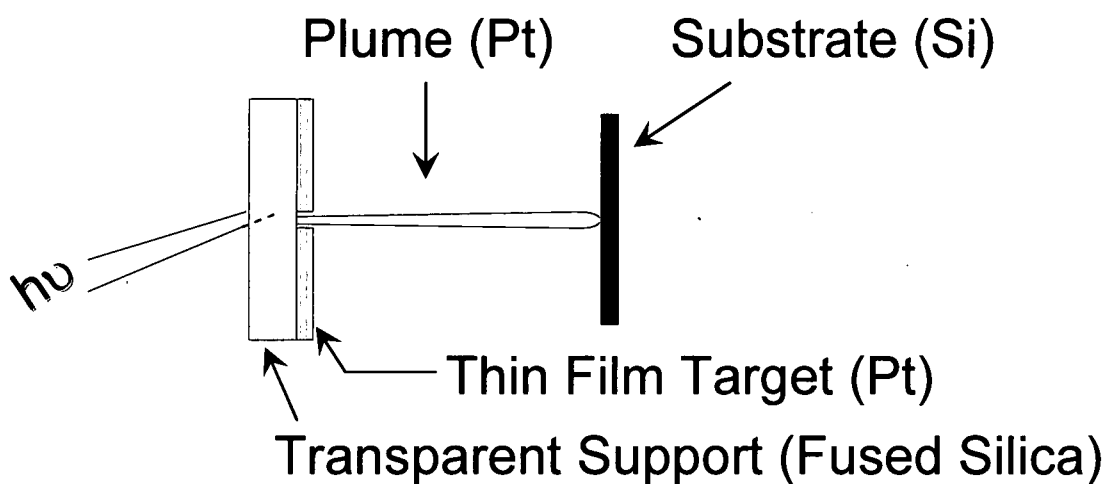


Figure 3.2. Ablation setup for TTFA synthesis.

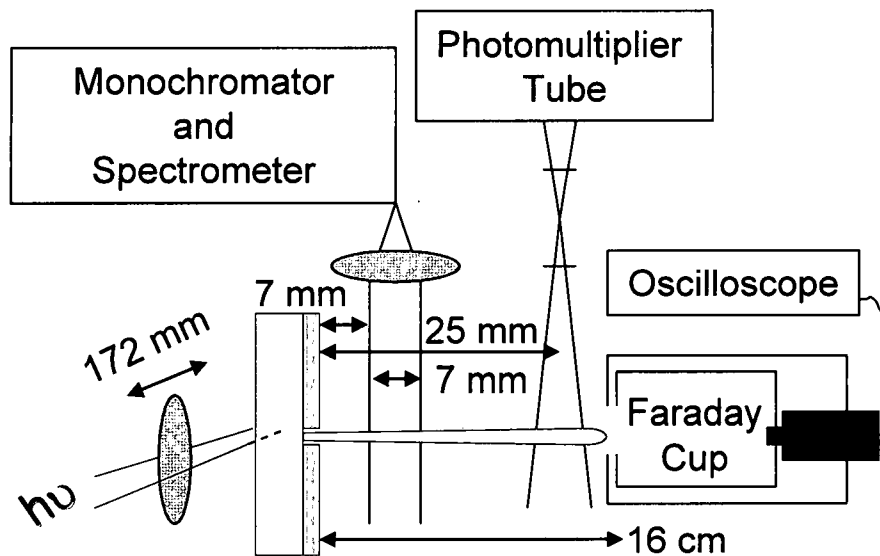


Figure 3.3. Instrumentation setup for ion current, emission spectroscopy, and time of flight measurements.

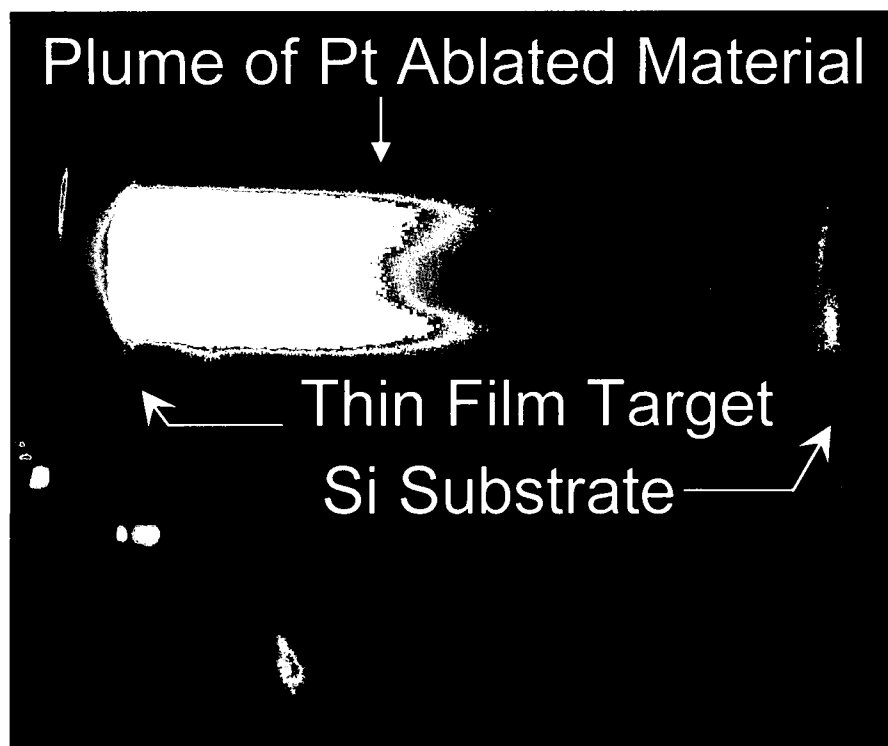


Figure 3.4. Photograph of Pt plume in vacuum.

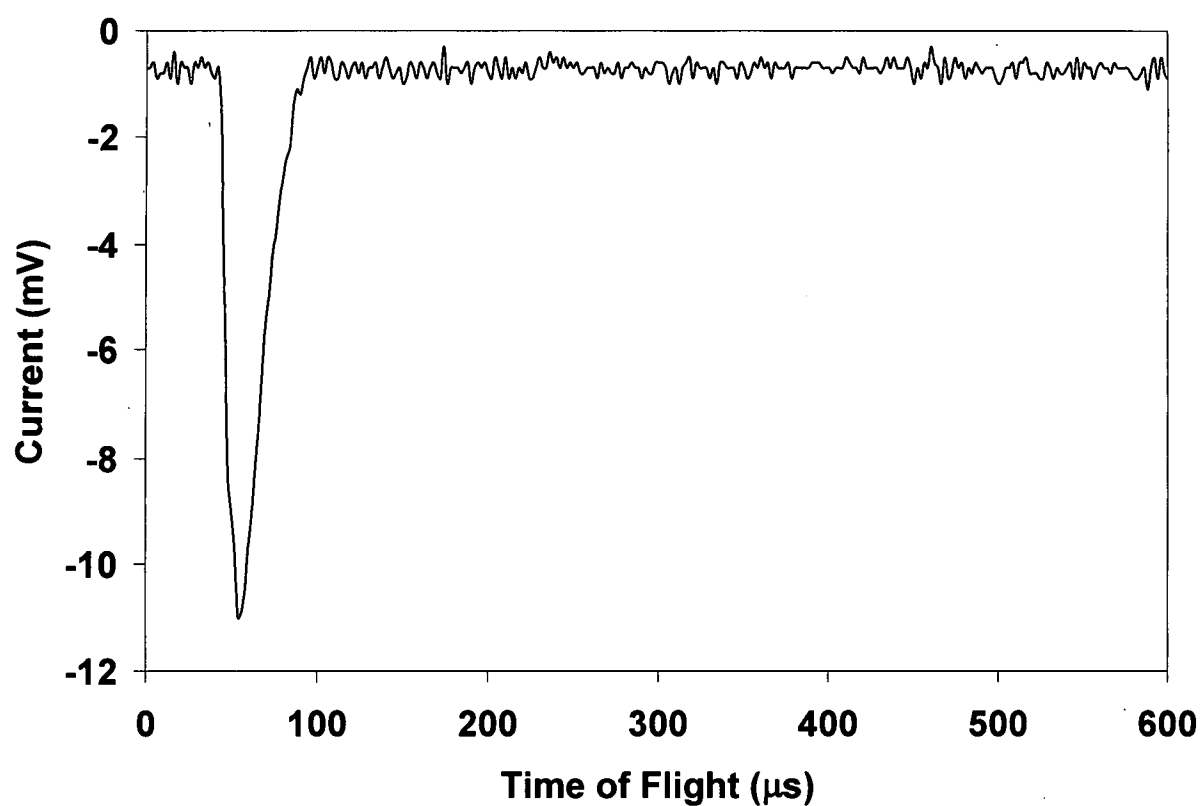
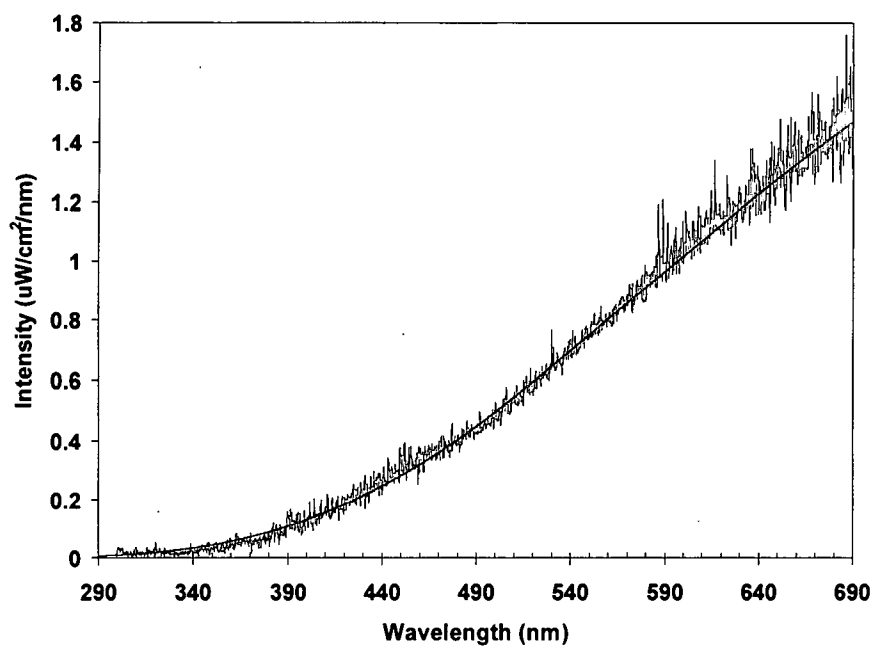
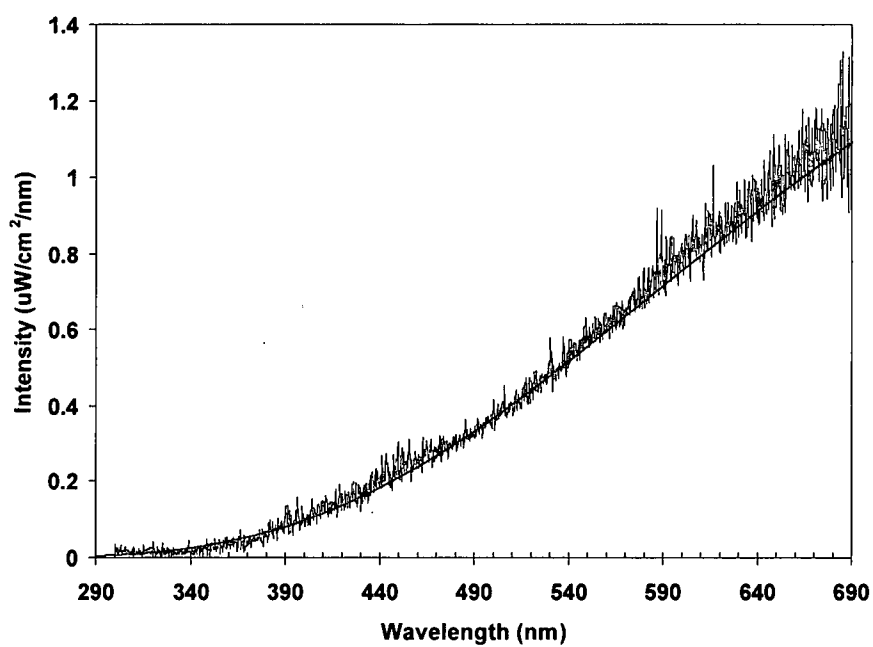


Figure 3.5. Time of flight spectrum of ion currents measured from Pt TTFA plume in vacuum.

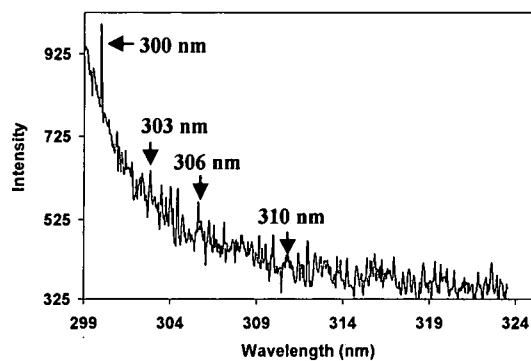


(a)

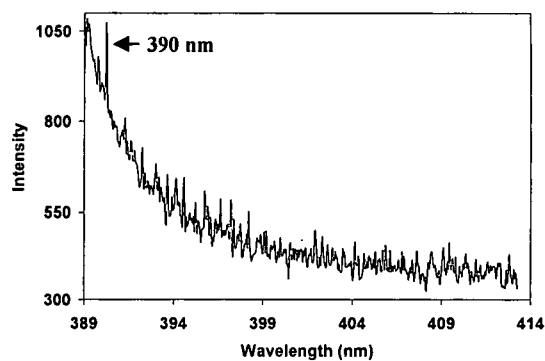


(b)

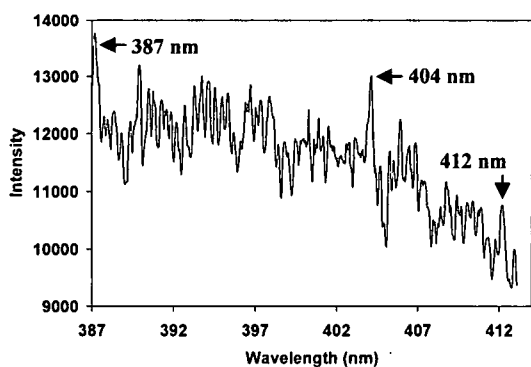
Figure 3.6. Temperature of Pt plume produced via TTFA in (a) vacuum, $T=2940\text{K}$ and (b) 5 Torr argon, $T=2938\text{K}$. The blue curve is a fit of the emission spectra (red and purple curves) using the blackbody formula.



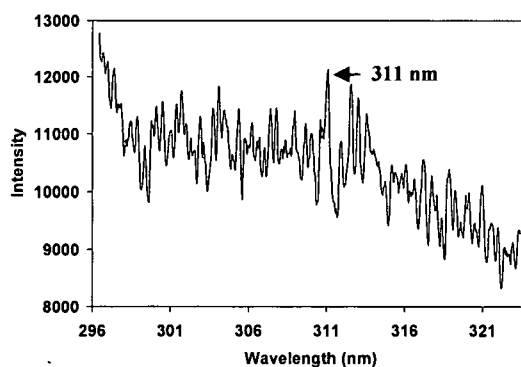
(a)



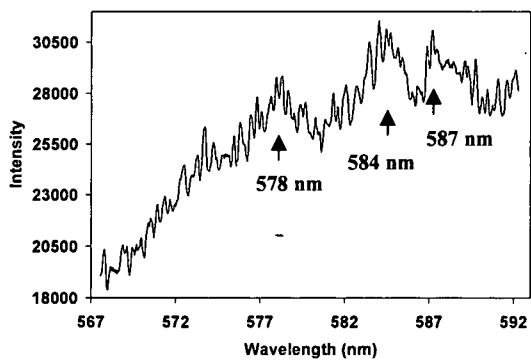
(b)



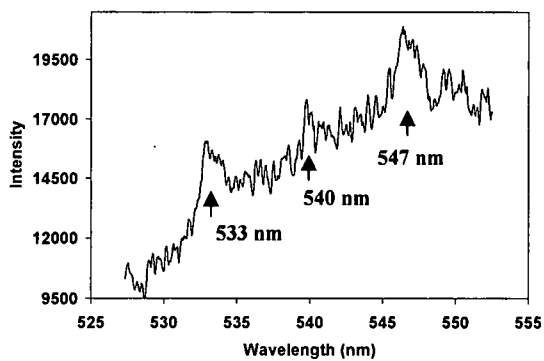
(c)



(d)

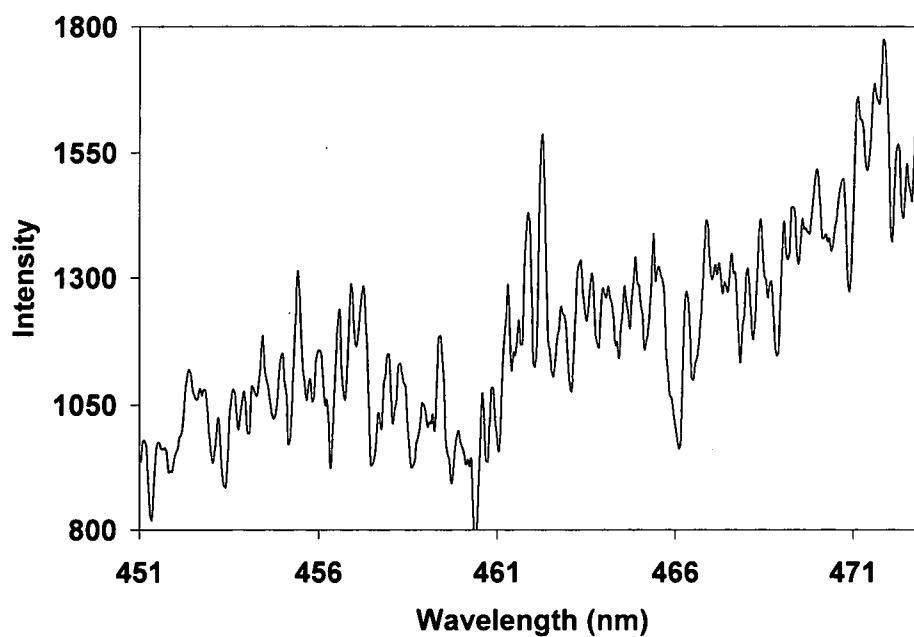


(e)

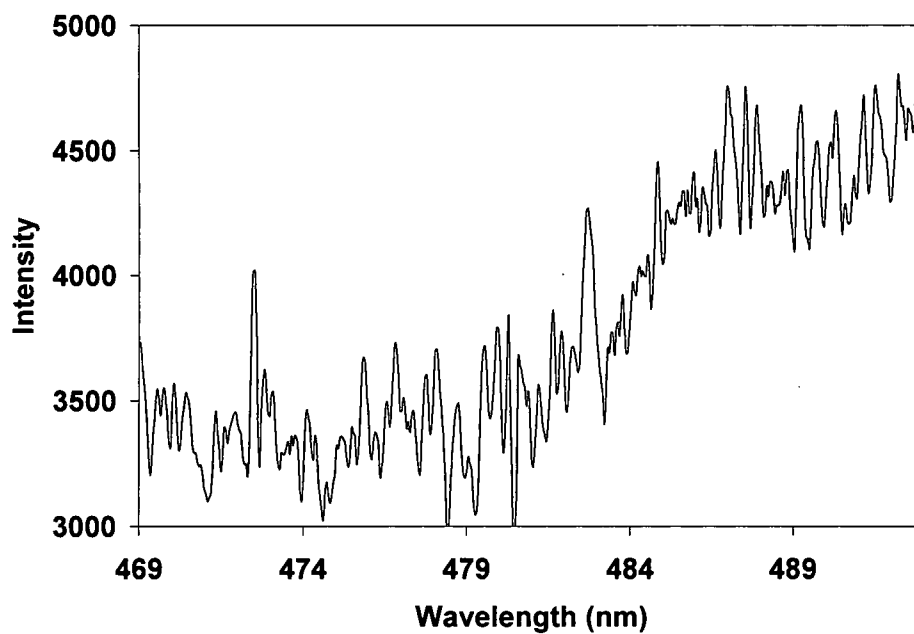


(f)

Figure 3.7. Emission spectra from Pt TTFA plume in vacuum at (a) 6 μ s delay, (b) 8 μ s delay, (c) 10 μ s delay, (d) 20 μ s delay, (e) 200 μ s delay, and (f) 400 μ s delay.

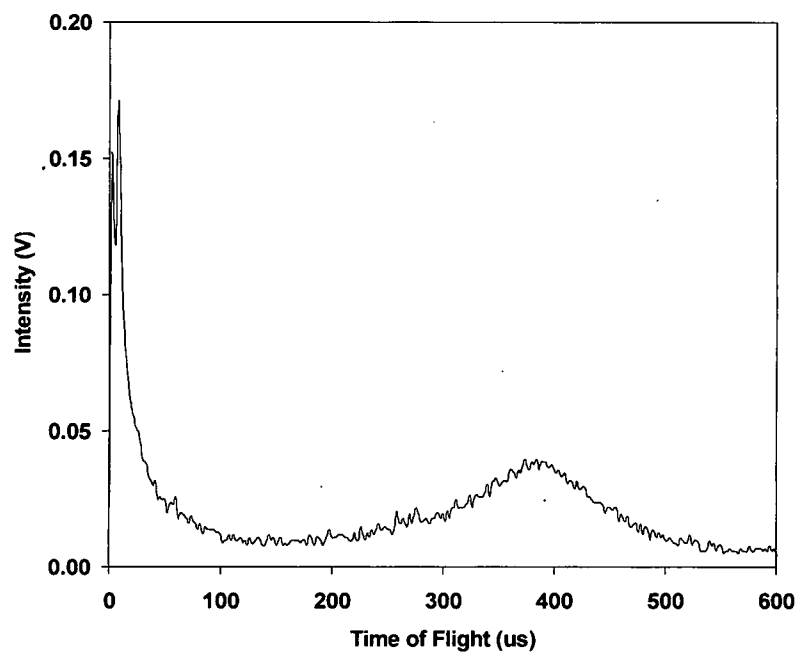


(a)

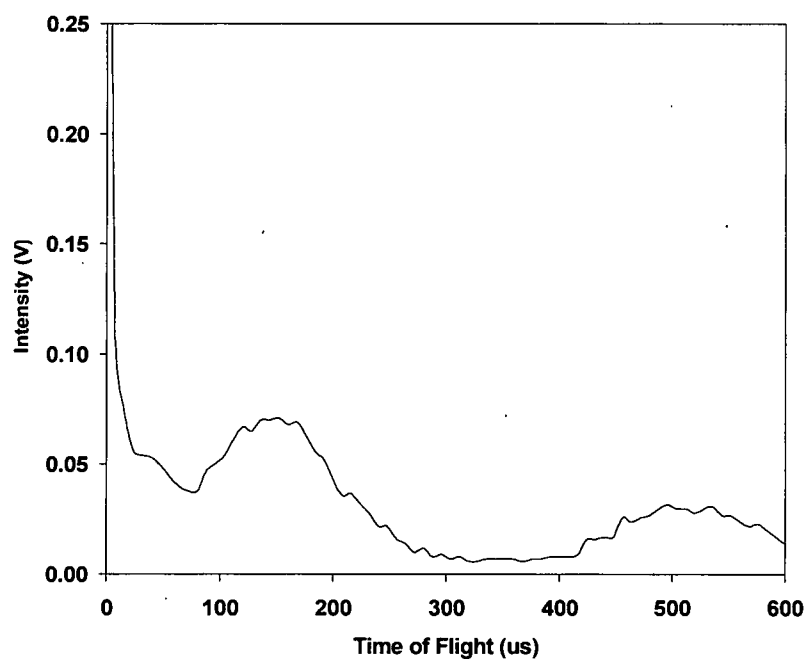


(b)

Figure 3.8. Emission spectra from Pt TTFA plume in vacuum at (a) 800 μs delay and (b) 1000 μs delay.



(a)



(b)

Figure 3.9. Time of flight spectrum of Pt during TTFA in (a) vacuum and (b) 5 Torr argon.

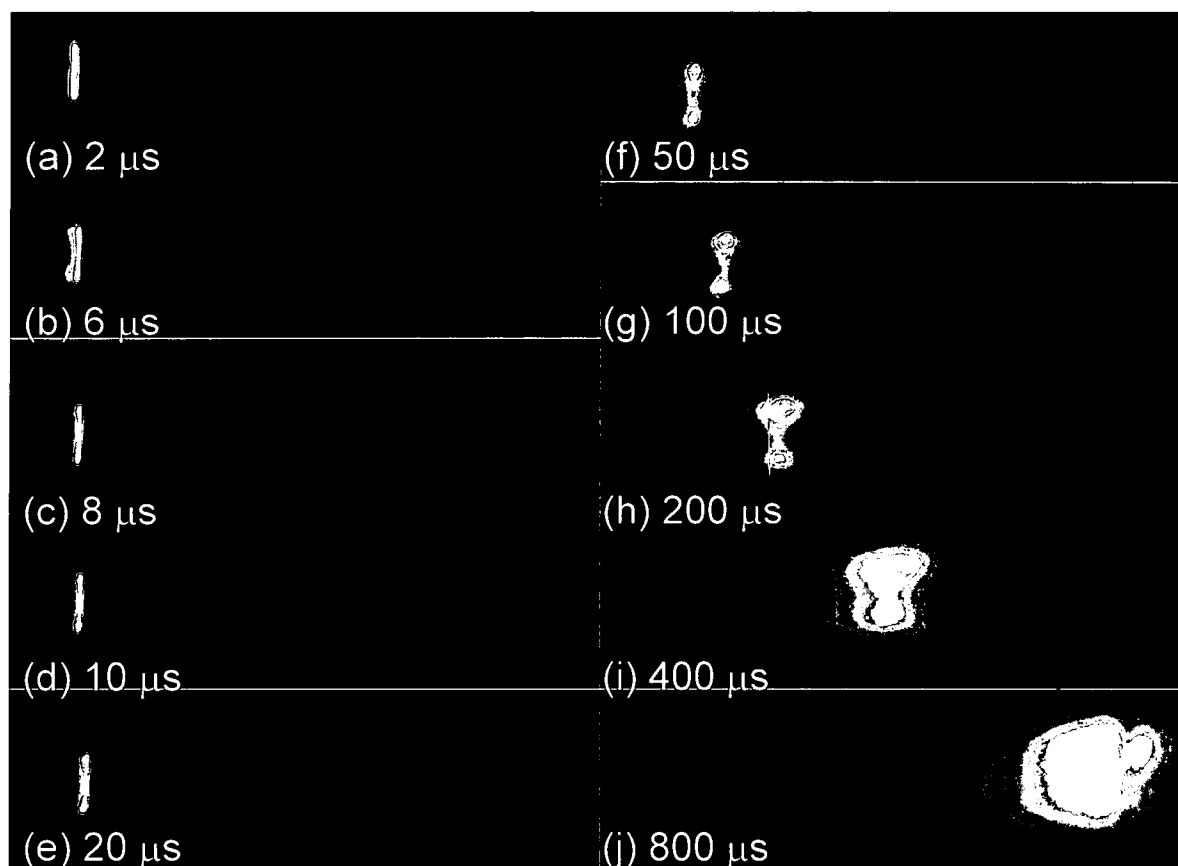


Figure 3.10. Propagation of TTFA plume in vacuum as a function of time over a distance of 25 mm.

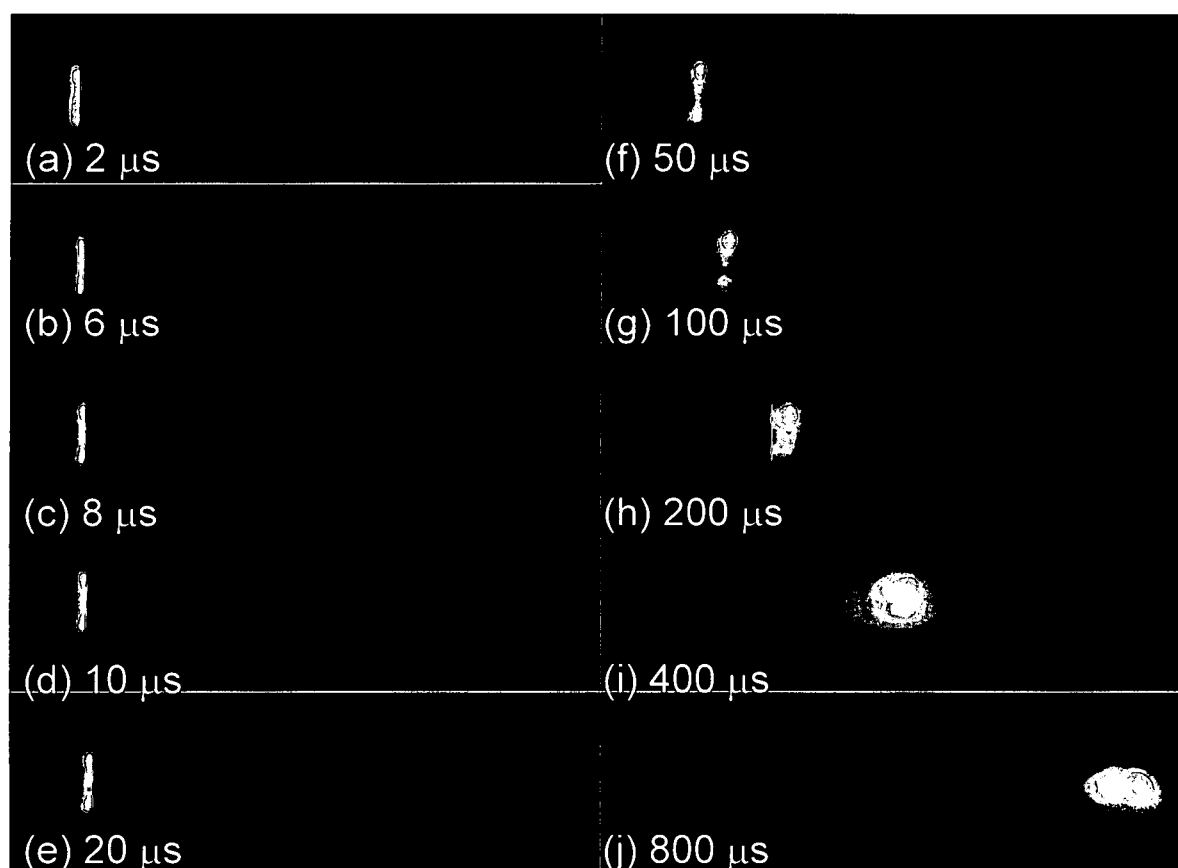


Figure 3.11. Propagation of TTFA plume in 5 Torr argon as a function of time over a distance of 25 mm.

CHAPTER IV

MORPHOLOGY OF NANO-ELECTRODES

You gain strength, courage, and confidence by every experience in which you really stop to look fear in the face.... You must do the thing which you think you cannot do.

-Eleanor Roosevelt

Introduction

Platinum nanoparticles have promising applications as nanoelectrodes due to their unusual electrochemical properties. It was believed that the electrochemical properties and nanoelectrode performance depended on the size distribution and number density of nanoparticles. Thus, adjustments of the laser deposition parameters were made to improve Pt nanoparticle, and therefore, nanoelectrode process control by optimizing the particle population density and morphology. The extent of nanoparticle agglomeration and sample morphology was determined by microscopic examination.

Experimental

Nanoparticles of Pt were deposited by TTFA onto 3 mm carbon-coated copper (Cu) transmission electron microscopy (TEM) grids (Part Number CF-400-Cu, Electron Microscopy Sciences). The grids were mounted to Si

substrates and removed prior to particle analysis. Due to the number of ablation parameters, a two level (i.e. maximum and minimum parameter setting) fractional factorial design with fold over (reversal of parameter settings) was chosen to identify which parameters or factors had the largest effect on size distribution and number density of nanoparticles. Replicate ablations were conducted with TF thickness of 5, 10, and 20 nm and were performed in vacuum (5.0×10^{-7} Torr) and varying pressures of background argon gas (5 or 10 Torr), making use of either single shot (SS) or multiple shot (4S = 4 shots) laser pulses. Laser energy densities were maintained at either 500 or 600 mJ/cm². The substrate was located 50 or 75 mm from the target.

A Hitachi H-7600 transmission electron microscope was used to image the Pt nanoparticles resulting from each ablation condition at magnifications up to 150,000x using an accelerating voltage of 100 kV. The micrographs were examined for particle size distribution and density. A Hitachi S-4800 high resolution scanning electron microscope (HRSEM) was used to perform routine checks of Pt TTFA deposition parameters onto Si substrates. Accelerating voltages, magnifications, and working distances were varied to achieve the best micrographs. Atomic force microscopy (AFM) measurements of Pt nanoparticles was performed to provide information regarding Pt nanoparticle height. A Digital Instruments/Veeco Metrology Dimension 3000 Scanning Probe System equipped with DNP-S20 silicon nitride tips (nominal tip diameter of 15 nm) and operating with a 0.12 N/m spring constant was used. Particle height information was

instrumental in assessing whether or not the synthesized nanoparticles produced sufficiently planar nanoelectrodes. The microscopic techniques were also used to examine the shape and overall uniformity of the nanoparticles.

Results and Discussion

Displayed in Figures 4.1 and 4.2 are the TEM micrographs and size distributions, respectively, of Pt nanoparticles deposited by TTFA (a) in vacuum and (b) in 5 Torr argon on carbon-coated Cu TEM grids. The nanoparticles were analyzed for size, shape, and density. The synthesized nanoparticles were nonagglomerated for both growth environments. In comparison to ablation performed in argon, which produced a low density of small particles (i.e. 1-3 nm) that were more regular (i.e. round) in shape, vacuum ablation produced Pt islands of larger and irregular dimensions. The irregular surface features observed in the micrographs for the vacuum growth may result from the coalescence of smaller atoms to make larger aggregates of atomic Pt species on the surface of the substrate. The observation of atomic Pt emission lines during vacuum ablation was discussed in Chapter 3 and provided evidence that atomic Pt species had been formed. A similar phenomenon was reported for silver (Ag) in vacuum which indicated a thin film of material was deposited on the substrate due to recombination of ablated atoms on the substrate surface [1].

The series of micrographs shown in Figures 4.3a and 4.4a were taken from samples grown only in an argon environment. For substrates positioned

close to the target at 50 mm (instead of 75 mm) and subjected to multiple laser pulses (4S) with higher laser energies (0.6 J/cm^2), it can be seen that TTFA of Pt occurring at lower pressures of argon gas (5 Torr) exhibited a greater density of Pt nanoparticles with less overall separation, regardless of target thickness (10 vs. 20 nm). These "optimum ablation parameters" produced a collection of nanoparticles ranging in diameter between 1 and 10 nm, averaging 3 nm in size (Figures 4.3b and 4.4b). From the size distributions at optimum ablation parameters, it was calculated that approximately 500 Pt nanoparticles were available in a $0.1 \text{ }\mu\text{m}^2$ area. Thus, approximately 5.0×10^{11} Pt particles/ cm^2 were deposited onto the substrate. This result meant that not all of the nanoparticles being ablated per laser pulse (calculated in Appendix A to be 2.4×10^{14}) were being captured by the substrate. It is speculated that the remaining particles are going into the surrounding area of the ablation chamber. When TTFA was conducted at a slightly higher pressure of argon (10 Torr), even fewer nanoparticles (8.8×10^{10} Pt particles/ cm^2) were detected as compared to 5 Torr argon (5.0×10^{11} Pt particles/ cm^2).

Ablations with the 5 nm TF target produced agglomerated (Figure 4.5, micrograph 1) or insufficient quantities (Figure 4.5, micrographs 2-4) of Pt nanoparticles and were omitted from the final test matrix of experiments shown in Table 4.1. White light interferometry (WLI) measurements of the target indicated that 5 nm films did not supply enough Pt material to sufficiently coat the fused silica target, given its roughness and overall topography.

Scanning electron micrographs of Pt nanoparticles deposited onto Si substrates using non-optimum TTFA parameters are shown in Figure 4.6. Examination of these large particles perpendicular to the electron beam suggested they were round (Figure 4.6a); however, examination of particles when tilted suggested that although they were round, the particles were also flat (pancake-like) (Figure 4.6b). Indeed, particle height (Z-axis) and line profile measurements obtained from AFM confirmed that the Pt nanoparticles were not as tall as they were wide (Figure 4.7). The particle heights ranged from 0.5 - 0.7 nm or averaged approximately 0.6 nm tall. It is speculated that the amount of energy available in a Pt nanoparticle at the average temperature of the plume, which was identified in Chapter 3 to be approximately 2939 K, played a role in the ability of the liquefied nanoparticles to wet, cool, and adhere to the Si substrate.

Based on the additive property for the change in enthalpy (ΔH), the enthalpy during the melting transition ($\Delta H_1 = 32.8 \text{ kJ/mol}$) and the cooling transition ($\Delta H_2 = 61.2 \text{ kJ/mol}$) were calculated. These calculations used the heat capacity (C_p) of liquid Pt ($C_{p_l} = 187 \text{ J kg}^{-1} \text{ K}^{-1}$) [2] going from 2939 K (Pt T_l) to 2042 K (Pt T_m) and the C_p of solid Pt ($C_{p_s} = 180 \text{ J kg}^{-1} \text{ K}^{-1}$) [2] going from Pt T_m to room temperature (298 K) according to the formula

$$\Delta H = C_p \Delta T \quad (4.1)$$

where dH is in kJ/mol, C_p is in $\text{J kg}^{-1} \text{ K}^{-1}$, and the change in temperature (ΔT) is in K. The addition of the heat of fusion for Pt ($\Delta H_{\text{fus}} = \Delta H_3 = 19.7 \text{ kJ/mol}$) gave a

total change in enthalpy of 113.7 kJ/mol for Pt having an atomic mass of 195 g/mol. If this reaction was exothermic in nature, based on the calculation for ΔH_1 presented in Appendix B, then for a Pt nanoparticle having an average diameter of 3 nm or 1300 atoms during the melting transition it would have an estimated energy of 443.8 eV. Thus, the heat of fusion and heat capacities for platinum as a function of temperature supplied enough energy for the platinum to wet and adhere to the substrate. Additionally, the optimum laser energy of 600 mJ/pul going into the target was more than sufficient then the necessary 7.1×10^{-14} mJ required for removal of the Pt TF from the target.

Summary

That TTFA is a feasible method of synthesizing Pt nanoparticles is presented in this chapter. The isolated particles produced by the TTFA method were sufficiently small and were sufficiently separated to be used as a collection of nanoparticles. The conventional PLA processing method [1] obviated using the resultant nanoparticles as nanosensors because the particles were entangled with their nearest neighbor. The TTFA method dramatically minimized the extensive agglomeration observed by conventional PLA processing when conducted with 10 and 20 nm Pt TF targets. To maximize Pt nanoparticle formation, TTFA syntheses were conducted in the presence of argon to produce Pt nanoparticles with smaller dimensions overall and more uniform shape.

In addition to the presence of background gas, positioning the substrate closer to the target (50 mm) and increasing the laser energy (600 mJ/pul) and number of laser pulses (4S) contributed to the identification of optimum TTFA parameters to prepare planar nanometer-scaled Pt electrodes of sufficient size (3 nm), shape, and population density. Ablation with the 5 nm TF target, when all other parameters were optimum, resulted in agglomeration. Ablation with the 5 nm TF target, when all other parameters were not optimum, produced insufficient quantities of Pt nanoparticles. Too few particles were not a desired result to move forward with the production of nanoelectrodes from a 5 nm TF target. Additionally, the irregular shape observed for vacuum ablation mitigated further use of this parameter in future experimentations. Thus, the final matrix of ablation parameters carried through to the compositional and electrochemical assessment is found in Table 4.1. It is anticipated that controlling the morphology, size, and density of TTFA synthesized Pt nanoparticles will lead to their use as nanoelectrodes with optimal electrochemical performance in the next two portions of this study.

References

- [1] P. T. Murray and E. Shin, "Formation of Silver Nanoparticles by Through Thin Film Ablation," *Mater. Lett.*, 62 (2008) 4336.
- [2] B. Wilthan, C. Cagran, C. Brunner, G. Pottlacher, "Thermophysical Properties of Solid and Liquid Platinum," *Thermochim. Acta*, 415 (2004) 47.

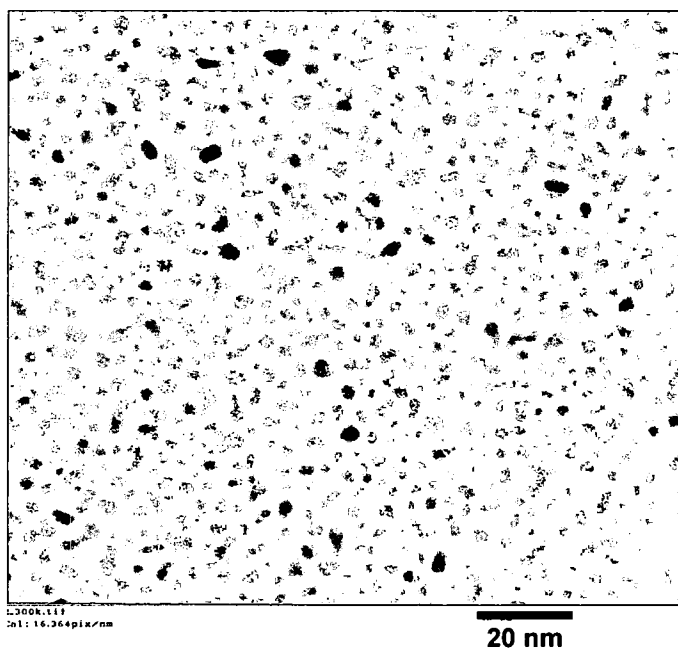
Table

Table 4.1

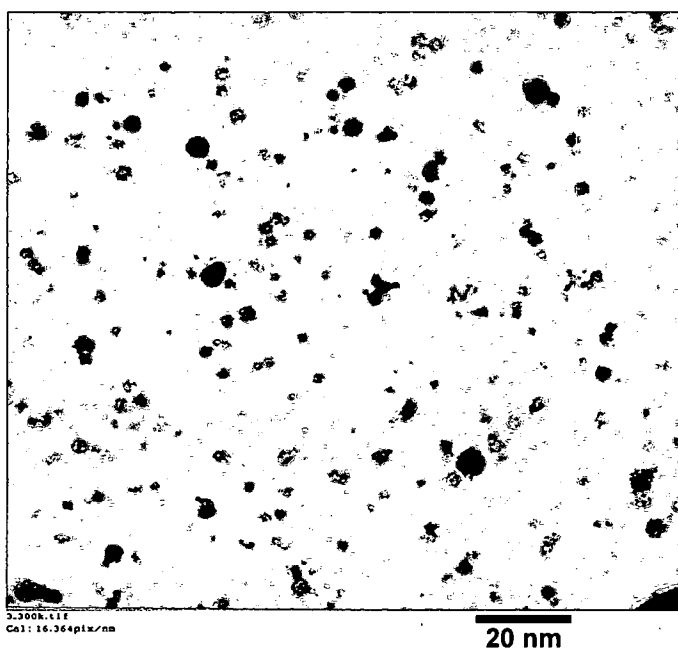
Platinum Through Thin Film Test Matrix

Run No.	Target Thickness (nm)	Ablation Environment (torr)	Laser Energy (mJ/pul)	Laser Pulse (shots)	Target-Substrate Distance (mm)	Post Anneal Temperature (°C)
1	20	5	500	4	75	410
2	10	5	500	1	50	410
3	20	10	500	1	75	As Deposited/Unannealed
4	10	10	500	4	50	As Deposited/Unannealed
5	20	5	600	4	50	As Deposited/Unannealed
6	10	5	600	1	75	As Deposited/Unannealed
7	20	10	600	1	50	410
8	10	10	600	4	75	410
9	20	10	600	1	50	As Deposited/Unannealed
10	10	10	600	4	75	As Deposited/Unannealed
11	20	5	600	4	50	410
12	10	5	600	1	75	410
13	20	10	500	1	75	410
14	10	10	500	4	50	410
15	20	5	500	4	75	As Deposited/Unannealed
16	10	5	500	1	50	As Deposited/Unannealed

Figures

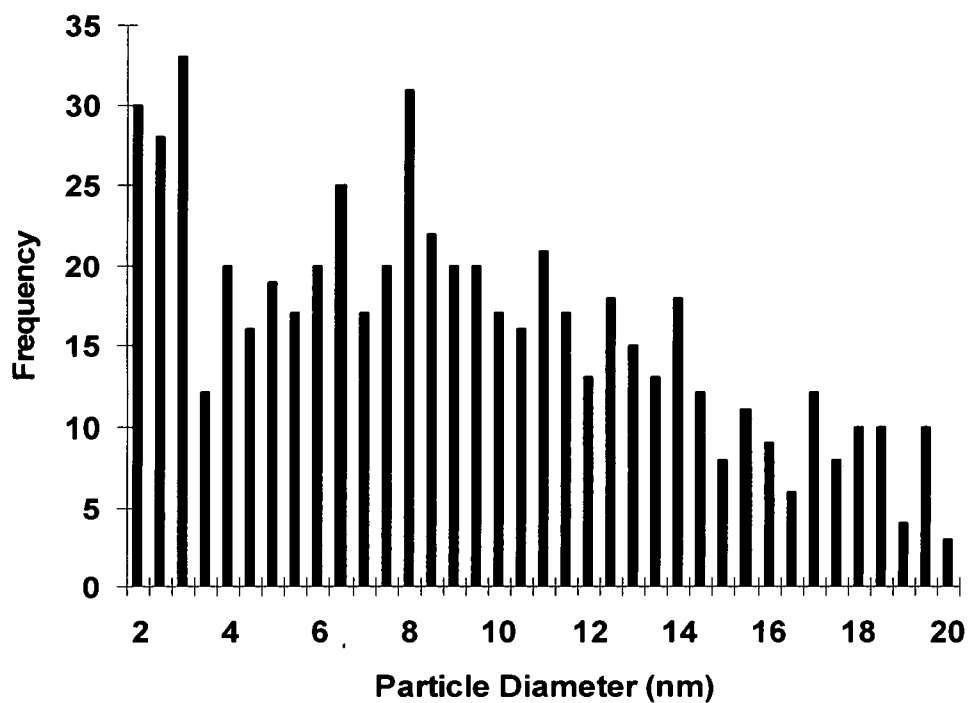


(a)

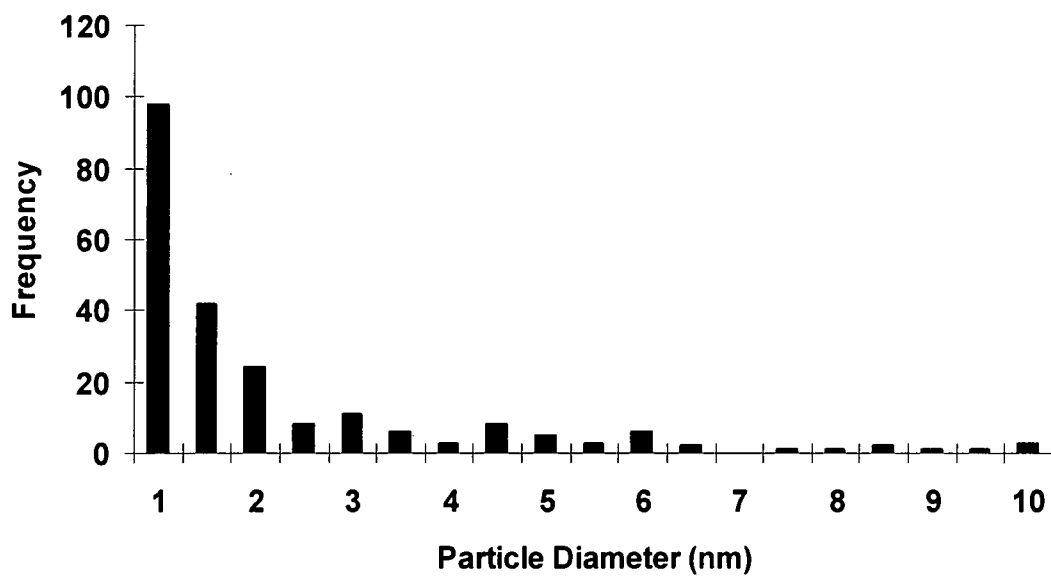


(b)

Figure 4.1. Micrograph images (magn. 150k, $0.1 \mu\text{m}^2$) of Pt nanoparticles from TTFA in (a) vacuum and (b) 5 Torr argon.

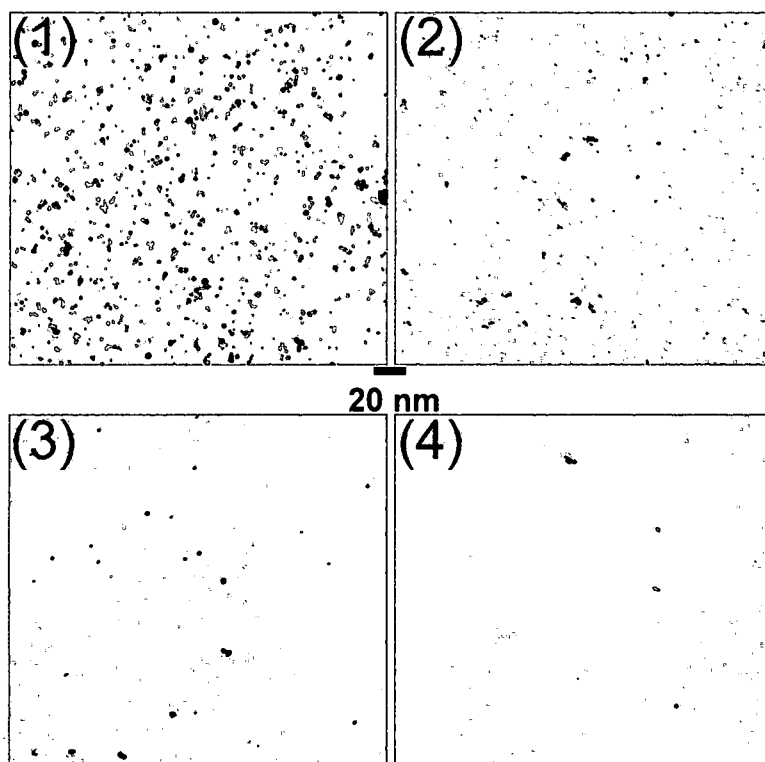


(a)

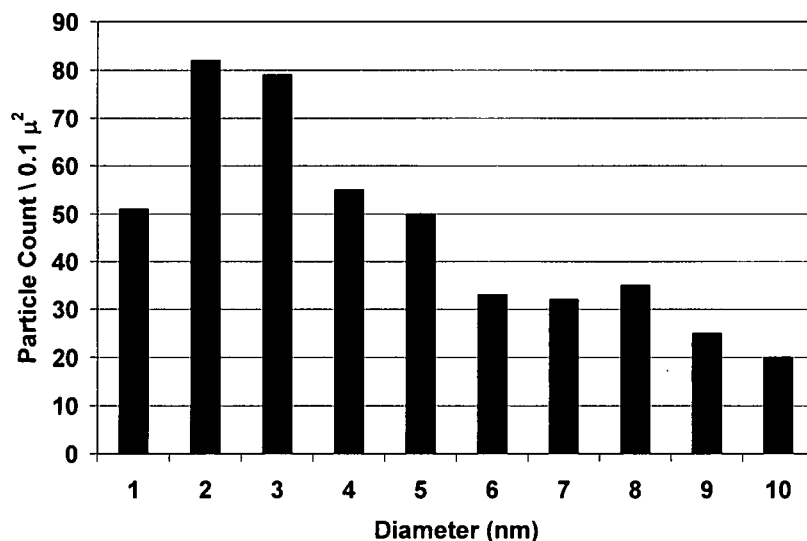


(b)

Figure 4.2. Size distribution of Pt nanoparticles from TTFA in (a) vacuum and (b) 5 Torr argon.

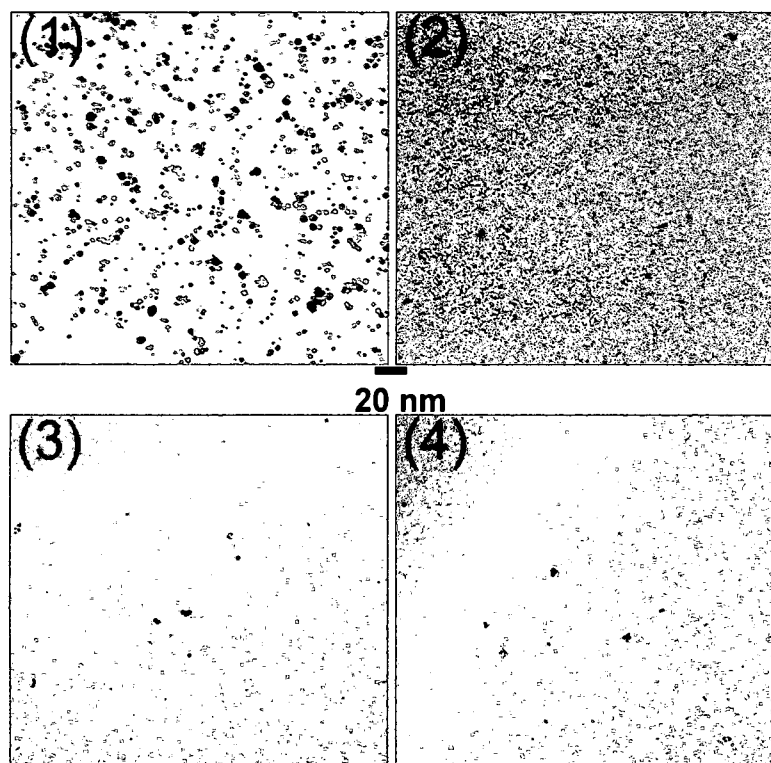


(a)

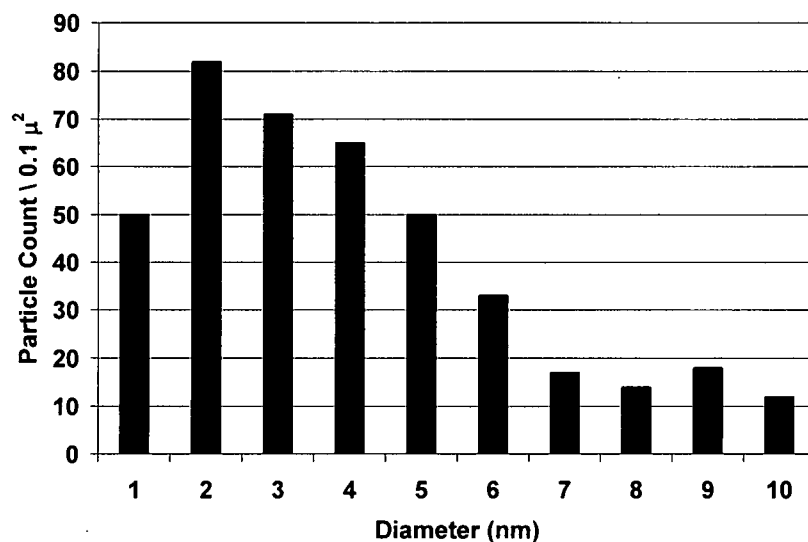


(b)

Figure 4.3. (a) Micrograph images (magn. 150k, $0.1 \mu\text{m}^2$) from matrix of samples using a 20 nm Pt TF TTFA target. The legend to identify the ablation parameters used is (1) 600 mJ/cm^2 -5 Torr Ar-4S-50 mm, (2) 500 mJ/cm^2 -5 Torr Ar-4S-75 mm, (3) 600 mJ/cm^2 -10 Torr Ar-1S-50 mm, and (4) 500 mJ/cm^2 -10 Torr Ar-1S-75 mm. (b) Size distribution of condition (1) "optimum ablation parameters".



(a)



(b)

Figure 4.4. (a) Micrograph images (magn. 150k, 0.1 μm^2) from matrix of samples using a 10 nm Pt TF TTFA target. The legend to identify the ablation parameters used is (1) 600 mJ/cm^2 -5 Torr Ar-4S-50 mm, (2) 500 mJ/cm^2 -5 Torr Ar-4S-75 mm, (3) 600 mJ/cm^2 -10 Torr Ar-1S-50 mm, and (4) 500 mJ/cm^2 -10 Torr Ar-1S-75 mm. (b) Size distribution of condition (1) "optimum ablation parameters".

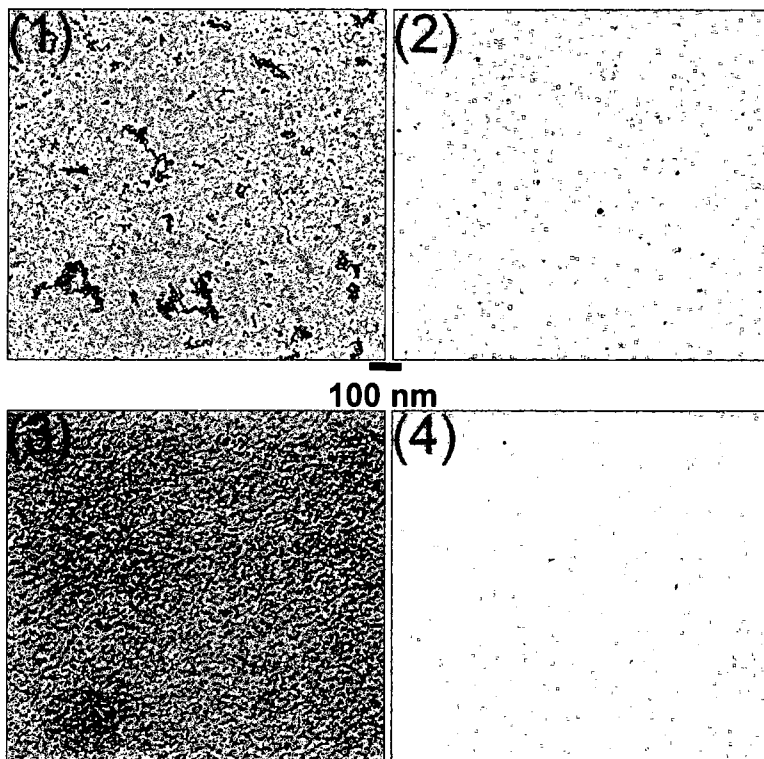
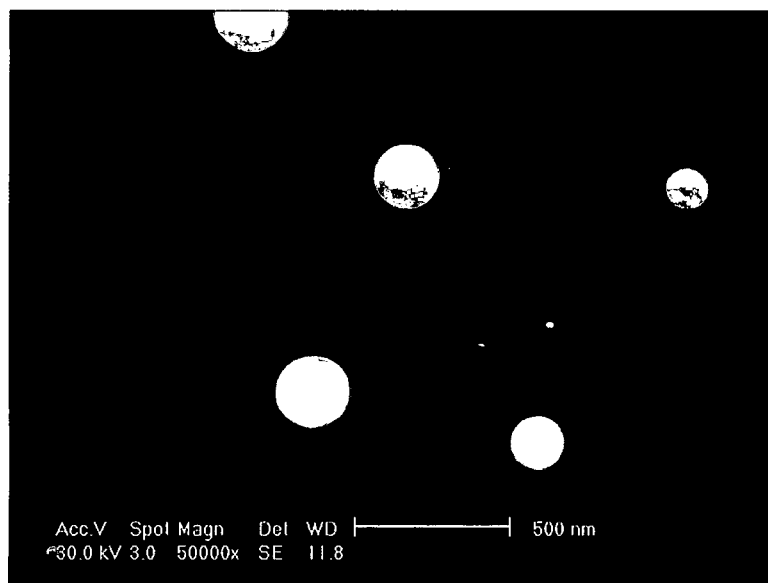
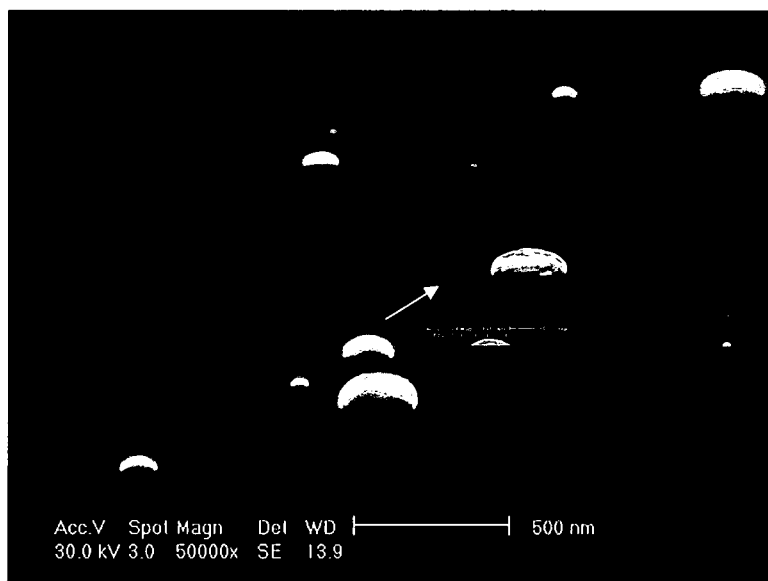


Figure 4.5. Micrograph images (magn. 30k, $3.0 \mu\text{m}^2$) from matrix of samples using a 5 nm Pt TF TTFA target. The legend to identify the ablation parameters used is (1) 600 mJ/cm^2 -5 Torr Ar-4S-50 mm, (2) 500 mJ/cm^2 -5 Torr Ar-4S-75 mm, (3) 600 mJ/cm^2 -10 Torr Ar-1S-50 mm, and (4) 500 mJ/cm^2 -10 Torr Ar-1S-75 mm.

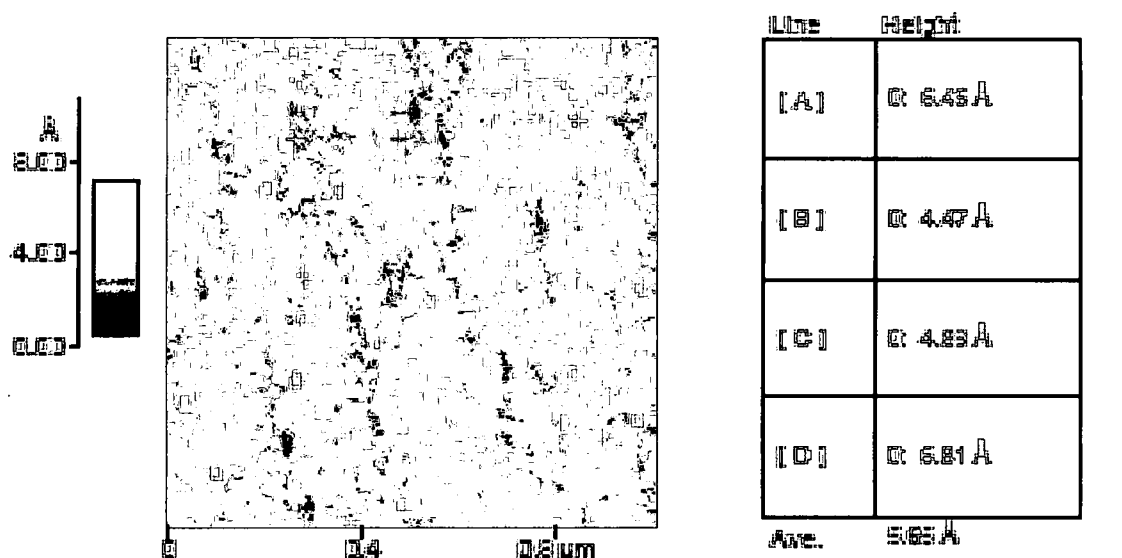


(a)

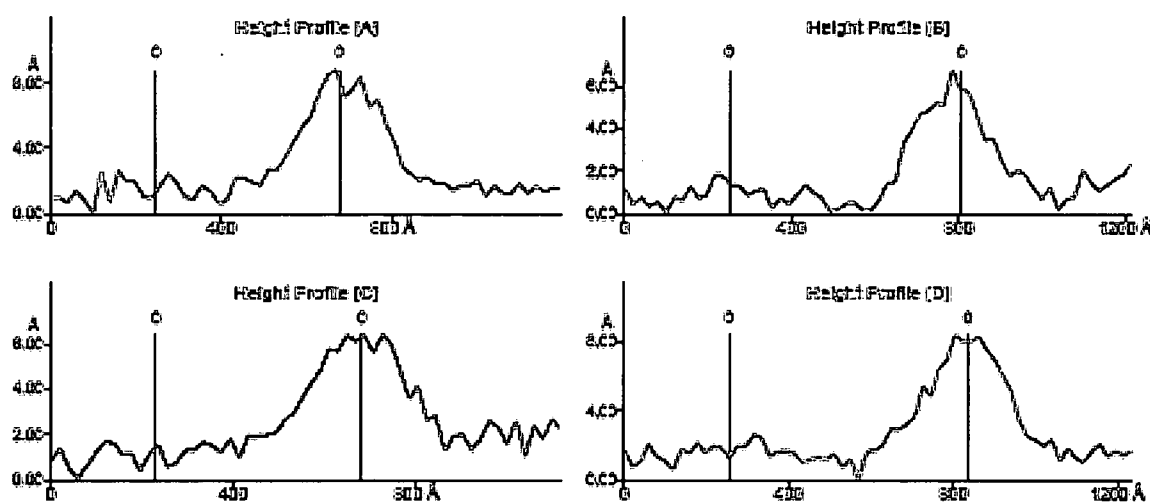


(b)

Figure 4.6. Scanning electron micrographs (SEM) of Pt nanoparticles deposited by TTFA on Si substrates. (a) Examination of particles orientated perpendicular to the electron beam suggests they are round. (b) Examination of particles when tilted suggests they are round but flat (pancake-like).



(a)



(b)

Figure 4.7. Platinum nanoparticle height determination. (a) Atomic force micrograph taken in non-contact mode shows numerous nanoparticles (bright contrast) that are approximately 0.6 nm tall. Particle heights are shown in the table and range 0.5 - 0.7 nm. (b) Line profiles across these particles suggest the nanoparticles are wider than they are tall (i.e. flat).

CHAPTER V

COMPOSITION OF NANOELECTRODES

Does God conduct opinion polls to determine truth?...If something is true about spiritual things, does that affect the nature of that truth?

-Robert S. McGee

Introduction

The study of interactions between silicon (Si) and transition metals (TM) and their use in silicon integrated circuits is at the forefront of developing new sensor technologies. Because of its natural abundance, processing ease, passivating quality, and electronic properties, silicon is the material of choice for most electronic devices making it the most important semiconducting material.

As early as the 1970's, transition-metal-silicon reaction couples have been investigated [1]. The properties of metal silicides directly related to device reliability are their thermal stability, low resistivity, electronic barrier formation, and reduced contact resistance [2]. In a paper on surface properties of platinum by Li et al., Pt electrode materials are stated to be more advantageous, and therefore, superior to gold (Au) electrode systems [3]. They attributed the

inferiority of Au electrode systems to their incompatibility with the Si class of integrated circuit technology because of the higher diffusivity and the deep electronic traps they form in Si. This fact coupled with the notion that Pt based silicides (Pt_xSi) are suitable candidates for the purpose of designing a low Schottky barrier contact material (ideally 0 eV) [2] suggests that Pt and subsequent silicide formation induced by thermal annealing on Si substrates offers great potential for application as nanoparticle electrodes.

Walser and Bene were the first to propose a rule for predicting which phase would nucleate first at the TM-Si interface [1]. Their prediction made use of the knowledge from phase diagrams of the binary compounds that could potentially form. They expected the first phase nucleated to be the congruent melting phase next to the lowest temperature eutectic. In other words, the reaction of a TM-Si bilayer would produce a planar TM-silicide at a temperature well below the melting point of the silicide phase [4]. For platinum silicide, the prediction of the phase indicated Pt_2Si formation. Walser and Bene corroborated this prediction experimentally for a thin film [1]. Following this initial prediction from 1976, Tsaur and his colleagues refined the prediction in 1981 to say the silicide system is driven toward equilibrium by forming compounds richer in the excess element [4]. Thus, the next phase of the compound formed would be richer in the unreacted element. Their experimental results pointed to PtSi and Pt_3Si as the next phases [4]. Additionally, the investigation by Larrieu et al. into the kinetics of platinum silicidation indicated the thermally activated reaction is a

two step process initiated by Pt diffusing into Si to form the Pt_2Si intermediate compound, followed by Si diffusing into Pt_2Si giving the stable PtSi layer [2]. One other thin film study demonstrated the platinum silicide forming sequence and reported forming energies for the Pt_2Si and PtSi phases as 28.8 kJ/mole and 33.0 kJ/mole, respectively [5].

It was anticipated, given the 113.7 kJ/mol (443.8 eV) available in a Pt nanoparticle during the TTFA process calculated in Chapter 4, that platinum silicide nanoparticles would be formed on the surface and possibly at the interface of the silicon substrate. Of interest was X-ray diffraction work performed by Tammeveski et al. which suggested that annealing temperatures greater than 300°C were necessary to observe a silicide phase diffraction pattern [6]. The use of higher annealing temperatures was reported to result in a platinum silicide at the interface [2,5,7]. Therefore, following Pt nanoparticle deposition onto Si substrates, half of the samples were annealed at 410°C (Table 4.1) to create a conductive and stable platinum silicide interface. An as-deposited diffusion reaction was expected since the results from Chapter 3 suggested the Pt nanoparticles in the plume were at liquid temperatures. Observation of diffusion in the Pt sample topography would suggest interaction with the semiconductor substrate. If a diffusion reaction is observed, then issues needing to be addressed are (1) the stoichiometry of the platinum silicide phase, (2) its size, and (3) the effects of temperature and (4) ablation parameters.

Experimental

As-deposited and post-annealed samples were characterized by X-ray diffraction (XRD) and X-ray photoelectron spectroscopy (XPS) to determine if the nanoparticle energy, prior to impact with the substrate, was sufficiently high to induce silicide formation in the absence of *ex-situ* annealing. X-ray diffraction characterization was performed with a PANalytical X'Pert Pro MRD in two-theta (2θ) mode with a programmable diffraction slit and a 0.18 degree parallel plate collimator with a (graphite) flat crystal monochromator. A Cu K-alpha ($K\alpha$) anode material was used with the generator voltage set to 45 kV and the tube current at 40 mA. The X-ray diffractometer was used to look for any long range order in the Pt nanoparticles (i.e. crystalline versus amorphous character) and for evidence of diffraction peaks at values of 2θ corresponding to a silicide phase, thereby indicating Pt diffusion. X-ray photoelectron spectroscopy (Physical Electronics PHI 5700 ESCA System equipped with a Model 20-327 Electron Gun) were used to look for evidence of platinum diffusion and stoichiometry. An aluminum (Al) monochromated anode material (1486.6 eV, 7 mm filament) was used with the voltage set at 15 kV. The pass energy and scan rate were adjusted to achieve the best signal to noise ratio.

Results and Discussion

Sample characterization was performed to look for evidence of Pt reaction with the substrate. X-ray diffraction results from as-deposited (no annealing)

TTFA Pt nanoparticles on Si substrates using the “optimum ablation parameters” compared with an as-deposited RF magnetron sputtered 10 nm Pt TF on Si are shown in Figure 5.1. The optimum ablation parameters identified in Chapter 4 consisted of using either a 10 nm or 20 nm TF Pt TTFA target positioned 50 mm from the substrate with a laser energy of 600 mJ at an argon pressure of 5 Torr for a duration of 4S laser pulses. The sputter deposited film was used as a reference standard, and four peaks were observed for it. These peaks were indicative of diffraction of X-rays at angles of 2θ indicative of the cubic phase of Pt. For the TTFA samples, compositional differences were noted by the presence of peaks at additional diffraction angles. These additional peaks were consistent with various silicide phases. The observation of platinum silicide is reasonable given a comparison of the enthalpies for forming different silicide phases ($\text{Pt}_2\text{Si} = 28.8 \text{ kJ/mol}$ and $\text{PtSi} = 33.0 \text{ kJ/mol}$) [5] with the total enthalpy for Pt during the TTFA (113.7 kJ/mol) process calculated in Chapter 4. These results demonstrated the Pt nanoparticles were energetic enough to induce a reaction of Pt with the substrate.

Using the Scherrer formula

$$t = 0.9\lambda/B\cos\theta_B, \quad (5.1)$$

where λ measured in Angstroms is 1.54 for Cu $K\alpha$ and B measured in radians at an intensity equal to half the maximum intensity for angles of θ , an estimated particle size was calculated for the particles. From the measured half width full maximum of the X-ray diffraction lines, Pt and Pt_xSi_y particle diameters for the

TTFA growth environments were approximated. Interestingly, the calculated crystal sizes were in good agreement with the original thicknesses of the Pt TF (10 nm) and TTFA target materials (10 nm and 20nm).

X-ray photoelectron spectroscopy was conducted to confirm XRD results and evaluate the effect of annealing the nano-Pt sample. Shown in Figures 5.2-5.9 are the X-ray photoelectron spectra for the Pt 4f signal (Figures 5.2-5.5) and Si 2p signal (Figures 5.6-5.9) at the TTFA Pt-Si substrate surface (Figures 5.2, 5.3, 5.6, and 5.7) and interface (Figures 5.4, 5.5, 5.8, and 5.9) as a function of ex-situ annealing at 410°C (Figure 5.3, 5.5, 5.7, and 5.9). In comparison to a sputter cleaned Pt foil which showed a Pt 4f_{7/2} peak at 71 eV (Figure 5.2), compositional differences were noted at the as-deposited nanoelectrode surface by the shift of the Pt 4f_{7/2} peak to higher binding energy. As shown in Figure 5.2, this shift from 71 eV to 72 eV was a significant shift and signified the surface Pt was not elemental but the Pt₂Si silicide phase. With annealing (Figure 5.3), this shift was greater than 72.5 eV and definitively indicated the Pt had diffused into the substrate to create a conductive platinum silicide interface that was, in chemical composition, the PtSi silicide phase. These XPS results were consistent with the various silicide phases identified in the XRD analyses and provided corroborating evidence for the energetics of the plume. While annealing contributed to a more homogenous silicide at the surface (Figure 5.3), what was shown in Figures 5.3 and 5.4 was that the Pt diffusion observed at the interface was the result of thermal energy conversion and momentum transfer of

the molten Pt on Si created during the TTFA process (Figure 5.3) and not the annealing process (Figure 5.4). These results indicated that the added step of annealing was not necessary to form a conductive platinum silicide and that the TTFA process itself was sufficient to induce a reaction.

Another interesting feature of the nano-Pt samples was the presence of Si surface oxidation (Figures 5.6 and 5.7). In addition to the elemental Si 2p peak between 99-100 eV, an oxidized Si 2p peak was present at 104 eV. In comparison, an oxidized silicide was not present at the as-deposited or annealed silicide interface (Figures 5.8 and 5.9, respectively). Thus, while annealing may have slightly increased the surface oxidation, annealing was not necessary to produce Pt silicide particles to be used as nanoelectrodes.

Summary

Platinum reaction with the silicon substrate created a platinum silicide interface. *Ex-situ* annealing was not necessary to induce Pt diffusion since the plume was sufficiently hot to cause a reaction. Surface oxidation of the Si substrate was observed.

References

- [1] R. M. Walser, R. W. Bene, "First Phase Nucleation in Silicon-Transition-Metal Planar Interfaces," *Appl. Phys. Lett.*, 28 (1976) 624.
- [2] G. Larrieu, E. Dubois, X. Wallart, X. Baie, "Formation of Platinum-Based Silicide Contacts: Kinetics, Stoichiometry, and Current Drive Capabilities," *J. Appl. Phys.*, 94 (2003) 7801.
- [3] Z. Li, P. Beck, D. A. A. Ohlberg, D. R. Stewart, R. S. Williams, "Surface Properties of Platinum Thin Films as a Function of Plasma Treatment Conditions," *Surf. Sci.*, 529 (2003) 410.
- [4] B. Y. Tsaur, S. S. Lau, J. W. Mayer, M. A. Nicolet, "Sequence of Phase Formation in Planar Metal-Si Reaction Couples," *Appl. Phys. Lett.*, 38 (1981) 922.
- [5] J. Yin, W. Cai, Y. Zheng, L. Zhao, "Effect of Pt Film Thickness on PtSi Formation and Film Surface Morphology," *Surf. Coat. Technol.*, 198 (2005) 329.
- [6] K. Tammeveski, T. Tenno, J. Niinisto, T. Leitner, G. Friedbacher, L. Niinisto, "Thermal Preparation of Thin Platinum Coatings and Their Electrochemical and Atomic Force Microscopic Characterization," *Appl. Surf. Sci.*, 156 (2000) 135.
- [7] F. F. Fan, R. G. Keil, A. J. Bard, "Semiconductor Electrodes. 48. Photooxidation of Halides and Water on n-Silicon Protected with Silicide Layers," *J. Am. Chem. Soc.*, 105 (1983) 220.

Figures

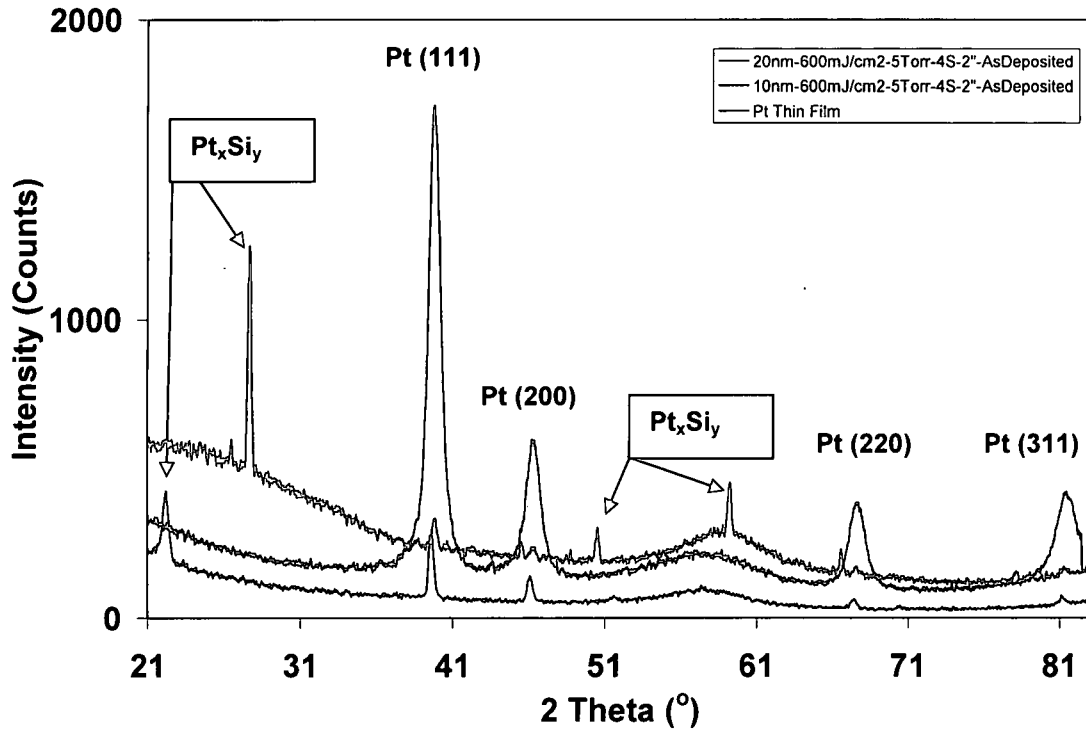


Figure 5.1. X-ray diffraction spectra of a collection of Pt nanoparticles deposited on Si by TTFA using the "optimum ablation parameters" compared with a RF magnetron sputtered 10 nm Pt TF. Diffraction of X-rays was observed in all cases at angles of 2θ indicative of Pt. For the TTFA samples, compositional differences were noted by the presence of peaks at additional diffraction angles. These additional peaks were consistent with various silicide phases.

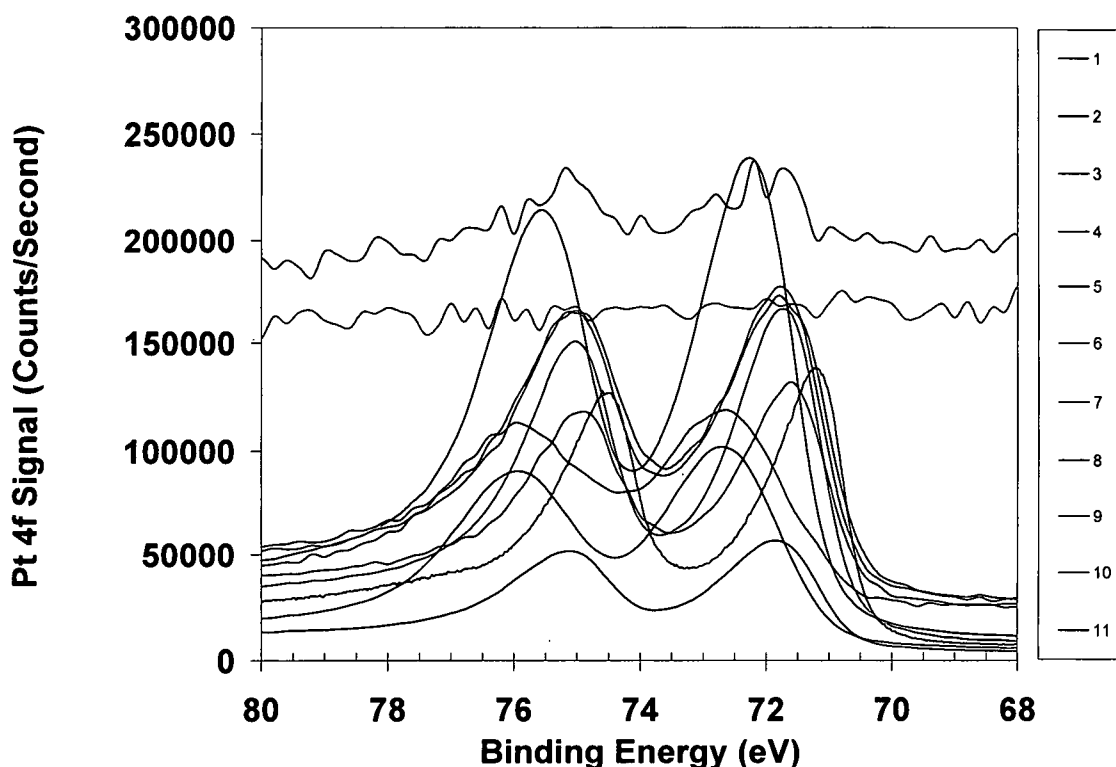


Figure 5.2. X-ray photoelectron spectroscopy of the Pt 4f peak at the surface of the test matrix of samples. The collection of spectra are from as-deposited (unannealed) samples. Curves 1-11 are for test matrix samples as follows: (1) Pt foil-unannealed, (2) 20 nm-600 mJ/cm²-vacuum-1S-50 mm, (3) 20 nm-600 mJ/cm²-5 Torr Ar-4S-50 mm, (4) 20 nm-600 mJ/cm²-10 Torr Ar-4S-75 mm, (5) 20 nm-500 mJ/cm²-5 Torr Ar-1S-50 mm, (6) 20 nm-500 mJ/cm²-10 Torr Ar-1S-75 mm, (7) 10nm-600 mJ/cm²-vacuum-1S-50 mm, (8) 10 nm-600 mJ/cm²-5 Torr Ar-1S-75 mm, (9) 10 nm-600 mJ/cm²-10 Torr Ar-1S-50 mm, (10) 10 nm-500 mJ/cm²-5 Torr Ar-4S-75 mm, and (11) 10 nm-500 mJ/cm²-10 Torr Ar-4S-50 mm.

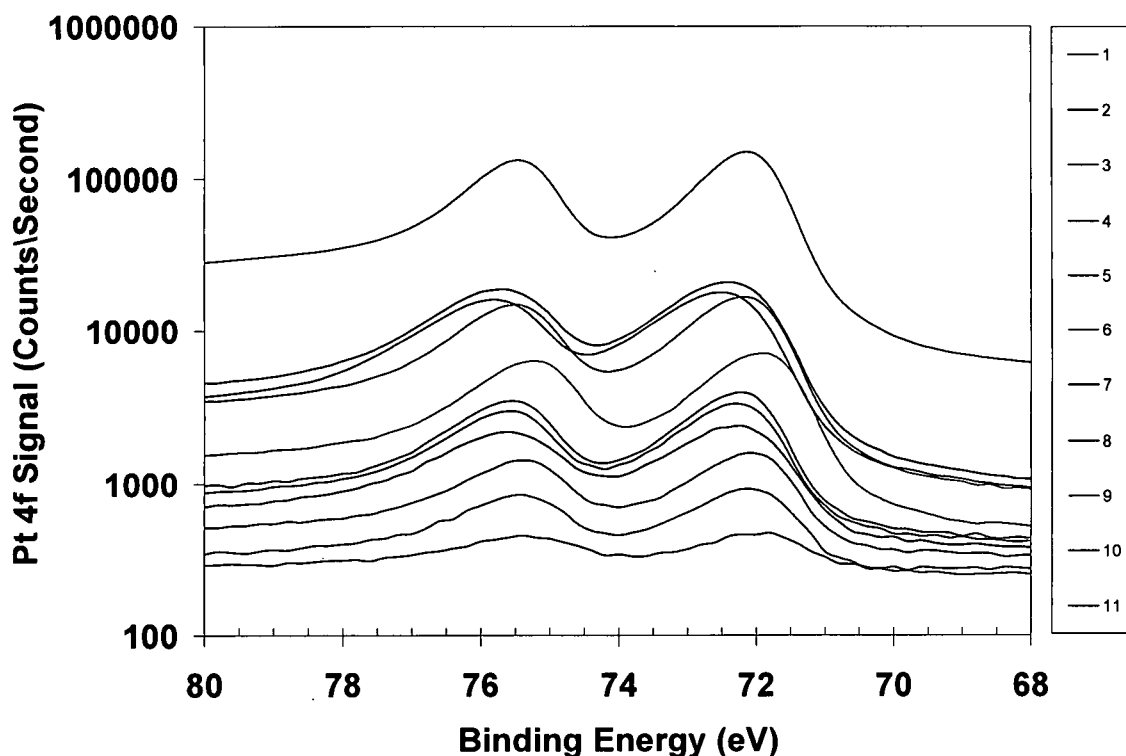


Figure 5.3. X-ray photoelectron spectroscopy of the Pt 4f peak at the surface of the test matrix of samples. The collection of spectra are from samples annealed at 410°C. Curves 1-11 are for test matrix samples as follows: (1) Pt foil-annealed, (2) 20 nm-600 mJ/cm²-vacuum-1S-50 mm, (3) 20 nm-600 mJ/cm²-5 Torr Ar-1S-75 mm, (4) 20 nm-600 mJ/cm²-10 Torr Ar-1S-50 mm, (5) 20 nm-500 mJ/cm²-5 Torr Ar-4S-75 mm, (6) 20 nm-500 mJ/cm²-10 Torr Ar-4S-50 mm, (7) 10 nm-600 mJ/cm²-vacuum-1S-50 mm, (8) 10 nm-600 mJ/cm²-5 Torr Ar-4S-50 mm, (9) 10 nm-600 mJ/cm²-10 Torr Ar-4S-75 mm, (10) 10 nm-500 mJ/cm²-5 Torr Ar-1S-50 mm, and (11) 10 nm-500 mJ/cm²-10 Torr Ar-1S-75 mm.

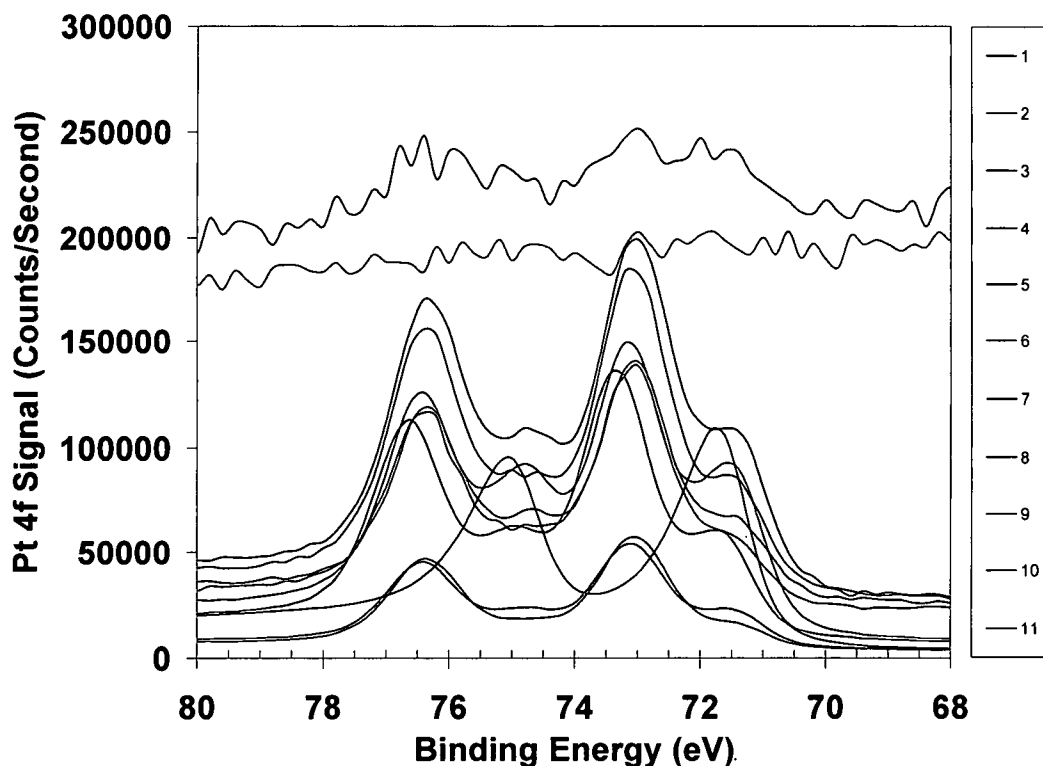


Figure 5.4. X-ray photoelectron spectroscopy of the Pt 4f peak at the interface of the test matrix of samples. The collection of spectra are from as-deposited (unannealed) samples. Curves 1-11 are for test matrix samples as follows: (1) Pt foil-unannealed, (2) 20 nm-600 mJ/cm²-vacuum-1S-50 mm, (3) 20 nm-600 mJ/cm²-5 Torr Ar-4S-50 mm, (4) 20 nm-600 mJ/cm²-10 Torr Ar-4S-75 mm, (5) 20 nm-500 mJ/cm²-5 Torr Ar-1S-50 mm, (6) 20 nm-500 mJ/cm²-10 Torr Ar-1S-75 mm, (7) 10 nm-600 mJ/cm²-vacuum-1S-50 mm, (8) 10 nm-600 mJ/cm²-5 Torr Ar-1S-75 mm, (9) 10 nm-600 mJ/cm²-10 Torr Ar-1S-50 mm, (10) 10 nm-500 mJ/cm²-5 Torr Ar-4S-75 mm, and (11) 10 nm-500 mJ/cm²-10 Torr Ar-4S-50 mm.

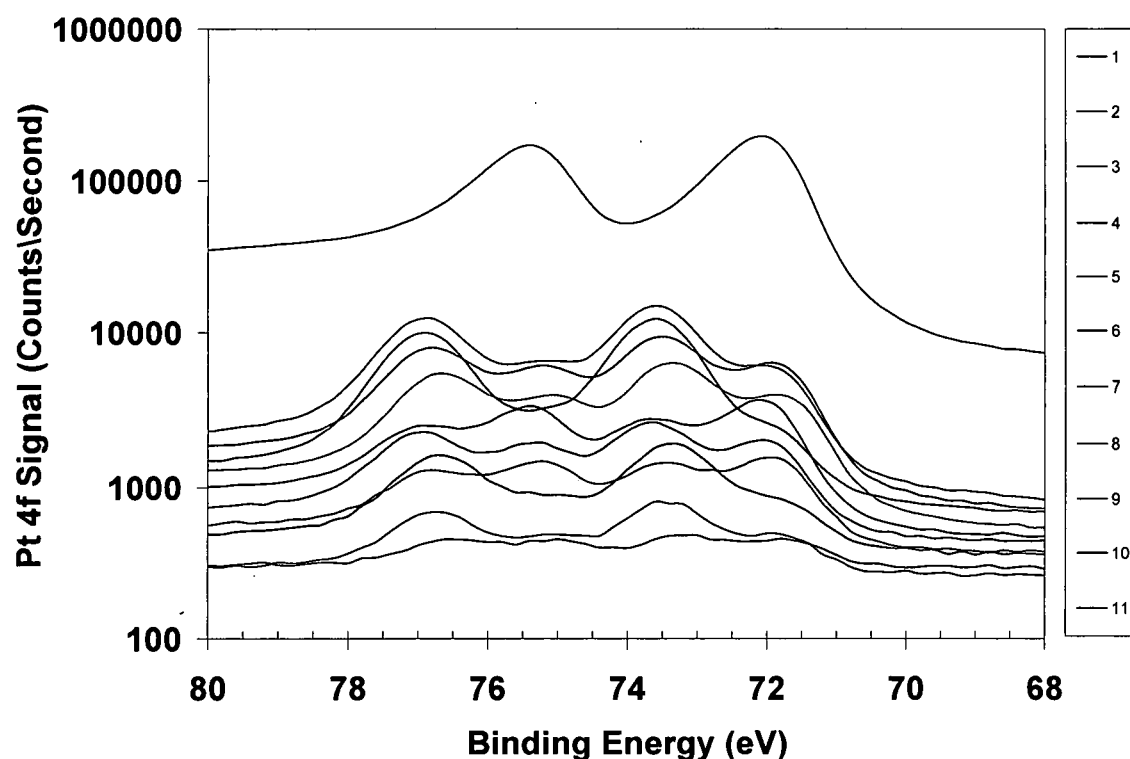


Figure 5.5. X-ray photoelectron spectroscopy of the Pt 4f peak at the interface of the test matrix of samples. The collection of spectra are from samples annealed at 410°C. Curves 1-11 are for test matrix samples as follows: (1) Pt foil-annealed, (2) 20 nm-600 mJ/cm²-vacuum-1S-50 mm, (3) 20 nm-600 mJ/cm²-5 Torr Ar-1S-75 mm, (4) 20 nm-600 mJ/cm²-10 Torr Ar-1S-50 mm, (5) 20 nm-500 mJ/cm²-5 Torr Ar-4S-75 mm, (6) 20 nm-500 mJ/cm²-10 Torr Ar-4S-50 mm, (7) 10 nm-600 mJ/cm²-vacuum-1S-50 mm, (8) 10 nm-600 mJ/cm²-5 Torr Ar-4S-50 mm, (9) 10 nm-600 mJ/cm²-10 Torr Ar-4S-75 mm, (10) 10 nm-500 mJ/cm²-5 Torr Ar-1S-50 mm, and (11) 10 nm-500 mJ/cm²-10 Torr Ar-1S-75 mm.

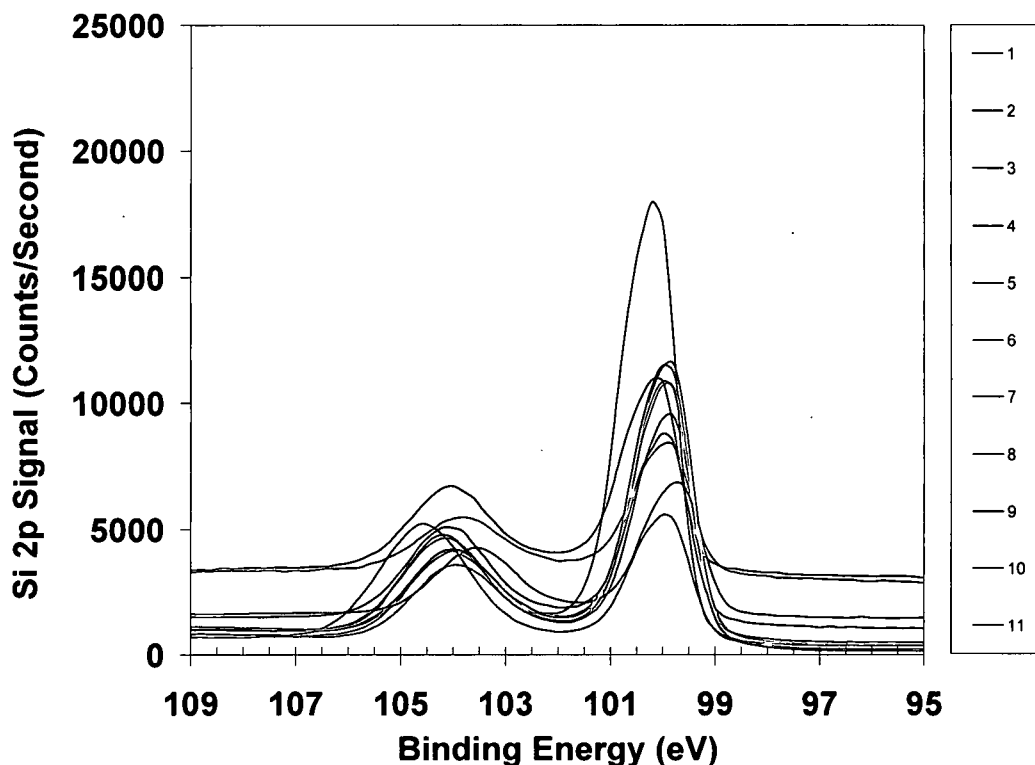


Figure 5.6. X-ray photoelectron spectroscopy of the Si 2p peak at the surface of the test matrix of samples. The collection of spectra are from as-deposited (unannealed) samples. Curves 1-11 are for test matrix samples as follows: (1) Si substrate-unannealed, (2) 20 nm-600 mJ/cm²-vacuum-1S-50 mm, (3) 20 nm-600 mJ/cm²-5 Torr Ar-4S-50 mm, (4) 20 nm-600 mJ/cm²-10 Torr Ar-4S-75 mm, (5) 20 nm-500 mJ/cm²-5 Torr Ar-1S-50 mm, (6) 20 nm-500 mJ/cm²-10 Torr Ar-1S-75 mm, (7) 10 nm-600 mJ/cm²-vacuum-1S-50 mm, (8) 10 nm-600 mJ/cm²-5 Torr Ar-1S-75 mm, (9) 10 nm-600 mJ/cm²-10 Torr Ar-1S-50 mm, (10) 10 nm-500 mJ/cm²-5 Torr Ar-4S-75 mm, and (11) 10 nm-500 mJ/cm²-10 Torr Ar-4S-50 mm.

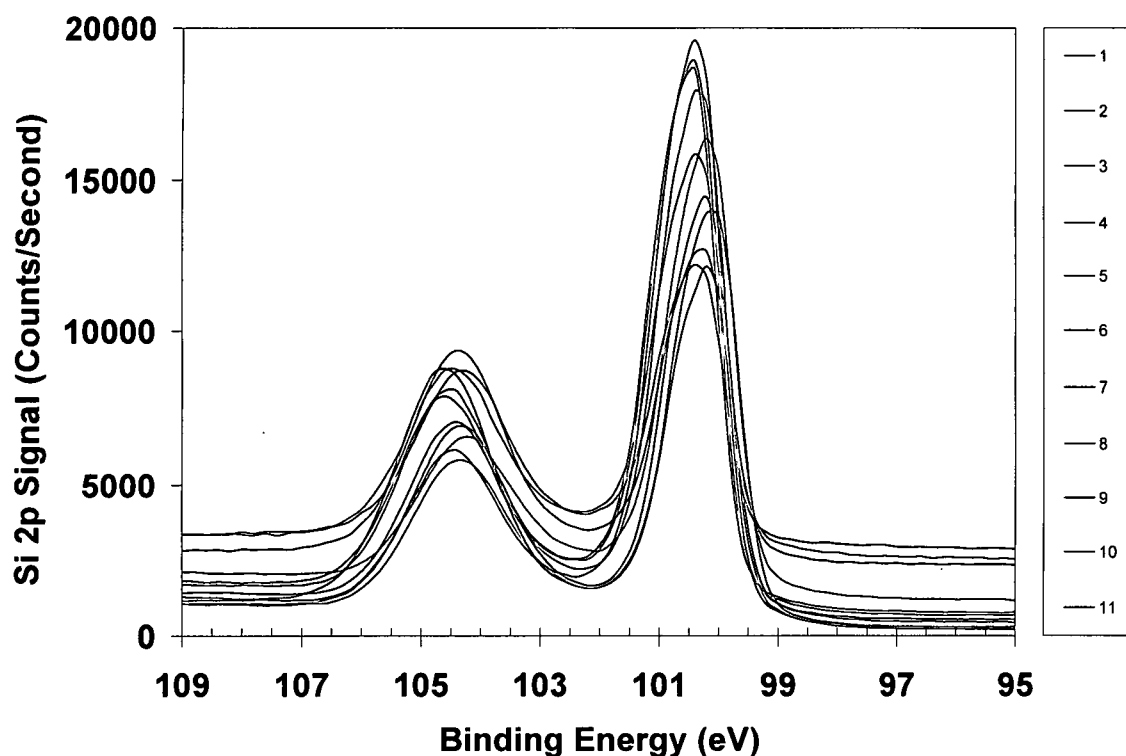


Figure 5.7. X-ray photoelectron spectroscopy of the Si 2p peak at the surface of the test matrix of samples. The collection of spectra are from samples annealed at 410°C. Curves 1-11 are for test matrix samples as follows: (1) Si substrate-annealed, (2) 20 nm-600 mJ/cm²-vacuum-1S-50 mm, (3) 20 nm-600 mJ/cm²-5 Torr Ar-1S-75 mm, (4) 20 nm-600 mJ/cm²-10 Torr Ar-1S-50 mm, (5) 20 nm-500 mJ/cm²-5 Torr Ar-4S-75 mm, (6) 20 nm-500 mJ/cm²-10 Torr Ar-4S-50 mm, (7) 10 nm-600 mJ/cm²-vacuum-1S-50 mm, (8) 10 nm-600 mJ/cm²-5 Torr Ar-4S-50 mm, (9) 10 nm-600 mJ/cm²-10 Torr Ar-4S-75 mm, (10) 10 nm-500 mJ/cm²-5 Torr Ar-1S-50 mm, and (11) 10 nm-500 mJ/cm²-10 Torr Ar-1S-75 mm.

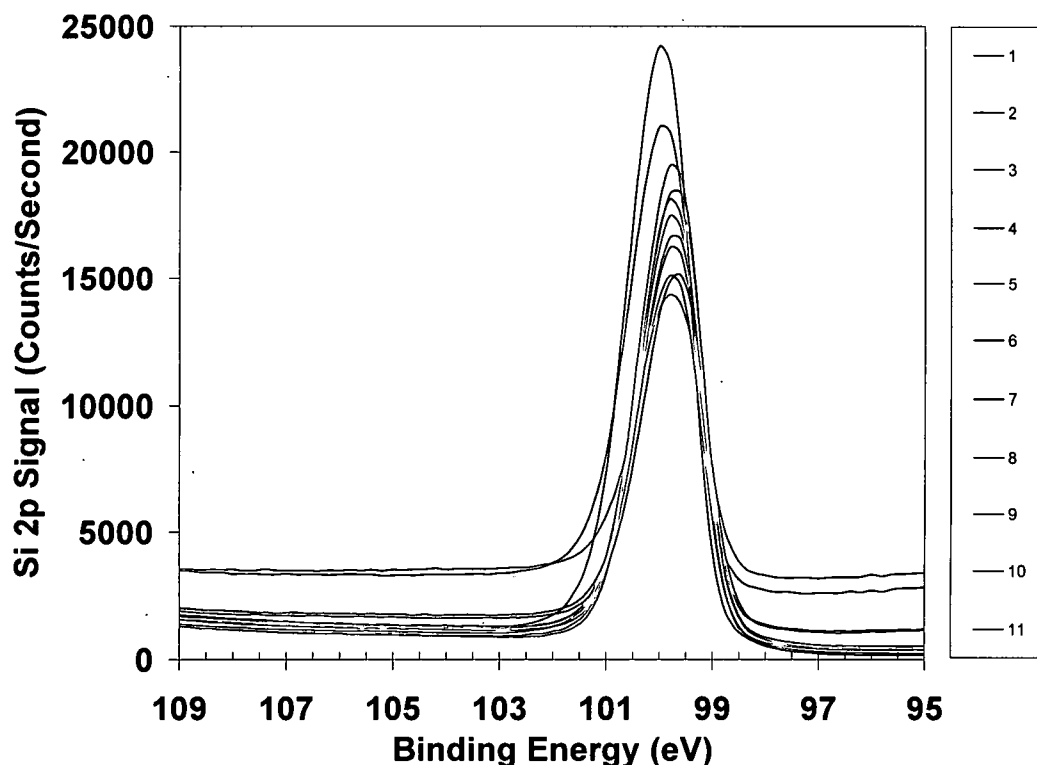


Figure 5.8. X-ray photoelectron spectroscopy of the Si 2p peak at the interface of the test matrix of samples. The collection of spectra are from as-deposited (unannealed) samples. Curves 1-11 are for test matrix samples as follows: (1) Si substrate-unannealed, (2) 20 nm-600 mJ/cm²-vacuum-1S-50 mm, (3) 20 nm-600 mJ/cm²-5 Torr Ar-4S-50 mm, (4) 20 nm-600 mJ/cm²-10 Torr Ar-4S-75 mm, (5) 20 nm-500 mJ/cm²-5 Torr Ar-1S-50 mm, (6) 20 nm-500 mJ/cm²-10 Torr Ar-1S-75 mm, (7) 10 nm-600 mJ/cm²-vacuum-1S-50 mm, (8) 10 nm-600 mJ/cm²-5 Torr Ar-1S-75 mm, (9) 10 nm-600 mJ/cm²-10 Torr Ar-1S-50 mm, (10) 10 nm-500 mJ/cm²-5 Torr Ar-4S-75 mm, and (11) 10 nm-500 mJ/cm²-10 Torr Ar-4S-50 mm.

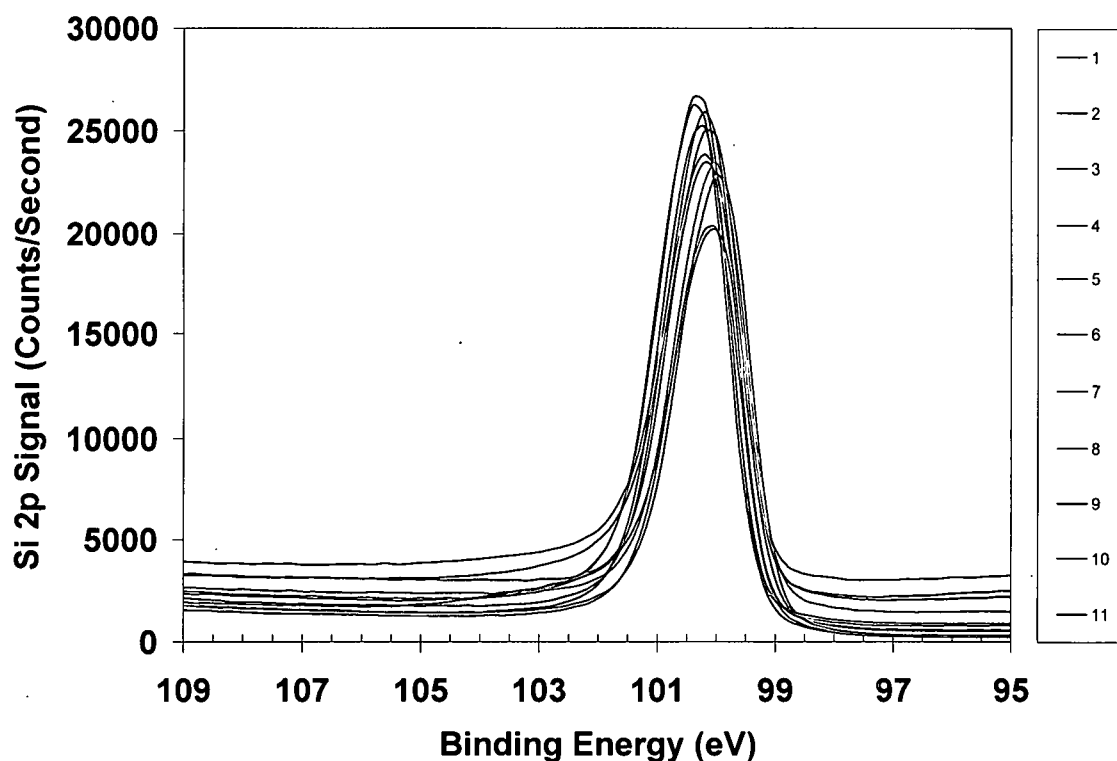


Figure 5.9. X-ray photoelectron spectroscopy of the Si 2p peak at the interface of the test matrix of samples. The collection of spectra are from samples annealed at 410°C. Curves 1-11 are for test matrix samples as follows: (1) Si substrate-annealed, (2) 20 nm-600 mJ/cm²-vacuum-1S-50 mm, (3) 20 nm-600 mJ/cm²-5 Torr Ar-1S-75 mm, (4) 20 nm-600 mJ/cm²-10 Torr Ar-1S-50 mm, (5) 20 nm-500 mJ/cm²-5 Torr Ar-4S-75 mm, (6) 20 nm-500 mJ/cm²-10 Torr Ar-4S-50 mm, (7) 10 nm-600 mJ/cm²-vacuum-1S-50 mm, (8) 10 nm-600 mJ/cm²-5 Torr Ar-4S-50 mm, (9) 10 nm-600 mJ/cm²-10 Torr Ar-4S-75 mm, (10) 10 nm-500 mJ/cm²-5 Torr Ar-1S-50 mm, and (11) 10 nm-500 mJ/cm²-10 Torr Ar-1S-75 mm.

CHAPTER VI

NANOELECTRODE ELECTROCHEMISTRY

Happiness is equilibrium. Shift your weight. Equilibrium is pragmatic. You have to get everything into proportion. You compensate, rebalance yourself so that you maintain your angle to the world. When the world shifts, you shift.
-Tom Stoppard

Introduction

Study of the oxidation-reduction processes occurring at the nanoelectrode array/solution interface is of fundamental interest in electrochemistry. The electrochemical behavior of the TTFA synthesized nanometer-scaled electrodes is hypothesized to depend upon electrode size, separation distance, and topography. It is possible that a reduction in electrode diameter and the gap between adjacent electrodes by optimizing particle population density and morphology on the substrate surface may mitigate the limited electron transfer current observed when the electrode size is reduced. This current limitation occurs when a redox couple such as $\text{Fe}(\text{CN})_6^{4-}/\text{Fe}(\text{CN})_6^{3-}$ interacts less frequently with the surface of the electrodes, for example, because the electrodes are too small or well separated.

Experimental

Electrochemical measurements made on Pt and Pt_xSi_y nanoelectrode array (the nano-Pt particles deposited on Si wafer substrate) consisted of cyclic voltammetry, limiting current, and impedance. Direct and alternating current investigations were carried out using a Princeton Applied Research (PAR) potentiostat/galvanostat (Model 2273) controlled by Powersuite software. ZSimpWin equivalent electrode circuit (EEC) software was used to obtain information regarding the various voltage dependent circuit parameters acquired during the electrochemical impedance spectroscopy (EIS) analyses and to model the impedance behavior observed at the nanoelectrode surface. Cyclic voltammograms were obtained typically at a sweep rate of 50 mV/s. Amperometric measurements were made by stepping the potential below that necessary to reduce ferricyanide and monitoring the current decay with time as the electroactive species near the nanoelectrodes surface was consumed. The impedance parameters were as follows: 0.01 to 100000 Hz and 10 mV potential amplitude relative to the open circuit potential.

All solution based electrochemical experiments were carried out in a Faraday cage and involved the nanoelectrode array as the working electrode (WE). Numerous sample arrays were prepared via TTFA according to the test matrix identified in Table 4.1. The counter electrode was a platinized niobium mesh screen. A silver/silver chloride (Ag/AgCl) reference electrode (RE) filled with saturated potassium chloride (KCl) solution was used. This three electrode

setup was housed in an electrochemical flat cell having a geometric exposure area of 0.785 cm^2 and containing 300 mL of electrolyte. All nanoelectrode arrays were oxidized in 1.0 M sulfuric acid prior to degassing the liquid test solution with argon. Passivation of the remaining silicon surface to form SiO_2 isolated the silicon substrate, leaving the nanoelectrode array exposed to the liquid test solution for electrochemical characterization. The active area of the nanoelectrode array was determined from a modified form of the Cottrell equation and the measured limiting current obtained via chronoamperometry.

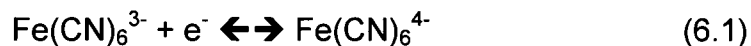
Liquid solutions were chosen on the basis of whether or not they were an oxidation reduction system (i.e. KCl supporting electrolyte plus potassium ferricyanide ($\text{K}_3\text{Fe}(\text{CN})_6$) or an environmental simulant (i.e. propylene carbonate which is a good chemical warfare simulant [1] and sodium chloride which is conductive and representative of a corrosive or even physiological environment). Redox couples were advantageous to determine the ability of the Pt nanoelectrode array to sustain electron transfer and operate as an electrochemical sensor. The chemical warfare simulant was chosen based on properties (i.e. vapor pressure, heat of vaporization, surface tension, and solubility) which mimic an actual blister agent [1]. The polarity of a solvent dramatically affects the charge density at the interface between the solution and the sensor; that is, $V = q/C$. It is possible that changes in the measured voltages will be observed at the Pt nanoelectrode array surface based on the polarity of the chosen simulant and the assumption of small capacitances being developed

at the array. Observation of voltage changes at the nanoelectrode surface demonstrates the viability of the Pt nanoelectrode array to selectively function as a chemical or biological sensor with improved sensitivity.

Results and Discussion

The foundation work first considered by Randles [2] and Sivicik [3], and the later numerical work of Nicholson and Shain [4], showed the fundamental relationship between current, concentration, diffusion coefficient and sweep rate. For large working electrodes, the CV experiment requires diffusion transport of the electroactive species. With decreasing electrode size, transport by diffusion does not need to occur and the resulting current does not result in a depletion zone at the electrode. A sigmoidal CV curve is obtained.

Size-dependent electrochemical properties were found at the solution-Pt nanoelectrode array interface. The cyclic voltammograms shown in Figures 6.1-6.3 were taken of oxidized Pt samples exposed to a degassed mixture of 0.5 M KCl + 0.001 M K₃Fe(CN)₆ (1:1 mixture ratio), which was used as the oxidation-reduction reaction model having a diffusion coefficient, D, equal to 0.770 x 10⁻⁵ cm²/s. In this model, the oxidation-reduction reaction occurs as described in equation (6.1).



Oxidation of the silicon surface in areas devoid of platinum nanoparticles provided a more catalytic surface for redox reactions to occur. Oxidation of the

silicon was achieved by holding the working electrode (actual sample) at a fixed potential of 1.2 V for 30 min prior to further electrochemical characterization. The sigmoidal shape of the CV curves obtained for the TTFA samples grown in vacuum (Figure 6.1a) and 5 Torr argon (Figures 6.2 and 6.3) shows the surfaces of each sample are comprised of numerous nanoelectrodes acting independently, i.e. sufficiently separated in a "nanoarray" (compare Figures 6.1a, 6.2, and 6.3 with Figure 6.1b).

It is also important to note the larger measured current for the vacuum growth sample as compared to the conventional Pt electrode. This larger current suggests the total electrode active area for the TTFA vacuum nanoarray is greater than the conventional electrode. The decreased measured current for the nanoarray grown in argon as compared to vacuum suggests not only the total active area of material is less but also the transport effects due to diffusion are small. Annealing the Pt nanoelectrodes at 410°C created a conductive, homogeneous PtSi nanoarray resulting in a slightly enhanced sigmoidal shaped CV curve (Figure 6.2). This result suggests that although annealing may not be necessary to produce a silicide or oxidize the substrate, it does enhance the already improved electron transfer observed for the as-deposited nanoparticles by creating a more catalytic array of nanoelectrodes, by virtue of a smaller diameter.

What this means is that the radii of the Pt nanoelectrodes, which according to AFM measurements are deposited essentially flush in an insulating

plane, are small enough and sufficiently separated from each other to be independent electrodes operating collectively in an array. This explanation is the analogy setup by White and White for oxidation-reduction reactions occurring at nanometer-scaled electrodes separated by nanoscale gaps [5]. The evolution of a diffusion field at a nanoelectrode array based on their simulations indicates that the diffusion layer (δ) is thinner than active site size or diameter, d and indicates that if $\delta < d$, then each active electrode has an individual diffusion field. A small d suggests the current is mass transfer limited and nanoelectrodes operate independently.

Using the same solution as in the CV measurement, the active area (A_A) of the nanoelectrode array was calculated following measurement of the chronoamperometric limiting current. The data shown in Figure 6.4 is for Pt nanoarrays grown at optimum ablation parameters using two different target thicknesses. The measured limiting current for the reduction of ferricyanide was used in the equation

$$i_d = nFA_A C k^0, \quad (6.2)$$

where C is the bulk concentration ($0.001 \text{ mol cm}^{-3}$) and k^0 the standard rate constant (0.024 cm s^{-1}) for ferricyanide at a nanoelectrode [6], to estimate the A_A of the electrodes. The Cottrell equation

$$i_d = nFA_A D^{1/2} C \pi^{-1/2} t^{-1/2} \quad (6.3)$$

was not used because transport was not diffusion controlled in this instance.

These values are presented in Table 6.1. For both growth environments, the

nanoarray A_A was less than the geometric area (A_G) of the flat cell ($A_G = 0.785 \text{ cm}^2$). The A_A of the conventional electrode calculated using the Cottrell equation was 3.518 mm^2 and was greater than its geometric area of 3.140 mm^2 . This 12.0% increase in area was attributed to surface roughness. Thus, the calculated A_A for the nanoarrays are in agreement with the measured currents indicated in the sigmoidal shape CV curves. Also, the larger A_A measured for the vacuum deposited Pt nanoarray may be due to the presence of multiple species of Pt as discussed in Chapters 3 and 4, where atomic Pt was shown to be deposited in addition to Pt NP.

Of particular interest was the comparison of the number of particles present per cm^2 on the sample with the number of those particles that were actually functioning as a nanoelectrode and how far apart they were. In Chapter 3 it was calculated that 2.4×10^{14} Pt particles were ablated per laser pulse of which in Chapter 4 it was determined by microscopy that only 5.0×10^{11} Pt particles/ cm^2 were deposited onto the substrate using optimum ablation parameters. For the same parameters, it was determined electrochemically that only 1.1×10^7 Pt particles/ cm^2 were active. This data meant that even though microscopic evidence demonstrated the particles were nonagglomerated, electrochemical evidence suggested some of the particles were close enough in proximity to their nearest neighbor that they performed as one larger electrode instead of as separate entities thereby reducing the total particle count.

However, if a uniform distribution of nanoelectrodes averaging 3 nm in diameter (d) is assumed, the total area of substrate covered with electrodes and the average gap or distance between the electrodes could be calculated. If the average nanoelectrode radius (r) is 1.5 nm, then the area (A) is equal to πr^2 or 7.1 nm^2 . The area correlates to $7.1 \times 10^{-14} \text{ cm}^2$ of particles. Multiplying this value by $5.0 \times 10^{11} \text{ Pt particles/cm}^2$ determined microscopically represented a total area of coverage of 3.6%. By taking the inverse square root of $5.0 \times 10^{11} \text{ Pt particles/cm}^2$, the average distance between nanoelectrodes was calculated to be 14 nm. Based on the average diameter of two concentric spherical yet planar nanoelectrodes separated by an average nanogap of 14 nm, it is hypothesized that this gap may be too close in some instances for the electrodes to be functioning independently of each other. Appendix C presents tabular and graphical representations of the TTFA efficiency and substrate percent coverage analyses in more detail. As shown in Table C.1 and Figure C.1, the TTFA method is an efficient means to generate small platinum nanoparticles, with an increase in the nanoelectrode radius implying a greater percentage of substrate is covered with platinum (Table C.2 and Figure C.2).

Electrochemical impedance spectroscopy data for Pt nanoarrays grown at optimum ablation parameters for two different target thicknesses are shown in Figure 6.5. Impedance results from the opposition to the flow of electrons, which is analogous to an alternating current circuit. The diameter of the semicircle obtained is proportional to electrode resistance. A smaller diameter represents a

decrease in electrode resistance which corresponds to an increase in the active area for faradaic charge-transfer reactions [7]. In other words, electron transfer is easier for small resistances, which is what is observed for the nanoarrays in the high frequency regime thus corroborating the earlier direct current (DC) electrochemical data. Additionally, the nanoarrays do not show diffusion effects from Warburg elements in the impedance spectra. These results indicate the effects due to diffusion are small for the nanoarrays and provide additional evidence of an ensemble of particles, sufficiently small and separate from each other that there is no depletion of the redox couple at the electrode surface.

Further evaluation of impedance data gathered from the Pt nanoarrays in a variety of electrolytes supports their utility for electrochemical sensing. The resultant Nyquist plots of the TTFA fabricated Pt nanoarrays (Figure 6.6) in the presence of propylene carbonate (neat) and sodium chloride (5.0 %) demonstrate that the Pt nanoarrays are sensitive in the high and low frequency regimes to changes in solvent polarity and electrolyte conductivity. These data demonstrate the utility of the Pt nanoarrays as a chemical or biological nanosensor (results for 0.9% sodium chloride not shown) because measurements can be made in the absence of conductive electrolytes. By exploiting the changes induced by an analyte-nanostructure interaction as shown by the decreased resistance with a change in electrolyte conductivity, it is anticipated that analyte signatures may be quantified with these nanoarrays by electrochemical response characteristics. Additionally, the ability to optimize the

population density of the nanoelectrodes in the nanoarray contributes to an increased response time at the surface of each nanoelectrode, and ultimately, maximizes the electrochemical sensitivity.

Lastly, equivalent circuit modeling of the impedance data revealed multiple RC circuits. The most suitable equivalent circuits to explain the data are shown in Figure 6.7. The fact that there are two RC circuits rules out a conventional Randles circuit model (Figure 6.7a) which contains only one RC component. Because there are two RC circuits observed in the data, either Figure 6.7b (RC components in series) or Figure 6.7c (RC components in parallel) are the equivalent circuit models that fit this data. Based on current literature discussing nanogaps [5,8], a parallel circuit model best describes the two RC circuits. The experimental resistive and capacitive values listed in Tables 6.2 and 6.3, respectively, were obtained from the Nyquist plots shown in Figures 6.5 and 6.6.

Summary

A means of assessing the electrochemical properties of the nanoarray was identified through the use of voltammetric, amperometric, and impedance measurements. Measurement of single electron transfer processes occurring at the nanoarray/solution interface elucidated how electrochemical behavior changed with electrode size when a comparison to conventional electrode diffusion properties was made. Evaluation of the nanoarray limiting current enabled calculation of the active nanoelectrode area. It was determined that the

number of Pt nanoparticles/cm² functioning as an electrode was four orders of magnitude less than that deposited on the substrate and seven orders of magnitude less than what was available in the ablated flux. The distance between electrodes was slightly greater than four times the average nanoelectrode size.

References

- [1] L. Petry, D. C. Hansen, "Final Report of the Evaluation of Chemical and Biological Warfare Agent Simulants," Technical Report Number UDR-TR-2007-00072, University of Dayton Research Institute, Dayton, OH (Jun 28, 2006).
- [2] J. E. B. Randles, "A Cathode Ray Polarograph. Part II.-The Current-Voltage Curves," *Trans. Faraday. Soc.*, **44** (1948) 327.
- [3] A. Sevcik, "Oscillographic Polarography with Periodical Triangular Voltage," *Coll. Czech. Chem. Commun.*, **13** (1948) 349.
- [4] R. S. Nicholson, I. Shain, "Theory of Stationary Electrode Polarography: Single Scan and Cyclic Methods Applied to Reversible, Irreversible, and Kinetic Systems," *Anal. Chem.*, **36** (1964) 706.
- [5] R. J. White, H. S. White, "Electrochemistry in Nanometer-Wide Electrochemical Cells," *Langmuir*, **24** (2008) 2850.
- [6] Y. Zhang, J. Zhou, L. Lin, Z. Lin, "Determination of Electrochemical Electron-Transfer Reaction Standard Rate Constants at Nanoelectrodes: Standard Rate Constants for Ferrocenylmethyltrimethylammonium (III)/(II) and Hexacyanoferrate (III)/(II)," *Electroanalysis*, **20** (2008) 1490.
- [7] W. B. Johnson, W. L. Worrell, Solid State Devices, in: E. Barsoukov, J. R. Macdonald (Eds.), *Impedance Spectroscopy - Theory, Experiment, and Applications*, 2nd ed., John Wiley & Sons, New Jersey, 2005, p. 294.

- [8] S. Oh, J. S. Lee, K. H. Jeong, L. P. Lee, "Minimization of Electrode Polarization Effect by Nanogap Electrodes for Biosensor Applications, in Micro Electro Mechanical Systems," The Sixteenth Annual International Conference, IEEE, MEMS-03 Kyoto, 52, Jan 19-23, 2003, IEEE, (2003).

Tables

Table 6.1

Measured limiting current and calculated A_A values for the nanoarrays

Condition	Limiting Current (i_d)	Active Area (A_A)
Vacuum growth nanoarray	350 μA	$1.51 \times 10^{-4} \text{ cm}^2$
Argon growth nanoarray	165 nA	$7.13 \times 10^{-8} \text{ cm}^2$
Conventional electrode	3 μA	$3.52 \times 10^{-2} \text{ cm}^2$
Silicon Substrate	8 nA	$3.45 \times 10^{-9} \text{ cm}^2$

Table 6.2

Resistive components of electrochemical impedance data for TTFA nanoelectrodes in solutions of ferricyanide, sodium chloride, or propylene carbonate

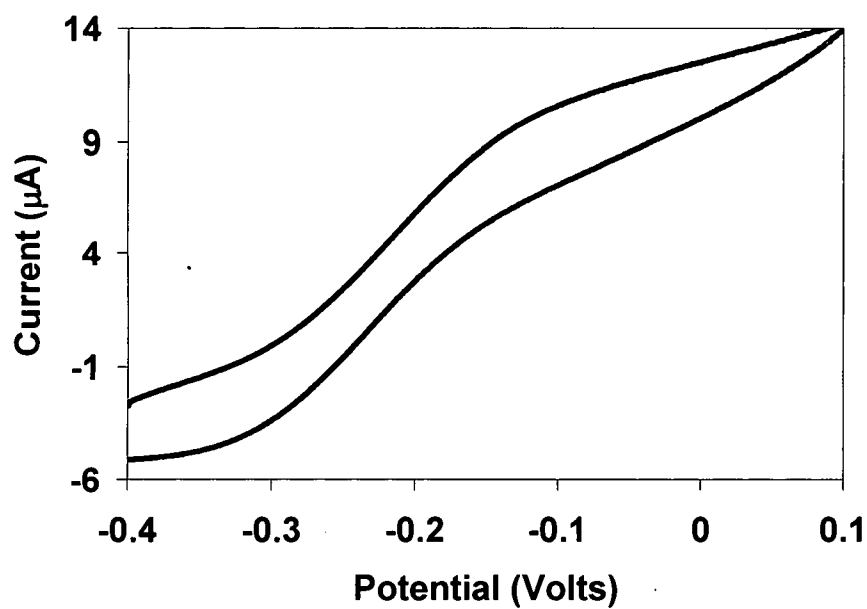
Solution	R1 (ohms)	R2 (ohms)	R3 (ohms)
Ferricyanide	1.325×10^3	9.201×10^4	9.201×10^4
Sodium Chloride	9.304×10^3	4.485×10^4	2.590×10^5
Propylene Carbonate	2.052×10^4	2.022×10^5	3.716×10^4

Table 6.3

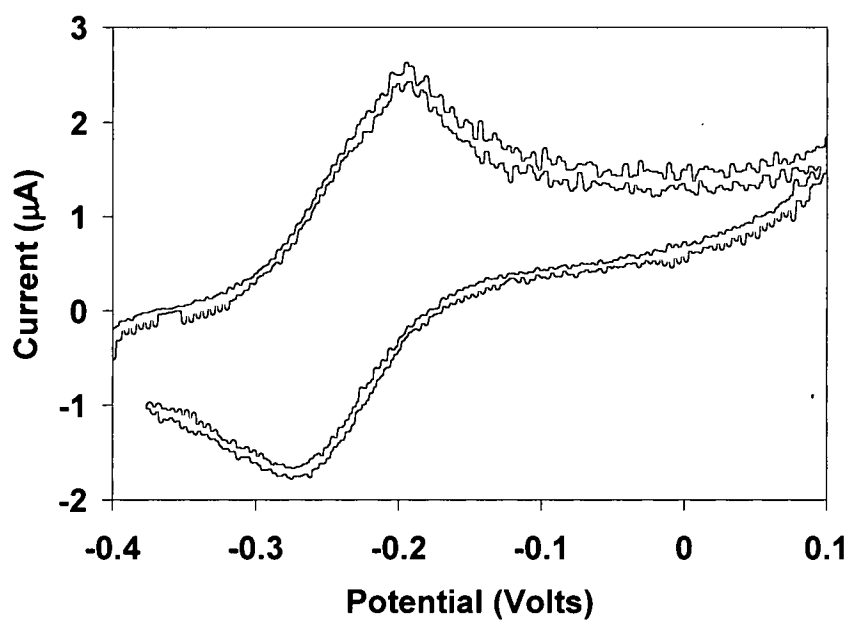
Capacitive components of electrochemical impedance data for TTFA nanoelectrodes in solutions of ferricyanide, sodium chloride, or propylene carbonate

Solution	C1	C2
Ferricyanide	162.9 nF	20.27 μ F
Sodium Chloride	2.570 nF	4.920 μ F
Propylene Carbonate	115.1 pF	136.9 nF

Figures



(a)



(b)

Figure 6.1. (a) Cyclic voltammogram from an array of Pt nanoelectrodes as-deposited in vacuum by TTFA. (b) Cyclic voltammogram exhibited by the conventional Pt electrode.

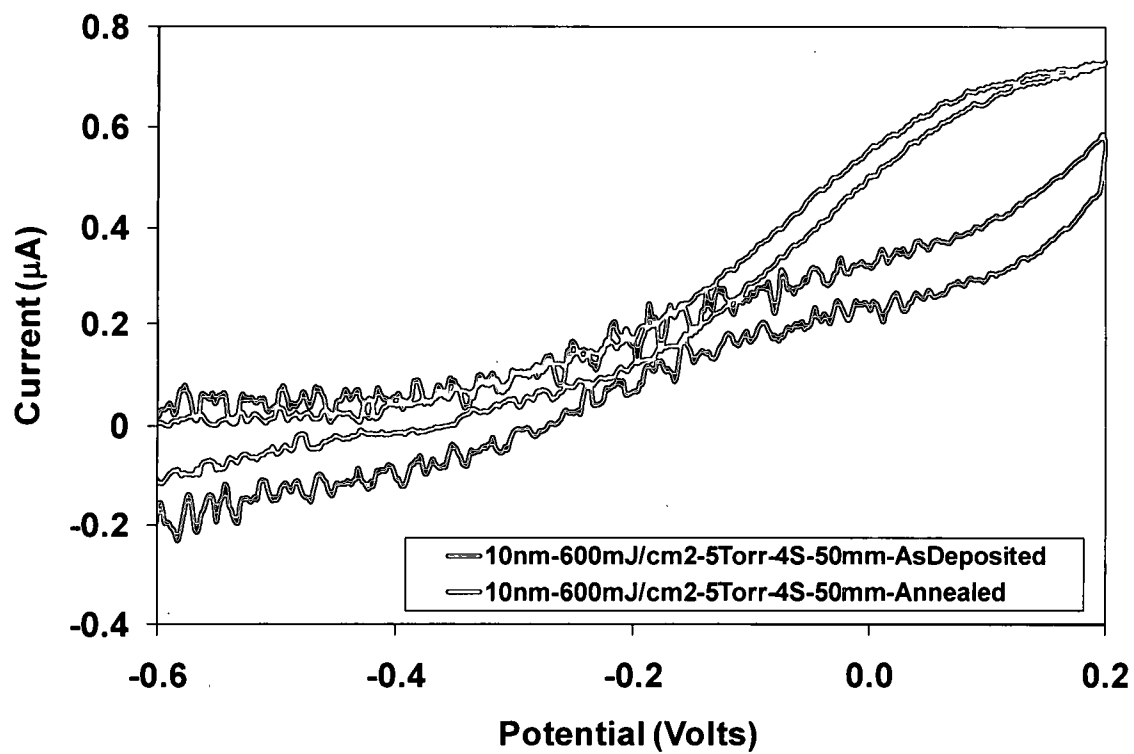


Figure 6.2. Comparison of cyclic voltammograms from an as-deposited vs. annealed array of Pt nanoelectrodes.

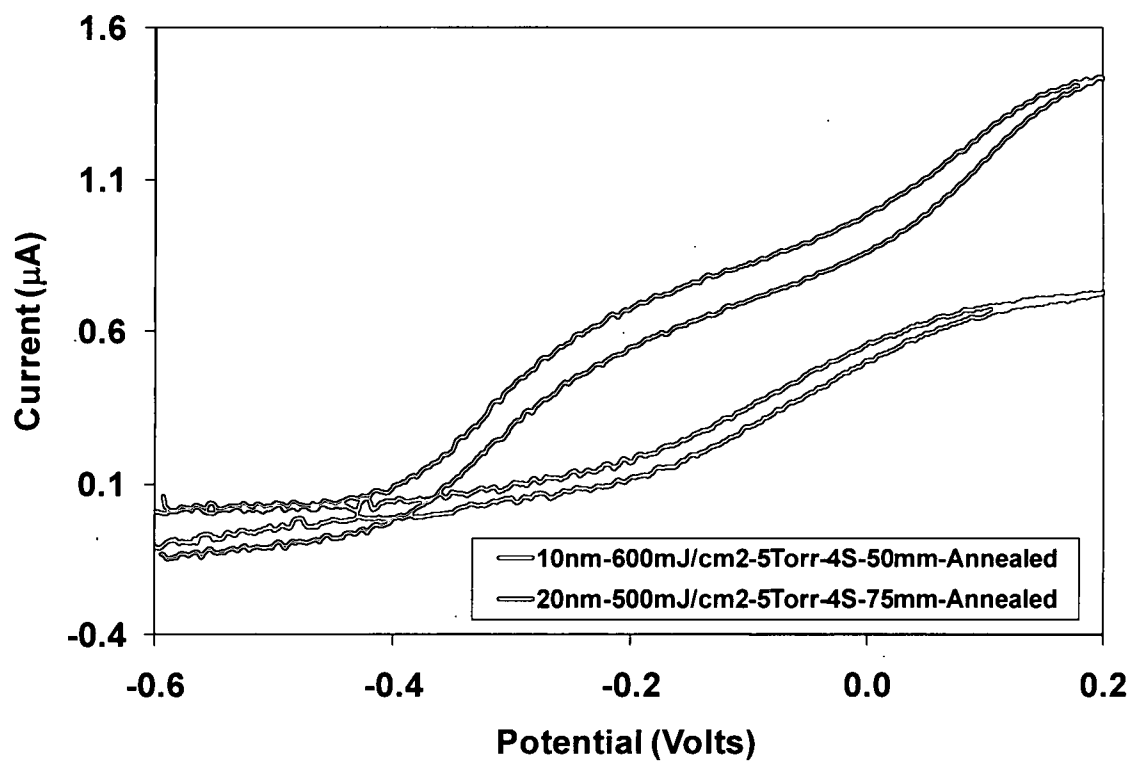


Figure 6.3. Comparison of cyclic voltammograms from an array of Pt nanoelectrodes synthesized via different ablation parameters and annealed.

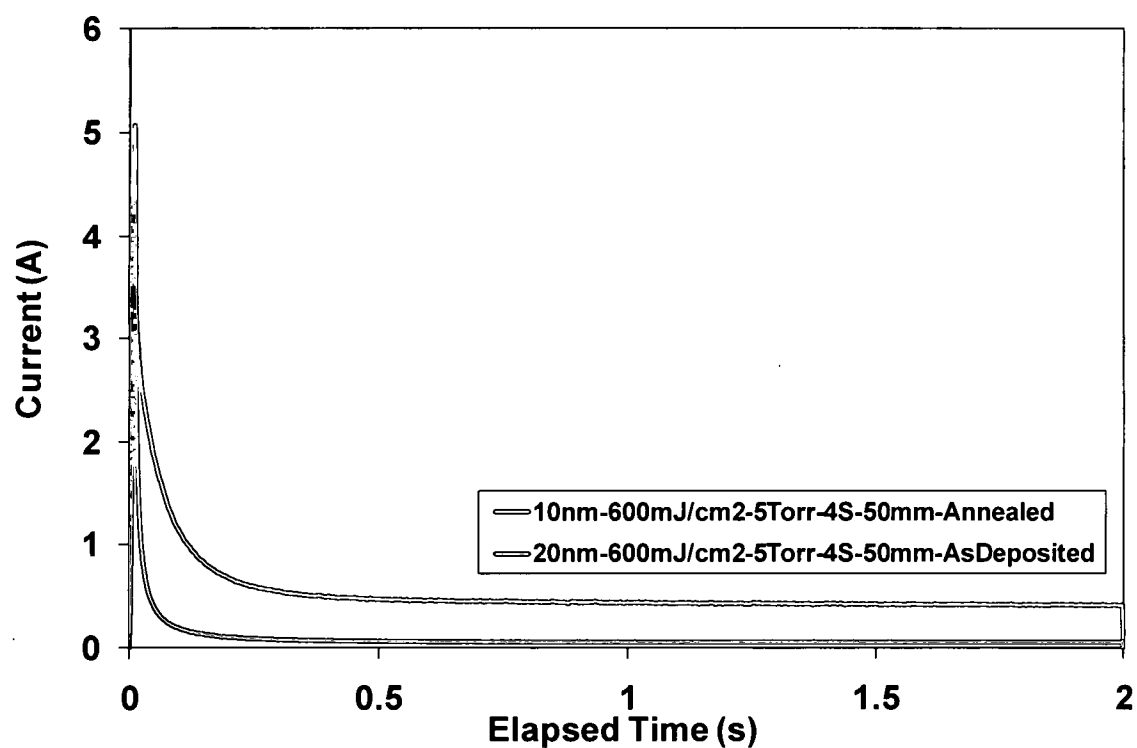


Figure 6.4. Chronoamperometric data for Pt nanoarrays grown in argon at the optimum ablation parameters using targets of different thicknesses.

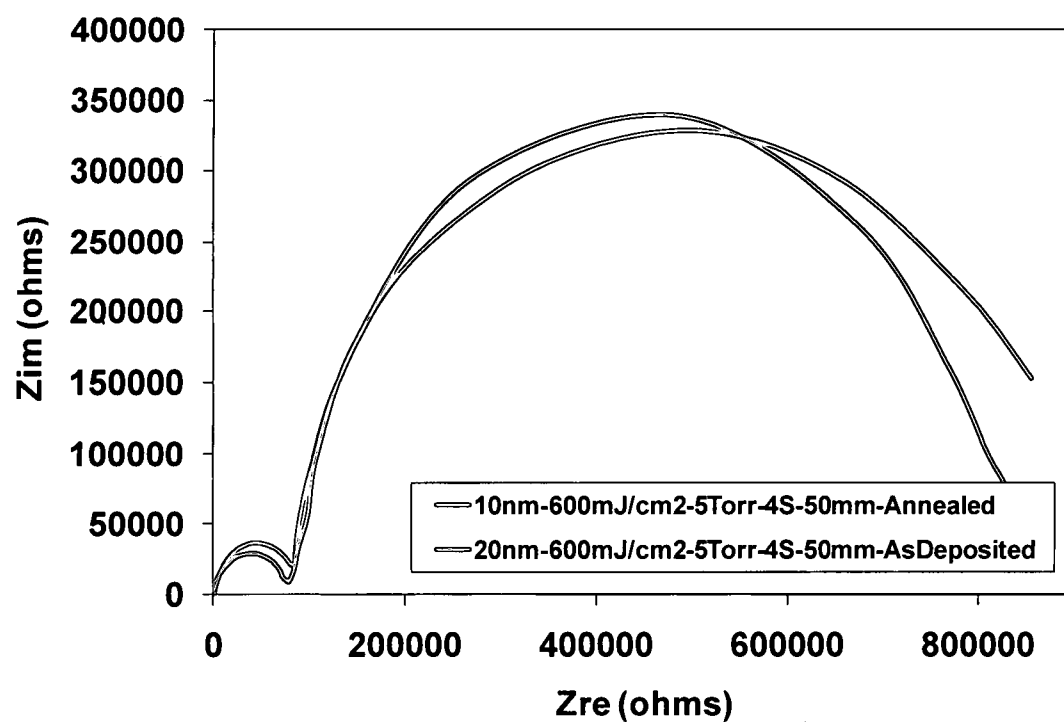


Figure 6.5. Nyquist plots for Pt nanoarrays grown in argon at the optimum ablation parameters using targets of different thicknesses. The absence of Warburg impedance indicates the transport effects due to diffusion are small.

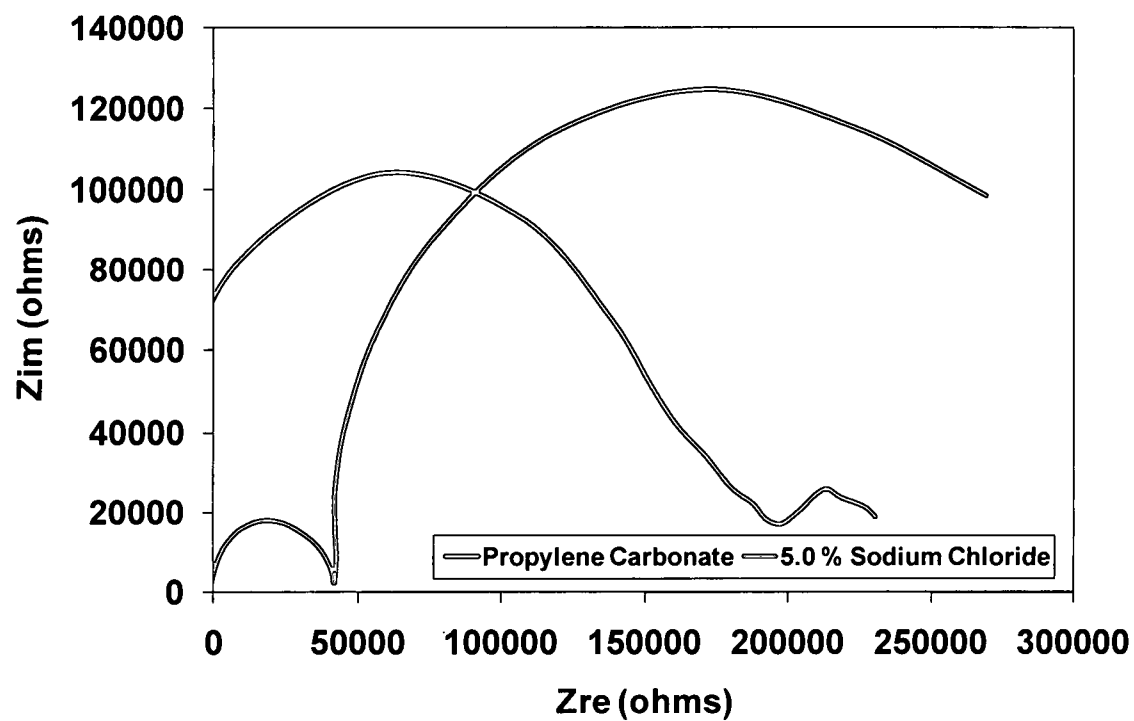
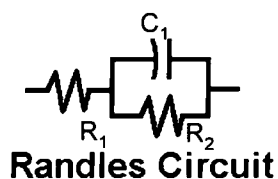
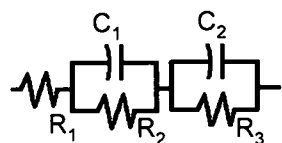


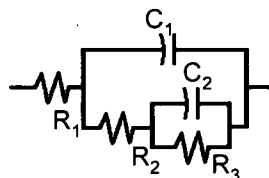
Figure 6.6. Nyquists plots of impedance measurements for TTFA Pt nanoarrays in the presence of propylene carbonate (chemical warfare simulant) or 5.0 % sodium chloride (highly conductive and corrosive electrolyte).



(a)



(b)



(c)

Figure 6.7. Possible equivalent circuit models. (a) Conventional Randles Circuit where the impedance is best described by the double-layer capacitance in parallel with the charge transfer resistance, both of which are in series with the electrolyte resistance. (b and c) Models in varying configurations distinguishing two time constants (two RC circuits) in series with the electrolyte resistance. In both cases, the capacitor can be replaced by a constant phase element.

CHAPTER VII

CONCLUSIONS AND RECOMMENDATIONS

There are nine requisites for contented living: health enough to make work a pleasure; wealth enough to support your needs; strength to battle with difficulties and overcome them; grace enough to confess your sins and forsake them; patience enough to toil until some good is accomplished; charity enough to see some good in your neighbor; love enough to move you to be useful and helpful to others; faith enough to make real the things of God; hope enough to remove all anxious fears concerning the future.

-Johann Wolfgang von Goethe

The preparation of nonagglomerated nanoelectrode arrays using TTFA is presented. This method of nanofabrication enables platinum metal nanoparticles of desired size (several nanometers in diameter) and requisite uniformity to be deposited easily and reproducibly onto silicon substrates. Increasing the target-substrate distance results in an increase in the mean nanoparticle separation. Conversely, the mean nanoparticle separation is reduced by decreasing the target-substrate distance or by increasing the number of laser pulses. The nanoparticle density distribution is also adjustable by varying the laser energy density at the target as well as by the addition of background gas. The TTFA process results are not strongly dependent upon starting target film thickness. Platinum diffusion into the silicon substrate creates a conductive platinum silicide interface that becomes more catalytic with annealing. Implementation of area 4 will require the assistance of skilled electrical engineers.

A means of assessing the electrochemical properties of the nanoarray has been identified through the use of voltammetric, amperometric, and impedance measurements. Measurement of single electron transfer processes occurring at the nanoarray/solution interface elucidates how electrochemical behavior changes with electrode size when a comparison to conventional electrode diffusion properties is made. Evaluation of the nanoarray limiting current enables calculation of the active nanoelectrode area. Thus, it is anticipated that the use of nanostructured electrodes will improve sensor sensitivity, selectivity, response time, and efficiency.

Future work with platinum nanoelectrode arrays should incorporate some lessons learned (i.e. CE placement position for resistive solutions and cell geometry to minimize solution volume and aid in concentrating analyte of interest) during the pursuit of this work and focus on the following four areas: (1) Evaluating nanosensor electrochemical detection limits with different analytes (Figure 7.1) [1,2] and resistive solutions (Figure 7.2). using a different cell geometry with a smaller solution volume (Figure 7.3). (2) Utilizing the nanoelectrode arrays as catalysts to be functionalized and characterizing resulting structure (Figure 7.4). (3) Alloying nanoelectrode arrays using a dual layer target and characterizing the resulting structure (Figures 7.5 through 7.8) [3,4]. (4) Prototyping a scaled up model of the original nanosensor as well as any functionalized or alloyed nanostructure.

Presented in Figure 7.1 is preliminary data for the electrochemical reduction of cadmium using a TTFA Pt nanoelectrode array prepared using optimum ablation parameters. The blue curve of Figure 7.1a demonstrates the reduction of cadmium for a conventional Pt electrode, whereas the feasibility of Pt nanoelectrode arrays to reduce metals (10ppm cadmium, maroon curve and 20 ppm cadmium, black curve) in a solution of ferricyanide is indicated in Figure 7.1b. The green curve of Figure 7.1b is for the reduction of ferricyanide, only, at the surface of a conventional electrode. Chronoamperometric data showing increasing current with increasing concentration of cadmium being reduced is presented in Figure 7.1c. This data supports a potential application for the nanoelectrodes developed using TTFA which is in the determination of water quality.

Impedance analyses using the Pt nanoelectrode arrays in propylene carbonate (PC) were repeated to investigate the feasibility of making a three electrode measurement in the flat cell configuration using highly resistive solutions. The aqua (CE near) and purple (CE far) curves shown in Figure 7.2 were acquired with the CE in different positions relative to WE (Pt array) in PC. In this experiment, the polarization values (R_p) were within an order of magnitude of each other and therefore did not represent a significant difference between the two measurements using the flat cell configuration. Thus, the solution resistance was sufficiently high to prevent polarization of the sample; otherwise, a larger

difference between the curves would have been observed. This result is a lesson learned for future experiments using resistive solutions.

An impedance spectrum from a Pt TF on Si in a different cell geometry using a smaller electrolyte volume is presented in Figure 7.3. In this example, the Pt TF is used because, with the change in cell geometry, it demonstrates the Warburg impedance characteristic of a macroelectrode and represented the utility of not only an alternative design configuration but also a smaller solution volume (i.e. a few mL instead of approximately 300 mL). The smaller solution volume is necessary to assist with metal [2] or even protein [1] concentration in ferricyanide solution prior to future electrochemical analysis.

Using the Pt nanoelectrode arrays as catalysts to be functionalized and characterizing the resulting structure is shown in Figure 7.4. The micrograph image of carbon nanotube (CNT) growth at 900°C on TTFA deposited Pt nanoparticles on Si substrates was acquired with the HRSEM. Spiraling tubes on the order of 20 nm are observed enveloping the Pt catalysts in the image of Figure 7.4a. High resolution XPS analyses of this sample indicate the presence of Pt catalysts (Figure 7.4b) and the formation of oxide on Si (Figure 7.4c and Figure 7.4d for the Si 2p and 2s signals, respectively). These results support the use of the deposited Pt NP for use in fuel cells or for carbon based sensors [3].

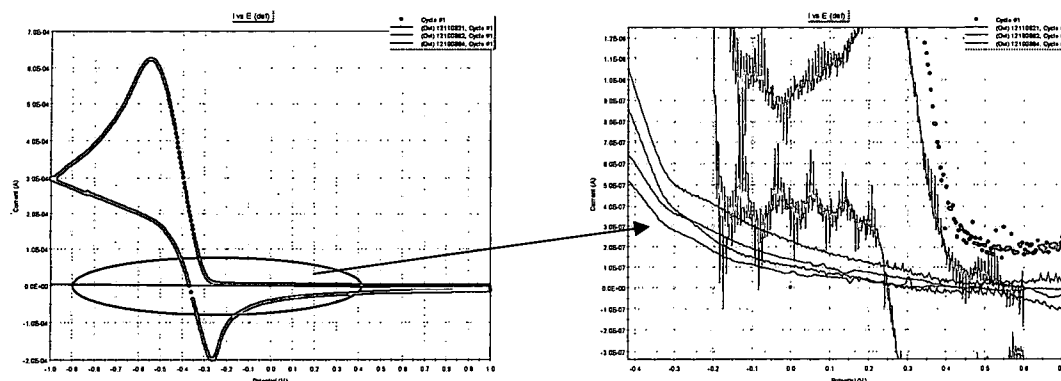
The micrograph images of FePt nanoparticles ablated via TTFA at 5 Torr Ar and 10 Torr Ar are presented in Figure 7.5a and Figure 7.5b, respectively, using a dual layer target consisting of a 10 nm Fe TF layer sandwiched between

the transparent support and a 10nm Pt TF layer (Figure 7.5c). Chemical composition information for TTFA synthesized FePt nanoparticles determined using backscattered electrons (BSE) at 10000x and 20000x is shown in Figure 7.6a and Figure 7.6b, respectively. For the BSE images, the higher atomic number Pt NPs appear brighter relative to the regions of lower atomic number, or Fe NPs. This data coupled with the inset photo of Figure 7.5a indicates that it is possible to fabricate alloyed NPs or multicompositional NPs. Further investigation into the chemical composition of FePt nanoparticles deposited via TTFA on Si substrates surveyed using XRD and XPS (Figure 7.7a and Figure 7.7b, respectively) as well as the high resolution XPS analyses presented in Figure 7.8 confirms this is the case. Multicompositional NPs are useful for fuel cell and magnetic recording media applications [3,4].

References

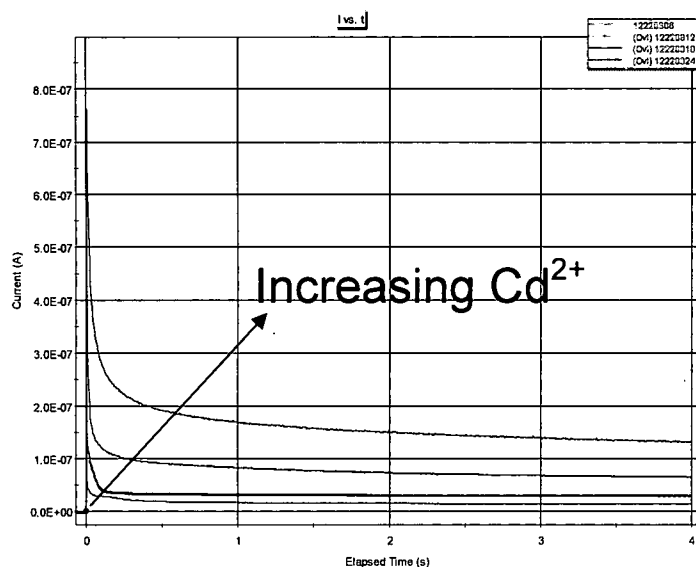
- [1] A. Bogomolova, E. Komarova, K. Reber, T. Gerasimov, O. Yavuz, S. Bhatt, M. Aldissi, "Challenges of Electrochemical Impedance Spectroscopy in Protein Biosensing," *Anal. Chem.*, 81 (2009) 3944.
- [2] G. H. Hwang, W.K. Han, J. S. Park, S. G. Kang, "An Electrochemical Sensor Based on the Reduction of Screen-Printed Bismuth Oxide for the Determination of Trace Lead and Cadmium," *Sens. Actuators B*, 135 (2008) 309.
- [3] H. Yano, M. Kataoka, H. Yamashita, H. Uchida, M. Watanabe, "Oxygen Reduction Activity of Carbon-Supported Pt-M (M = V, Ni, Cr, Co, and Fe) Alloys Prepared by Nanocapsule Method," *Langmuir*, 23 (2007) 6438.
- [4] K. Yano, V. Nandwana, N. Poudyal, C. B. Rong, J. P. Liu, "Rapid Thermal Annealing of FePt Nanoparticles," *J. Appl. Phys.*, 104 (2008) 013918.

Figures



(a)

(b)



(c)

Figure 7.1. (a) The blue curve demonstrates the reduction of cadmium for a conventional Pt electrode. (b) Investigation into feasibility of Pt nanoelectrode array to reduce metals (10ppm cadmium, maroon curve and 20 ppm cadmium, black curve) in a solution of ferricyanide. The green curve is for the reduction of ferricyanide solution, only, at the surface of a conventional electrode. (c) Chronoamperometric data showing increasing current with increasing concentration of cadmium being reduced.

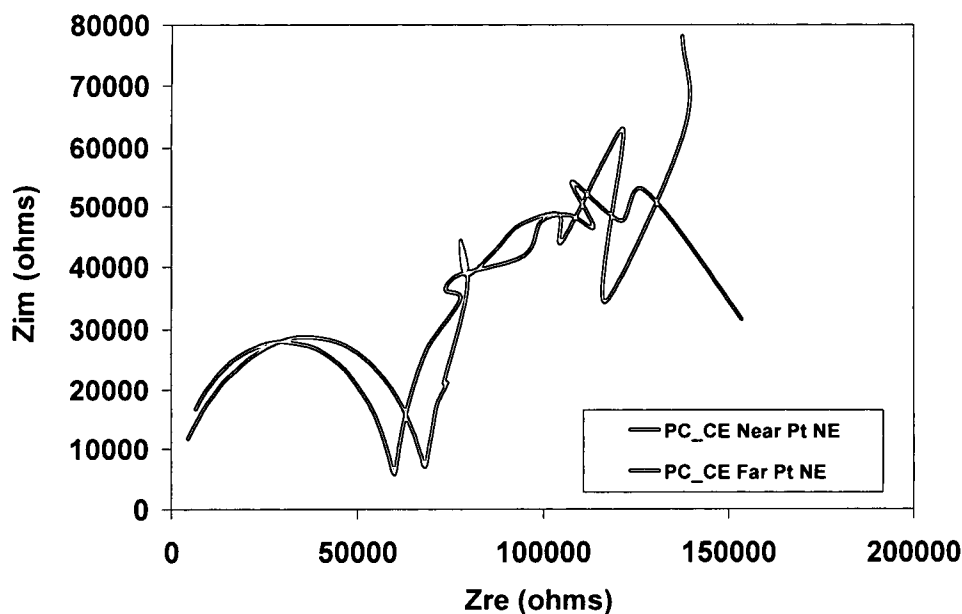


Figure 7.2. Impedance spectra from Pt nanoelectrode array in propylene carbonate (PC). The aqua (CE near) and purple (CE far) curves were acquired with the CE in different positions relative to WE (Pt array).

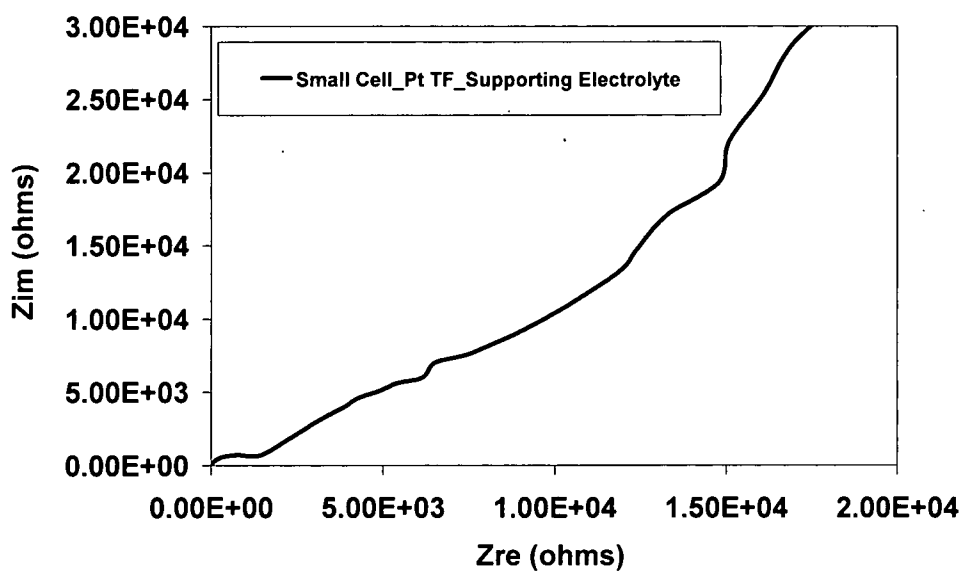
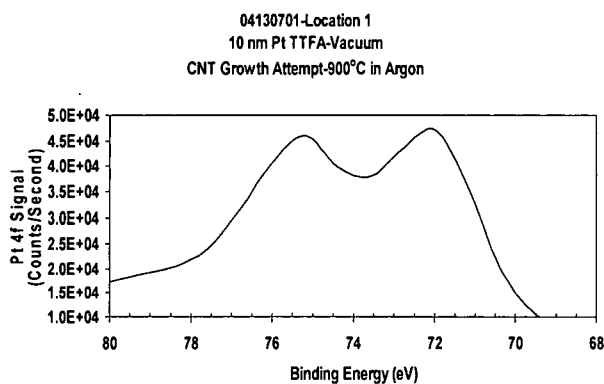


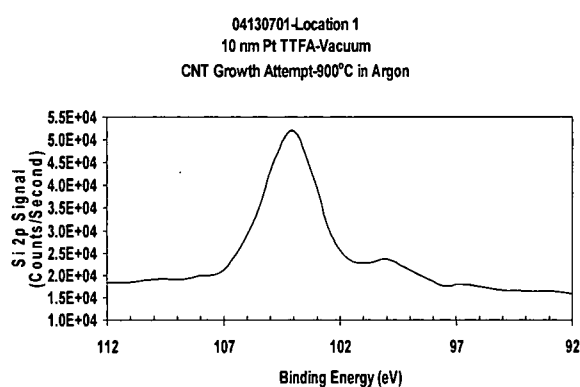
Figure 7.3. Impedance spectrum from Pt TF on Si in a different cell geometry using a smaller electrolyte volume.



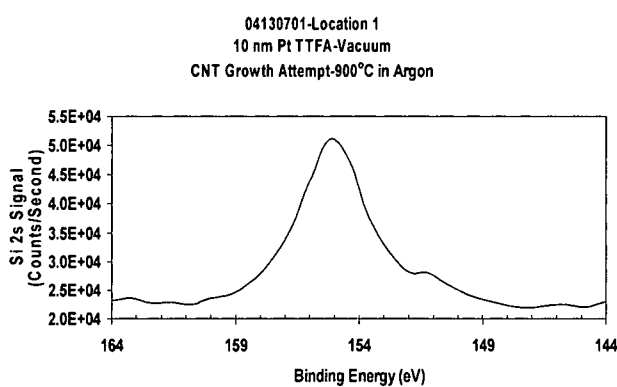
(a)



(b)

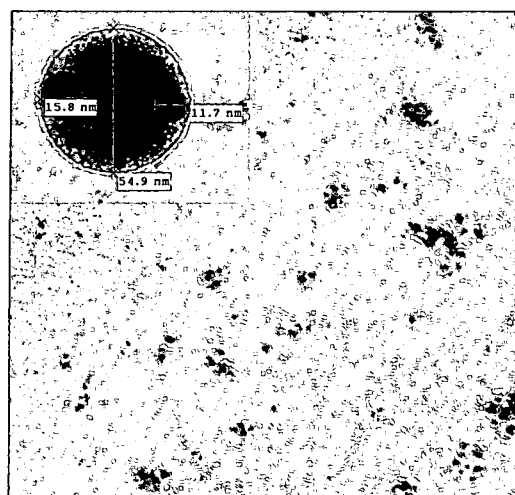


(c)



(d)

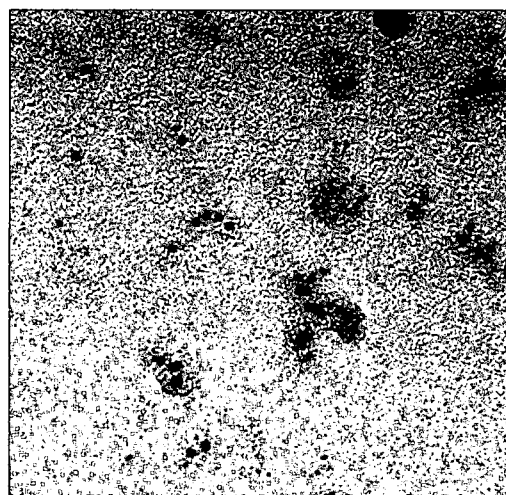
Figure 7.4. (a) Micrograph image of carbon nanotube (CNT) growth at 900°C on TTFA deposited Pt nanoparticles on Si substrates. High resolution XPS analyses of this sample indicate the presence of (b) Pt catalysts and formation of oxide on Si as shown in the (c) Si 2p and (d) Si 2s signals.



300000x

20 nm

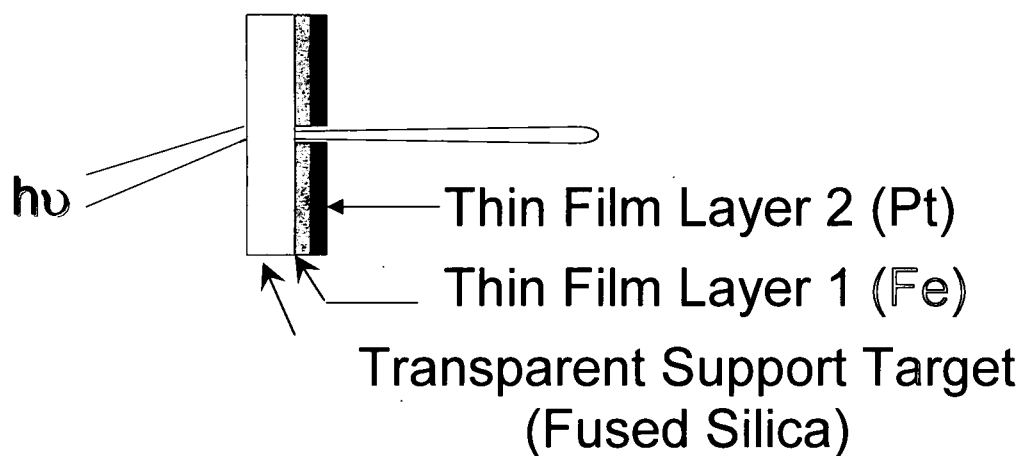
(a)



300000x

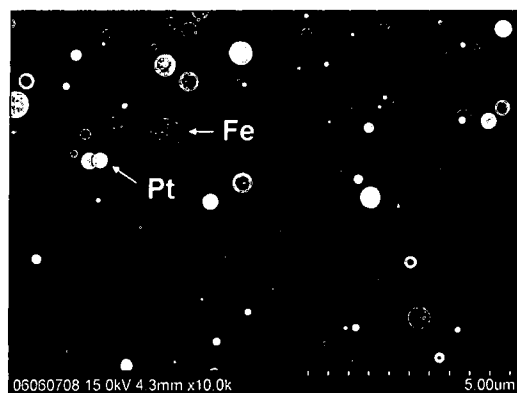
20 nm

(b)

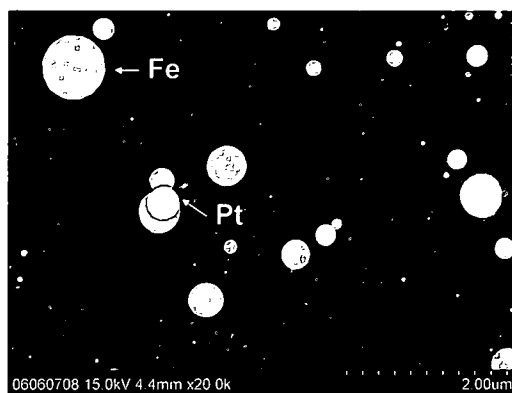


(c)

Figure 7.5. Micrograph images of FePt nanoparticles ablated via TTFA at (a) 5 Torr Ar and (b) 10 Torr Ar using (c) a dual layer target consisting of a 10 nm Fe TF layer sandwiched between the transparent support and a 10nm Pt TF layer.

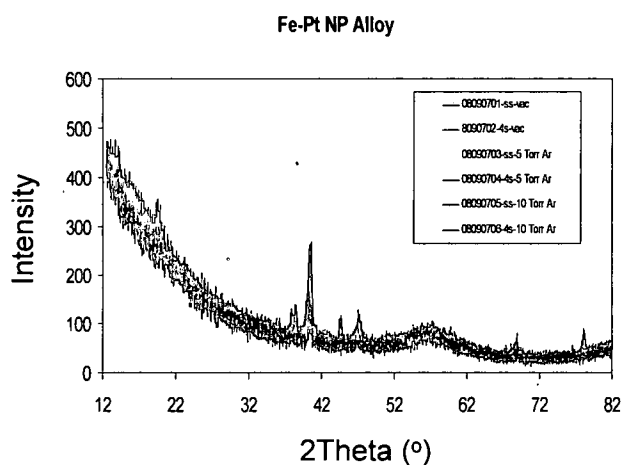


(a)

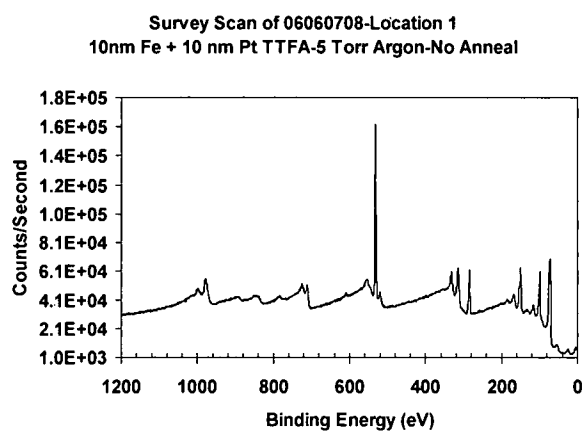


(b)

Figure 7.6. Chemical composition information for TTFA FePt nanoparticles determined using backscattered electrons (BSE) at (a) 10000x and (b) 20000x.



(a)



(b)

Figure 7.7. Chemical composition of FePt nanoparticles deposited via TTFA on Si substrates surveyed using (a) XRD and (b) XPS.

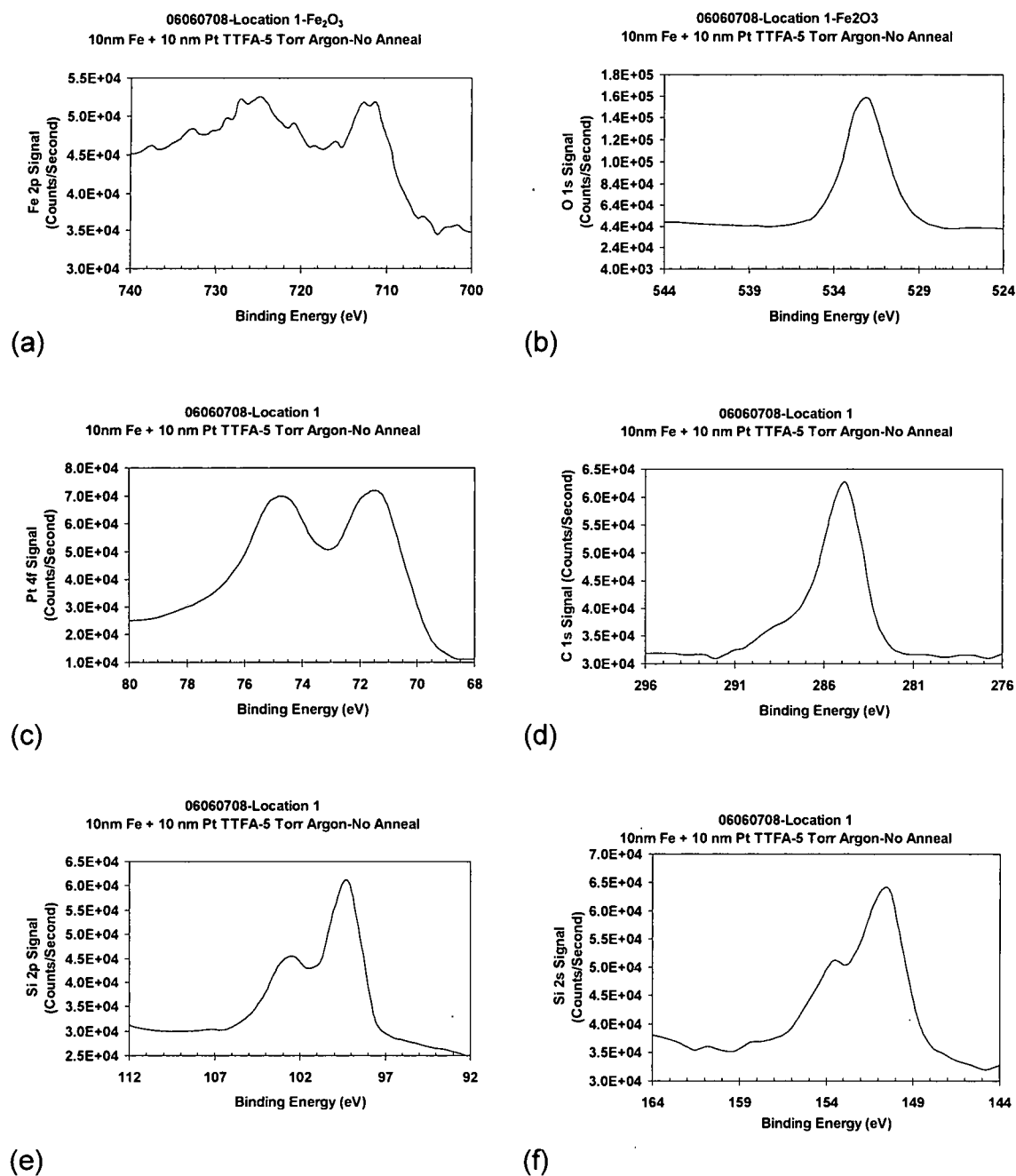


Figure 7.8. (a) Fe 2p, (b) O 1s, (c) Pt 4f, (d) C 1s, (e) Si 2p, and (f) Si 2s high resolution XPS analyses of FePt nanoparticles.

APPENDIX A

CALCULATION OF IONIZED PLATINUM PER ABLATED PLATINUM ATOM

In Figure 3.1 it was noted that the area of the laser footprint was 2.4 cm^2 . For the 20 nm TF from which the ion current data was shown, this corresponded to a volume of $4.8 \times 10^{-6} \text{ cm}^3$. The maximum ion current of $2.2 \times 10^{-4} \text{ A}$ was extrapolated from the voltage intensity of 11 mV from Figure 3.5 for a 50 ohm resistor equaling $9.2 \times 10^{-5} \text{ A/cm}^2$. For the negative peak at 54 μs having a current of $2.2 \times 10^{-4} \text{ A}$, a charge of $1.2 \times 10^{-8} \text{ coulombs (C)}$ was calculated indicating 7.4×10^{10} ions per laser pulse were produced.

Since Pt has a density of 21.41 g/cm^3 , the amount of Pt ablated per laser pulse for a volume of $4.8 \times 10^{-6} \text{ cm}^3$ equals $1.0 \times 10^{-4} \text{ g}$. Dividing the amount of Pt ablated by the atomic mass of Pt (195 g/mol) gives the number of moles of Pt ablated or $5.1 \times 10^{-7} \text{ moles Pt}$. Multiplying the number of moles of Pt ablated by Avogadro's number ($A_v = 6.0 \times 10^{23} \text{ atoms/mol}$) is $3.1 \times 10^{17} \text{ atoms ablated}$, and therefore, $2.0 \times 10^{-7} \text{ ions/atom}$. Thus, for a face centered cubic (FCC) Pt structure containing approximately 1300 atoms per 3 nm particle, there are 2.4×10^{14} nanoparticles per laser pulse.

APPENDIX B

ESTIMATED ENERGY OF PLATINUM DURING MELT TRANSITION

If this reaction was exothermic in nature, based on the following calculation for ΔH_1 ,

$$\Delta H_1 = (187 \text{ J kg}^{-1} \text{ K}^{-1}) (2939 \text{ K} - 2042 \text{ K}) \quad (\text{A.1})$$

$$\Delta H_1 = (187 \text{ J kg}^{-1} \text{ K}^{-1}) (897 \text{ K})$$

$$\Delta H_1 = 167.7 \text{ kJ/kg}$$

then a Pt nanoparticle having an average diameter of 3 nm or 1300 atoms during the melting transition would have an energy of 443.8 eV based on the following estimation:

$$\begin{aligned} (1300 \text{ atoms}) (195 \text{ g/mol}) (1 \text{ mol} / 6.0 \times 10^{23} \text{ atoms}) &= 4.2 \times 10^{-19} \text{ g} \\ &\text{or } 4.2 \times 10^{-22} \text{ kg.} \end{aligned} \quad (\text{A.2})$$

Since $\Delta H_1 = 167.7 \text{ kJ/kg}$, then

$$\begin{aligned} (167.7 \text{ kJ/kg}) (4.2 \times 10^{-22} \text{ kg}) &= 7.1 \times 10^{-20} \text{ kJ} \\ &\text{or } 7.1 \times 10^{-17} \text{ J} \\ &\text{or } 7.1 \times 10^{-14} \text{ mJ.} \end{aligned} \quad (\text{A.3})$$

Dividing this result by charge gives

$$(7.1 \times 10^{-17} \text{ J}) / (1.6 \times 10^{-19} \text{ C}) = 443.8 \text{ eV.} \quad (\text{A.4})$$

APPENDIX C

TABULAR AND GRAPHICAL REPRESENTATION OF TTFA EFFICIENCY AND PERCENT SUBSTRATE COVERAGE

By carefully selecting the ablation parameters, the ablation process can be manipulated in such a way as to nucleate, grow, and accelerate ablated species by the transfer of energy and momentum in the plasma toward a substrate. For example, laser energies on the order of tens of kilojoules (kJ) can sufficiently ionize approximately 10^{22} atoms (the number of atoms in a 0.3 cm cube at solid density) [1]. It can be calculated from a unit cell that a 3 nm FCC Pt nanoparticle with a surface area of 28 nm^2 will contain approximately 1300 atoms [2].

Additionally, high power (i.e. 10^9 W) at ultraviolet (UV) wavelengths (i.e. 248 nm for a KrF gas mixture) is typically generated for excimer lasers. When operated at a repetition rate of a few hertz (Hz), laser energies in the tens of millijoules (mJ) per pulse can be emitted. Thus, control of the laser power output (watts (W) or one joule per second (J/s)) is another way to control the transfer of energy and the ablation conditions necessary to synthesize nanoparticles, specifically the Pt nanoparticles synthesized in this study. The ablation energies used in this study were 600 mJ/pul and 500 mJ/pul. The higher ablation energy was found to be optimum for the TTFA synthesis process.

This Appendix C presents tabular and graphical representations of the TTFA efficiency and substrate percent coverage analyses. As shown in Table C.1 and Figure C.1, the TTFA method is an efficient means to generate small platinum nanoparticles, with an increase in the nanoelectrode radius implying a greater percentage of substrate is covered with platinum (Table C.2 and Figure C.2). These results indicate the 600 mJ/pul is more than sufficient to remove the Pt TF from the target and generate Pt species in the plume, which have enough energy to wet, adhere, and provide substrate coverage.

Table C.1

TTFA efficiency based on nanoparticle diameter size

Diameter (nm)	Approx. No. [2] (atoms)	Efficiency (NP/pul)	Energy (mJ)
1	433	7.2×10^{14}	2.4×10^{-14}
3	1300	2.4×10^{14}	7.1×10^{-14}
5	2167	1.4×10^{14}	1.2×10^{-13}
10	4333	7.2×10^{13}	2.4×10^{-13}
20	8667	3.8×10^{13}	4.7×10^{-13}
50	21667	1.4×10^{13}	1.2×10^{-12}
100	43333	7.2×10^{12}	2.4×10^{-12}
250	108333	2.9×10^{12}	5.9×10^{-12}

Table C.2

Substrate coverage as a function of nanoelectrode radius size

Radius (nm)	Area/Particle (cm ²)	Coverage (%)
0.5	7.9×10^{-15}	0.4
1.5	7.1×10^{-14}	3.5
2.5	2.0×10^{-13}	9.8
5	7.9×10^{-13}	39.3
10	3.1×10^{-12}	157.1
25	2.0×10^{-11}	981.7
50	7.9×10^{-11}	3927.0
125	4.9×10^{-10}	24543.7

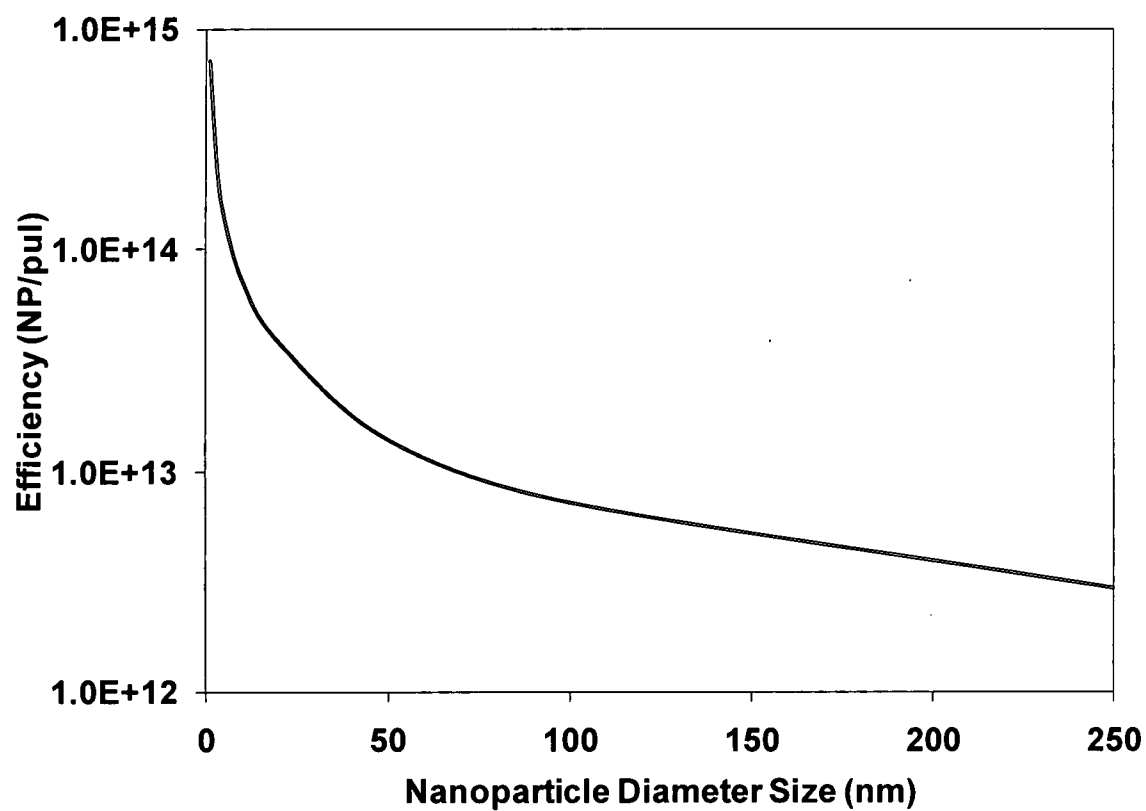


Figure C.1. The TTFA method is an efficient means to generate small platinum nanoparticles.

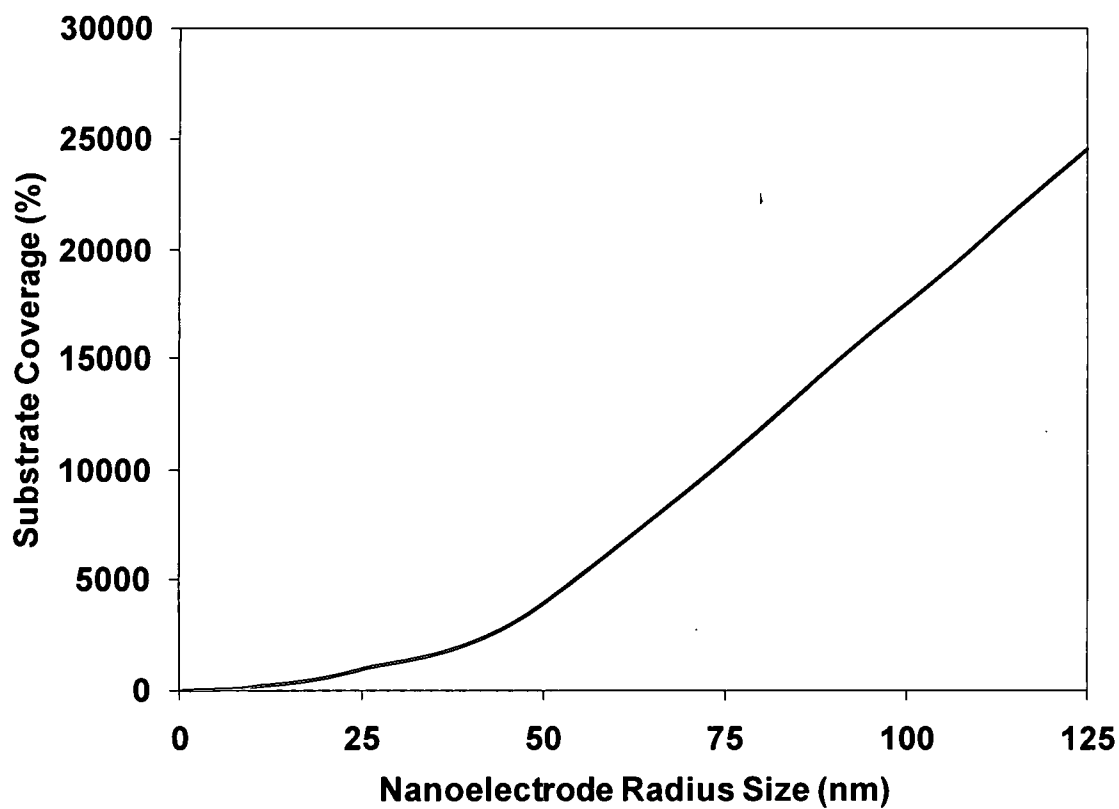


Figure C.2. An increase in the nanoelectrode radius indicates a greater percentage of substrate is covered with platinum.

R70203 SS93

References

- [1] A. R. Bell, Laser-Produced Plasmas, in: R. O. Dendy (Ed.), Plasma Physics - An Introductory Course, Cambridge University Press, Great Britain, 1993, p. 319.
- [2] H. Akbarzadeh, G. A. Parsafar, "A Molecular-Dynamics Study of Thermal and Physical Properties of Platinum Nanoclusters," Fluid Phase Equilibria, 280 (2009) 16.